

ACIX-III AQUA

EVALUATION OF ATMOSPHERIC CORRECTION PROCESSORS FOR HYPERSENSITIVE SATELLITE OVER INLAND AND COASTAL WATERS



**A comparative analysis of atmospheric
correction methods applied to PRISMA and
EnMAP using in situ reflectance data**



CNR-IREA, Milan, November 2025

ISBN 979-12-985355-2-7

Author list and affiliations

Claudia Giardino¹, Nima Pahlevan², Alice Fabbretto^{1,3}, Lodovica Panizza¹, Andrea Pellegrino^{1,4}, Ryan Vandermeulen⁵, Marco Gianinetto⁶, Stefan Adriaensen⁷, Joram Agten⁷, Hendrik Bernert⁸, Liesbeth De Keukelaere⁷, Tristan Harmel⁹, Thomas Heege⁸, Anders Knudby⁹, Karin Schenk⁸, François Steinmetz¹⁰, Sindy Sterckx⁷, Quinten Vanhellemont¹², Yulun Wu¹⁰, Federica Braga¹³, Vittorio E. Brando¹⁴, Mariano Bresciani¹, Ana Dogliotti¹⁵, Susanne Kratzer¹⁶, Salvatore Mangano¹, Daniel Odermatt¹⁷, Gian Marco Scarpa¹³, Thomas Schroeder¹⁸, Mortimer Werther¹⁷, Ettore Lopinto¹⁹, Kevin Alonso²⁰, Noelle Cremer²⁰, Georgia Doxani²⁰, Ferran Gascon²⁰

Astrid Bracher^{21,22}, Mariana A. Soppa²¹, Avotramalala Najoro Radrianalisoa²¹
and additionally all other coauthors from Soppa et al. (2024) who are not listed above:
Maximilian Brell²³, Sabine Chabrilat²⁴, Leonardo M. A. Alvarado²⁵, Peter Gege²⁶, Stefan Plattner²⁴, Ian Somlai-Schweiger²⁴, Nicole Pinnel²⁴, Simone Collela¹⁴, Dieter Vansteenwegen²⁵, Maximilian Langheinrich²⁶, Emiliano Carmona²⁶, Martin Bachmann²⁶, Miguel Pato²⁶, Sebastian Fischer²⁷

¹ Institute of Electromagnetic Sensing of the Environment (IREA), CNR, Milan, Italy.

² NASA Goddard Space Flight Center, Greenbelt, MD, USA.

³ Department of Remote Sensing, Tartu Observatory, University of Tartu, Tõravere, Estonia

⁴ Department of Engineering, University of Sapienza, Rome, Italy.

⁵ NOAA Fisheries, Silver Spring, MD, USA.

⁶ Politecnico di Milano, Milan, Italy.

⁷ Flemish Institute for Technological Research (VITO), Mol, Belgium.

⁸ EOMAP GmbH & Co. KG, Seefeld, Germany.

⁹ Earth Observation Unit, Magellium, Ramonville-Saint-Agne, France.

¹⁰ University of Ottawa, Ottawa, Canada.

¹¹ HYGEOS, Lille, France.

¹² Royal Belgian Institute of Natural Sciences (RBINS), Brussels, Belgium.

¹³ Institute of Marine Sciences (ISMAR), CNR, Venice, Italy.

¹⁴ Institute of Marine Sciences (ISMAR), CNR, Rome, Italy.

¹⁵ Instituto de Astronomía y Física del Espacio (IAFE), Buenos Aires, Argentina.

¹⁶ Department of Ecology, Environment and Plant Sciences (DEEP), Stockholm University, Stockholm, Sweden.

¹⁷ Swiss Federal Institute of Aquatic Science and Technology (EAWAG), Dübendorf, Switzerland.

¹⁸ Commonwealth Scientific and Industrial Research Organisation (CSIRO), Brisbane, Australia.

¹⁹ Italian Space Agency (ASI), Rome, Italy.

²⁰ European Space Research Institute, European Space Agency (ESA), Frascati, Italy.

²¹ Alfred Wegener Institute Helmholtz Centre for Polar and Marine Research, 27570 Bremerhaven, Germany

²² Institute of Environmental Physics, University of Bremen, Otto-Hahn-Allee 1, 28359 Bremen, Germany

²³ GFZ German Research Centre for Geosciences, Potsdam, Germany²¹ CSIRO, Brisbane, Australia

²⁴ German Aerospace Center (DLR), Remote Sensing Technology Institute, Weßling, Germany

²⁵ Flanders Marine Institute (VLIZ), Oostende, Belgium

²⁶ Earth Observation Center (EOC), German Aerospace Center (DLR), Weßling, Germany

²⁷ German Aerospace Center (DLR), Bonn, Germany

TABLE OF CONTENTS

1	ABSTRACT	10
2	KEY POINTS	11
3	INTRODUCTION.....	12
3.1	REPORT AIMS	15
4	MATERIALS AND METHODS.....	17
4.1	IN SITU DATA.....	17
4.1.1	AERONET-OC NETWORK	17
4.1.2	COMMUNITY VALIDATION DATABASE	18
4.2	ATMOSPHERIC CORRECTION MODELS.....	18
4.2.1	ACOLITE.....	19
4.2.2	hGRS.....	20
4.2.3	POLYMER	21
4.2.4	iCOR	21
4.2.5	MIP	22
4.2.6	PACO-WASI.....	22
4.2.7	ACOLITE-T-Mart.....	23
5	PRISMA DATA ANALYSIS	25
5.1	FEATURES OF THE PRISMA DATASET USED IN THE EXERCISE	25
5.2	MATCH-UPS ANALYSIS	26
5.2.1	DATASET	27
5.2.2	PERFORMANCE ASSESSMENT	27
5.2.3	STATISTICS.....	28
5.2.4	QUALITY WATER INDEX POLYNOMIAL	29
5.3	RESULTS	31
5.3.1	OVER THE SITES	31
5.3.2	OVER THE SPECTRAL BANDS	37
5.3.3	OPTICAL WATER TYPES.....	50
5.4	INTERPRETING THE QWIP OUTPUT	55
6	EnMAP DATA ANALYSES.....	61
6.1	DATASET AND MATCH-UP ANALYSIS.....	61
6.2	IN SITU DATA.....	61
6.3	EnMAP DATA	63
6.4	MATCH-UP ANALYSIS	63

6.5	PERFORMANCE ASSESSMENT	65
6.5.1	MULTISPECTRAL PERFORMANCE	65
6.5.2	HYPERSPETRAL PERFORMANCE	72
7	CONCLUSIONS	79
8	ACKNOWLEDGMENTS	81
9	REFERENCES	82
10	PRISMA DATA REPOSITORY	90
11	PRISMA GALLERY	91

LIST OF FIGURES

Figure 1 Dataset of the globally distributed sites and number of available match-ups between PRISMA and field data. The colour of the dots indicates the number of available match-ups ranging from a minimum of 1 to a maximum of 17 for every study area. The Location of AERONET-OC are indicated with circles only, the black dots indicate CVD sites; Rio de la Plata and AAOT (Venice) are both AERONET-OC and CVD. The bottom-right bar plot shows the frequency distribution of Rrs on the y-axis, with the values in sr^{-1} reported on the x-axis. This is shown for both multispectral (AERONET-OC, light blue) and hyperspectral (CVD, green) in situ data collection. The darker blue area shows the overlap between the two distributions.....	27
Figure 2 Reference OWTs for the different AC models performance assessment [79].	28
Figure 3 Spectral comparisons between PRISMA L2C and in situ data in the 21 globally distributed AERONET-OC sites. The variability across the dataset in the mean spectra of PRISMA L2C is displayed as blue curves, with the shaded blue area representing the standard deviation. The mean and standard deviation of the in situ data are equivalently shown in orange. SA represents the Spectral Angle and N represents the number of the images.	32
Figure 4 Spectral comparisons between ACOLITE and in situ data in the 21 globally distributed AERONET-OC sites. The variability across the dataset in the mean spectra of ACOLITE is displayed as blue curves, with the shaded blue area representing the standard deviation. The mean and standard deviation of the in situ data are equivalently shown in orange. SA represents the Spectral Angle and N represents the number of the images.	33
Figure 5 Spectral comparisons between hGRS and in situ data in the 21 globally distributed AERONET-OC sites. The variability across the dataset in the mean spectra of hGRS is displayed as blue curves, with the shaded blue area representing the standard deviation. The mean and standard deviation of the in situ data are equivalently shown in orange. SA represents the Spectral Angle and N represents the number of the images.	34
Figure 6 Spectral comparisons between POLYMER and in situ data in the 21 globally distributed AERONET-OC sites. The variability across the dataset in the mean spectra of POLYMER is displayed as blue curves, with the shaded blue area representing the standard deviation. The mean and standard deviation of the in situ data are equivalently shown in orange. SA represents the Spectral Angle and N represents the number of the images.	34
Figure 7 Spectral comparisons between iCOR and in situ data in the 21 globally distributed AERONET-OC sites. The variability across the dataset in the mean spectra of PRISMA iCOR is displayed as blue curves, with the shaded blue area representing the standard deviation. The mean and standard deviation of the in situ data are equivalently shown in orange. SA represents the Spectral Angle and N represents the number of the images.	35
Figure 8 Spectral comparisons between MIP and in situ data in the 21 globally distributed AERONET-OC sites. The variability across the dataset in the mean spectra of MIP is displayed as blue curves, with the shaded blue area representing the standard deviation. The mean and standard deviation of the in situ data are equivalently shown in orange. SA represents the Spectral Angle and N represents the number of the images.	36
Figure 9 Spectral comparisons between ACOLITE-T-Mart and in situ data in the 21 globally distributed AERONET-OC sites. The variability across the dataset in the mean spectra of ACOLITE-T-Mart is displayed as blue curves, with the shaded blue area representing the standard deviation. The mean and standard deviation of the in situ data are equivalently shown in orange. SA represents the Spectral Angle and N represents the number of the images.	36
Figure 10 Overall performance of AC processors using the AERONET-OC match-ups with all the satellite data combined. The number of matchups per processor and per band is reported in the scatterplots (N) along with the statistics. The black lines refer to the 1:1 line.	38
Figure 11 Performance assessments as determined by the Median Symmetric Accuracy (ϵ) and Bias (β ;) for all the match-ups combined. The dashed line corresponds to a 30% threshold [18].	39
Figure 12 Overall performance of AC processors using the AERONET-OC match-ups with all the satellite data combined (equal size samples). The number of matchups per processor and per band is reported in the scatterplots (N) along with the statistics. The black lines refer to the 1:1 line.	40
Figure 13 Performance assessments as determined by the Median Symmetric Accuracy (ϵ) and Bias (β ;) for all the match-ups combined (equal size samples). The dashed line corresponds to a 30% threshold [18].	41

Figure 14 Spectral comparisons between PRISMA L2C and hyperspectral in situ data in the 8 sites of the CVD. The variability across the dataset in the mean spectra of PRISMA L2C is displayed as blue curves, with the shaded blue area representing the standard deviation. The mean and standard deviation of the in situ data are equivalently shown in orange. SA represents the Spectral Angle and N represents the number of the images.	42
Figure 15 Spectral comparisons between ACOLITE and hyperspectral in situ data in the 8 sites of the CVD. The variability across the dataset in the mean spectra of ACOLITE is displayed as blue curves, with the shaded blue area representing the standard deviation. The mean and standard deviation of the in situ data are equivalently shown in orange. SA represents the Spectral Angle and N represents the number of the images.	43
Figure 16 Spectral comparisons between hGRS and hyperspectral in situ data in the 8 sites of the CVD. The variability across the dataset in the mean spectra of hGRS is displayed as blue curves, with the shaded blue area representing the standard deviation. The mean and standard deviation of the in situ data are equivalently shown in orange. SA represents the Spectral Angle and N represents the number of the images.	44
Figure 17 Spectral comparisons between POLYMER and hyperspectral in situ data in the 8 sites of the CVD. The variability across the dataset in the mean spectra of POLYMER is displayed as blue curves, with the shaded blue area representing the standard deviation. The mean and standard deviation of the in situ data are equivalently shown in orange. SA represents the Spectral Angle and N represents the number of the images.	44
Figure 18 Spectral comparisons between iCOR and hyperspectral in situ data in the 8 sites of the CVD. The variability across the dataset in the mean spectra of iCOR is displayed as blue curves, with the shaded blue area representing the standard deviation. The mean and standard deviation of the in situ data are equivalently shown in orange. SA represents the Spectral Angle and N represents the number of the images.	45
Figure 19 Spectral comparisons between MIP and hyperspectral in situ data in the 8 sites of the CVD. The variability across the dataset in the mean spectra of MIP is displayed as blue curves, with the shaded blue area representing the standard deviation. The mean and standard deviation of the in situ data are equivalently shown in orange. SA represents the Spectral Angle and N represents the number of the images.	46
Figure 20 Spectral comparisons between ACOLITE-T-Mart and hyperspectral in situ data in the 8 sites of the CVD. The variability across the dataset in the mean spectra of ACOLITE-T-Mart is displayed as blue curves, with the shaded blue area representing the standard deviation. The mean and standard deviation of the in situ data are equivalently shown in orange. SA represents the Spectral Angle and N represents the number of the images.	46
Figure 21 Overall performance of AC processors using the CVD match-ups with all the satellite data combined. The number of matchups per processor and per band is reported in the scatterplots (N) along with the statistics. The black lines refer to the 1:1 line.	48
Figure 22 Performance assessments as determined by the Median Symmetric Accuracy (ϵ) and Bias (β) for all the match-ups combined. The dashed line corresponds to a 30% threshold.	48
Figure 23 Overall performance of AC processors using the CVD match-ups with all the satellite data combined (equal size samples). The number of matchups per processor and per band is reported in the scatterplots (N) along with the statistics. The black lines refer to the 1:1 line.	49
Figure 24 Performance assessments as determined by the Median Symmetric Accuracy (ϵ) and Bias (β) for all the match-ups combined (equal size samples). The dashed line corresponds to a 30% threshold [18].	50
Figure 25 Performance assessments as determined by the spectral Median Symmetric Accuracy (ϵ) and Bias (β) for the AC methods. The dashed-dotted line corresponds to the 30% accuracy threshold suggested by GCOS and adopted also by ACIX-Aqua [18].	50
Figure 26 Mean values of PRISMA-derived Rrs spectra for each AC method, by OWT. For in situ data, AERONET-OC and CVD have been aggregated and plotted as mean values with standard deviations, from 443 to 667 nm. N provides the number of averaged in situ spectra per OWT.	52
Figure 27 Aggregation of pairwise inter-comparisons (heatmaps) obtained from the MdSA (%) reported in each cell. Processors with lighter colours (white/yellow) are likely to generate high quality for a given OWT and band.	54

Figure 28 An example of QWIP analysis output for a scene at Ariake Tower AERONET-OC site on May 11, 2020, processed using the hGRS AC approach. (A) Map of AVW, (B) Map of the QWIP score, (C) scatter plot of QWIP analysis, and (D) frequency distribution of incremental QWIP scores.	57
Figure 29 An example of QWIP analysis output for a scene at Ariake Tower AERONET-OC site on May 11, 2020, processed using the hGRS AC approach. These plots display the mean normalised spectral shapes meeting various criteria (A) $ QWIP < 0.2$, (B) $0.2 > QWIP > 0.4$, (C) $QWIP > 0.4$, (D) $QWIP < -0.4$, and (E) out of range water type.	58
Figure 30 Results obtained for a Lake Trasimeno scene considering all five AC models (A: ACOLITE, B: hGRS, C: POLYMER, D: iCOR, E: MIP) and T-Mart product (F). On the left it is shown the QWIP score map and on the right the scatterplots of the QWIP analysis.	60
Figure 31 Dataset of the globally distributed sites and number of available match-ups between EnMAP and field data. The colour of the dots indicates the number of available match-ups ranging from a minimum of 1 to a maximum of 13 for every study area. The Location of AERONET-OC are indicated with circles only, the black dots indicate CVD sites. AAOT (Venice) is both Hyperspectral (CVD sites) and AERONET-OC.	62
Figure 32 Frequency distribution of reflectance levels the hyperspectral (CVD) and multispectral in situ measurements (all wavelengths).	65
Figure 33 Spectral comparisons between EnMAP L2A water products (MIP) and in situ data in the 11 globally distributed AERONET-OC sites. The variability across the dataset in the mean spectra of MIP is displayed as blue curves, with the shaded blue area representing the standard deviation. The mean and standard deviation of the in situ data are equivalently shown in red. SA represents the Spectral Angle and N represents the number of the images.	66
Figure 34 Spectral comparisons between ACOLITE and in situ data in the 9 globally distributed AERONET-OC sites. The variability across the dataset in the mean spectra of ACOLITE is displayed as blue curves, with the shaded blue area representing the standard deviation. The mean and standard deviation of the in situ data are equivalently shown in red. SA represents the Spectral Angle and N represents the number of the images.	67
Figure 35 Spectral comparisons between POLYMER and in situ data in the 10 globally distributed AERONET-OC sites. The variability across the dataset in the mean spectra of POLYMER is displayed as blue curves, with the shaded blue area representing the standard deviation. The mean and standard deviation of the in situ data are equivalently shown in red. SA represents the Spectral Angle and N represents the number of the images.	68
Figure 36 Spectral comparisons between PACO-WASI and in situ data in the 12 globally distributed AERONET-OC sites. The variability across the dataset in the mean spectra of PACO-WASI is displayed as blue curves, with the shaded blue area representing the standard deviation. The mean and standard deviation of the in situ data are equivalently shown in red. SA represents the Spectral Angle and N represents the number of the images.	69
Figure 37 Overall performance of AC processors using the AERONET-OC match-ups with all the satellite data combined. The number of matchups per processor and per band is reported in Table 11 along with the statistics. The black lines refer to the 1:1 line.	70
Figure 38 Performance assessments as determined by the Median Symmetric Accuracy (ϵ) and median symmetric Bias (β) for all the match-ups combined. The dashed line corresponds to a 30% threshold [18].	72
Figure 39 Spectral comparisons between EnMAP L2A standard products (MIP) and hyperspectral in situ data in the 6 sites of the CVD. The variability across the dataset in the mean spectra of MIP is displayed as blue curves, with the shaded blue area representing the standard deviation. The mean and standard deviation of the in situ data are equivalently shown in red. SA represents the Spectral Angle and N represents the number of the images.	74
Figure 40 Spectral comparisons between ACOLITE and hyperspectral in situ data in the 5 sites of the CVD. The variability across the dataset in the mean spectra of ACOLITE is displayed as blue curves, with the shaded blue area representing the standard deviation. The mean and standard deviation of the in situ data are equivalently shown in red. SA represents the Spectral Angle and N represents the number of the images.	75
Figure 41 Spectral comparisons between POLYMER and hyperspectral in situ data in the 5 sites of the CVD. The variability across the dataset in the mean spectra of POLYMER is displayed as blue curves, with the shaded blue	

area representing the standard deviation. The mean and standard deviation of the in situ data are equivalently shown in red. SA represents the Spectral Angle and N represents the number of the images.76

Figure 42 Spectral comparisons between PACO-WASI and hyperspectral in situ data in the 6 sites of the CVD. The variability across the dataset in the mean spectra of PACO-WASI is displayed as blue curves, with the shaded blue area representing the standard deviation. The mean and standard deviation of the in situ data are equivalently shown in red. SA represents the Spectral Angle and N represents the number of the images.77

Figure 43 Spectra of ϵ , β , RMSE and MdAPE for MIP, Polymer, ACOLITE and PACO-WASI for coincident hyperspectral match-ups during the operational mission phase (N=7). The grey shaded area represents the required uncertainty (RMSE) outside of strong atmospheric absorption regions as defined by the EnMAP Ground Segment and for AOT at 550 nm lower than 0.4 [22].78

LIST OF TABLES

Table 1 A section of traceability matrix in the ‘Inland and Coastal’ water market area as defined by the CHIME MRD (cf. Table 4-1) showing link between user needs and requirements, defined on the basis of high-level EU policies and the CHIME mission requirements.....	13
Table 2 In situ data used in the study, percentage of location in inland and coastal waters (the % are computed with respect to the number of sites for each of the instruments). * highlights in situ data only used for matchups in the EnMAP data evaluation.	17
Table 3 Table 3 Main characteristics of the AC models and T-Mart model. Notably ACOLITE, POLYMER and MIP are applied to both PRISMA and EnMAP; hGRS, iCOR and T-Mart only to PRISMA; PACO-WASI only to EnMAP...	18
Table 4 Band settings in the different datasets: the nominal band used in the match-up analysis and the corresponding band settings of AERONET-OC and PRISMA.	26
Table 5 Conceptual description of OWTs [79].	28
Table 6 Band names.....	37
Table 7 AC models performance by wavelength and OWT (including also the T-Mart model).....	54
Table 8 Average SA results for each OWT class. N indicates the size of each class.	55
Table 9 List of study sites, location, type of in situ measurements and number of images (C: Commissioning, O: Operational mission phase, LQ: Low Quality).	61
Table 10 Band settings in the different datasets: the nominal band used in the match-up analysis and the corresponding band settings of AERONET-OC and EnMAP. The first part of the table refers to the band setting used for the entire dataset, while the second part refers to the additional bands considered for the CVD dataset only.....	64
Table 11 Summary of the five statistical metrics for the EnMAP matchup data shown in Figure 37. N represents the total number of samples for each band.	71
Table 12 Statistics of MIP, Polymer, ACOLITE and PACO-WASI for two wavelength ranges using the common hyperspectral dataset (both mission phases).	78

1 ABSTRACT

This report shows the main outcomes of the Atmospheric Correction Intercomparison Exercise (ACIX-III Aqua), aiming to test atmospheric correction (AC) processors on spaceborne imaging spectroscopy. Developed under the same concepts of ACIX-Aqua that enabled an evaluation of eight state-of-the-art AC processors available for multi-spectral satellite data, ACIX-III Aqua focuses on hyperspectral data, particularly as those acquired by the Italian Space Agency (ASI) satellite hyperspectral mission PRecursoRe IperSpettrale della Missione Operativa (PRISMA). Launched in March 2019, the PRISMA mission has acquired thousands of images over various marine and freshwaters, where *in situ* measurements were collected to enable match-up generation with satellite products. The *in situ* dataset originates from two sources: hyperspectral data contributed by the international community (called Community Validation Database, CVD) and multispectral measurements provided by the AERONET-OC network. This extensive data set allows the performance of each AC processor to be evaluated in different spectral regions and on eight different Optical Water Types (OWTs). Five AC models are participating in ACIX-III Aqua: ACOLITE, hGRS, POLYMER, iCOR, and MIP. Additionally, the standard AC product of PRISMA L2C was included in the comparison. Moreover, T-Mart, which focuses solely on adjacency effect correction, was also evaluated in combination with the ACOLITE model. PRISMA data were selected based on the synchronicity with the *in situ* measurements and the percentage of cloud cover, which was required to be less than 2%. The dataset finally consists of 174 images with *in situ* data derived from the AERONET-OC network and 65 images with *in situ* data obtained from the CVD network, for a total of 239 images. The match-up analysis is provided both per site and across the OWTs; the Quality Water Index Polynomial (QWIP) is also included in the analysis to identify Rrs spectra that fall outside the general trends observed in aquatic optics for optically deep inland and coastal waters. So far ACIX-III Aqua results seem consistent with previous findings of ACIX-Aqua for Landsat-8 and Sentinel-2. In particular, we observe largest differences between satellite and *in situ* measurements associated with the blue bands and NIR bands, and that each AC model has different degrees of accuracy depending on OWTs. Further results will be presented based on the latest progress in data analysis to understand how the variations in AC performance are related to the increased hyperspectral information content of PRISMA and how the results of this exercise compare to those obtained with other satellites to support the generation of improved products for aquatic applications from hyperspectral data collected by other current and future missions (e.g., CHIME). To the aim, the last section shows the first results obtained with EnMAP for 2022 to 2023 by applying three of the AC processors used with PRISMA (i.e. ACOLITE, MIP and POLYMER), and also including the PACO land AC processor in combination with WASI (PACO-WASI). In this case, the dataset consists of 25 images with *in situ* data derived from the AERONET-OC network and 21 images with *in situ* data obtained from the CVD network, for a total of 46 images.

2 KEY POINTS

- ACIX-III Aqua evaluated the performance of atmospheric correction (AC) processors on hyperspectral satellite data, following the methodology of ACIX-Aqua, which focused on multispectral data.
- Seven AC teams participated to the exercise by applying AC processors to PRISMA and EnMAP. For PRISMA we tested ACOLITE, hGRS, iCOR, MIP, POLYMER, ACOLITE-T-Mart (L2 PRISMA data were also included in the comparison); for EnMAP we analysed three ACOLITE, MIP, POLYMER and PACO+WASI.
- *In situ* reference data played a key role in assessing the performance of AC methods: a total of 285 water reflectance (Rrs) spectra, collected in coincidence with the satellite overpasses, supplied by both AERONET-OC and a community validation effort.
- The results were consistent with previous ACIX-Aqua findings, with no single AC method demonstrating superior performance across all conditions; accuracy varied by spectral band, but all showed largest and lowest discrepancies with *in situ* at 443 nm and 560 nm, respectively. All AC methods performed best in greenish waters while highest uncertainties were observed in dark, humic-rich waters.
- The two non-operational PRISMA and EnMAP national missions have been supporting the development of future operational spaceborne hyperspectral missions, such as PRISMA Second Generation (PRISMA SG), CHIME and SBG.
- Further efforts should be devoted to:
 - Fully exploiting the spatial assessment based on Quality Water Index Polynomial (QWIP) results provided per image and per AC processor.
 - Assess the sensitivity of water quality and biophysical parameters retrieval based on RRS results derived in the exercise to support applications and downstream services for aquatic ecosystems based on spaceborne imaging spectroscopy.
 - Continue the ACIX-III Aqua due to the growing number of match-ups that PRISMA/EnMAP are collecting over the sites; to the aim we suggest to support the deployment of autonomous fixed-position radiometers and field campaigns to both improve the global distribution of sites (e.g. Asia is much less represented than Europe) and the diversity of aquatic ecosystems (e.g. rivers were not included).

3 INTRODUCTION

Why are inland and coastal waters important?

Inland and coastal waters are complex ecosystems that provide habitats for aquatic species and are critical for global biodiversity. They play a key role in biogeochemical cycles, storing, transforming and transporting compounds and toxic substances. Aquatic environments are economically and recreationally valuable. Waters are used for multiple purposes, often in conflict with each other. The quality of inland and coastal waters is a key global issue due to human impact and environmental changes. These areas are among the most densely populated in the world, and the increasing number of users and uses is putting pressure on the ecosystem services. The degradation of these services is exacerbated by climate change and natural variability. Changes in the hydrological cycle and global temperature, leading to new mixing regimes and habitat shifts, are leading to profound societal impacts. In this context, there is an increasing need for regular monitoring of inland and coastal waters to support national and international directives and conventions such as the US Clean Water Act & Safe Drinking Water Act and the Australian Reef Water Quality Protection Plan, which require regular monitoring of biological, hydro-morphological and physical-chemical parameters of water bodies. Several European directives aim to achieve sustainable management of inland and coastal waters, maintaining or restoring high ecological status and safeguarding ecosystem services. Since 2000, the Water Framework Directive (WFD, 2000/60/CE) has been the legal framework for water management in the EU Member States, with the objective of achieving "good surface water status" for all European waters by 2015, both in terms of ecological status (i.e. healthy ecosystems) and chemical status (i.e. low pollution). In Italy, the determination of the trophic status of inland, coastal and transitional ecosystems, as required by the WFD, is carried out by the Regional Agencies for Environmental Protection (ARPA), which have activated multi-annual monitoring programmes. The Marine Strategy Framework Directive (MSFD, 2008/56/CE) and the Maritime Spatial Planning Directive (MSPD, 2014/89/EU) aim to support the sustainable development of the seas and oceans and to develop coordinated, coherent and transparent decision-making with regard to the Union's sectoral policies affecting the oceans, seas, islands, coastal and maritime sectors. Integrated Coastal Management (ICM) is introduced to ensure sustainable management of coastal resources. Environmental regulations for activities like dredging and aquaculture are becoming more stringent, requiring detailed assessments and monitoring. The EU Habitats Directive, the Drinking Water Directive, the Bathing Water Directive and Natura 2000 have been established to protect particularly unique and valuable habitats, drinking water resources and to ensure healthy bathing waters. These directives ensure that activities are compatible with good environmental status and do not compromise aquatic ecosystems, while allowing sustainable use of water by present and future generations.

How remote sensing, particularly the hyperspectral missions, can contribute?

Remote sensing techniques may be used for acquiring timely, frequent synoptic information, from local to global scales, of inland and coastal waters. Satellite based measurements of physical and biochemical parameters in these aquatic ecosystems mainly rely on the interpretation of the spectral reflectance. Multispectral and ocean colour sensors have been successfully applied for mapping inland and coastal waters for about 50 years [1–11]. Over the same period, when in the late 1980s the first airborne hyperspectral sensors were deployed over lakes, imaging spectrometry of aquatic ecosystems has followed similar progresses although much limited in time and geographic scale due to the lack in spaceborne imaging spectroscopy. After the launch of Hyperion in 2001, this situation has been rapidly changed thanks to recent imaging spectrometers deployments, from both the International Space Station (e.g., HICO, DESIS and EMIT) and the sun-synchronous polar-orbiting satellites, as PRISMA and EnMAP and more recently OCI on PACE. Particularly, the field of aquatic hyperspectral remote sensing is nowadays advancing rapidly for supporting potential new applications that are not limited by gaps in the spectrum. In inland and coastal waters, where the optically complexity of water is high hyperspectral data in fact provides a spectral setting and information redundancy needed for accurate retrievals of optical parameters [12–14]. Consequently, current spaceborne hyperspectral asset is supporting a variety of novel applications [15], covering for instance water quality monitoring and the assessment of aquatic biodiversity in pelagic and benthic habitats. Hyperspectral data provides potential new applications that are not limited by gaps in the spectrum based; the full-spectrum estimates of the diffuse attenuation coefficient (K_d) may lead to new insights about aquatic ecosystems and biodiversity processes like spectral niche partitioning and complementarity [16]. The potential contribution of a hyperspectral mission to the Copernicus Programme has been demonstrated in the Copernicus Hyperspectral Imaging Mission for the Environment (CHIME) - Mission Requirements Document (MRD)¹, highlighting how the identified data products, and more generally the applications addressing user needs can respond to specific EU policies and directives issued to regulate at European level several thematic areas. Table 1 shows these from high-level EU policies and key observational requirements.

Table 1 A section of traceability matrix in the ‘Inland and Coastal’ water market area as defined by the CHIME MRD (cf. Table 4-1) showing link between user needs and requirements, defined on the basis of high-level EU policies and the CHIME mission requirements.

1. Policy/Directives/Conventions/initiatives	2. Market Area	3. Stakeholders	4. User needs	5. EO Data products	6. Key observational Requirements
EU Water Framework Directive. EU Bathing Water Directive, EU Urban Waste Water Treatment Directive, EU Biodiversity Strategy, Natura 2000, United Nations Convention on Biological Diversity, United Nations	Inland- and coastal waters	Water Protection Agencies, Water authorities, Aquaculture, Dredging industry, Recreation and tourism sectors	Water quality assessment for e.g. inland and coastal water management, aquaculture practices, fishery; Water pollution management for e.g. harmful	Spectral water leaving radiance, inherent optical properties, light penetration depth, phytoplankton pigments (chl-a, PC, PE) and size class, suspended matters (with their inorganic/organic	Spatial resolution: HIGH/MODERATE Spectral resolution: HIGH Temporal resolution: HIGH/MODERATE Data latency: MEDIUM/LONG

¹ https://esamultimedia.esa.int/docs/EarthObservation/Copernicus_CHIME_MRD_v3.0_Issued_21_01_2021.pdf

Sustainable Development Goal No. 6 Ramsar Convention on Wetlands			algae blooms; Ecosystem assessment in terms of e.g. phytoplankton typing and phenology, underwater light field; Mass transport for e.g. coastal erosion; Coral reef assessment; Understanding roles of lakes in the global carbon cycle	fractions), colored dissolved organic matter, bottom properties (substrate types, status and depth), type and properties of aquatic vegetation (submerged, floating and emergent vegetation), type and properties of floating materials (e.g. oils, cyanobacterial scum)	High SNR in the VNIR (plus SWIR for extreme turbid waters, emerging vegetation and floating materials, improving atmospheric correction)
--	--	--	---	--	--

What are the challenges?

Most of the challenges in inland and coastal water observations are still due to the atmospheric correction (AC). This is due to numerous confounding factors such as the complexity of water optical properties including those related to the bottom, the surface glint, the heterogeneous nature of atmospheric aerosols (e.g., the proximity to terrestrial sources of atmospheric pollution which results in a heterogeneous atmosphere that is difficult to model), and the proximity of bright land surfaces. This combination of factors makes it difficult to retrieve accurate information about the observed system also due to the impossibility of applying the ocean colour approaches because of the non-negligible reflectance of water in the near-infrared region due to high sediment concentrations. Nonetheless, an accurate modelling of atmospheric absorption and scattering effects, in addition to the specular water surface reflection effects, is required to derive the typical water reflectance, the key variable for aquatic remote sensing applications. Remote Sensing Reflectance (R_{rs}), defined as the ratio of water-leaving radiance to the total downwelling irradiance just above water, is a spectral quantity, which depends on the content and concentration of optically reactive substances dissolved or suspended in the euphotic layer of water column, as well as on illumination conditions. R_{rs} spectrum is the result of the interaction of the electromagnetic signal with, in addition to the water itself, phytoplankton, detrital and organic matter substances, dissolved or suspended in the water column (e.g., Chlorophyll-a (Chl-a), Total Suspended Matter (TSM) and Colored Dissolved Organic Matter (CDOM)). It might also include the spectral properties of bottom types (e.g., coral, mud, seagrass) and of floating matter (e.g., aquatic vegetations, plastic, oil) which absorb and scatter light in a different way along the electromagnetic spectrum.

3.1 REPORT AIMS

Water reflectance can be inferred by Top-Of-Atmosphere signal measured from remote sensors through a processing chain, which primarily includes the removal of atmospheric effects. In fact, on the total amount of the signal recorded by remote sensing optical sensors, water and water components contribution is very small, while most of the signal is due to the interactions with the atmosphere (up to 90%). AC is hence a key step to obtain high quality Rrs and thus an accurate retrieval of bio-physical parameters, then supporting a variety of research and applications. A lot of efforts have been conducted to develop and improve methods for correcting satellite images such as the Atmospheric Correction Intercomparison eXercise (ACIX), jointly conducted in 2018 by NASA and the ESA in coordination with the Committee on Earth Observation Satellites (CEOS) validation group. The first exercise ACIX-I [17] focused on diverse land-cover types and continental/coastal atmospheric conditions and mostly evaluated Aerosol Optical Thickness (AOT) retrieval to gauge performances.

Then, as scope of the first exercise was not considering the assessments of water reflectance, a second ACIX (ACIX-II), hereafter referred to as ACIX-Aqua, started. The scope of the ACIX-Aqua was to provide an objective assessment of state-of-the-art of AC over inland and coastal waters for multispectral data gathered by Landsat-8 Operational Land Imager (OLI) and Sentinel-2A/B MultiSpectral Instrument (MSI). The exercise results were successfully published [18]. Shortly, through a considerable effort of *in situ* data collation, they were able to assess comprehensively the performance of eight different AC processors.

Based on the success of ACIX-Aqua, the same framework supported the starting of the third exercise, ACIX-III Aqua, now dedicated to satellite hyperspectral data. Started in 2020, ACIX-III Aqua was developed based on satellite data gathered from the PRISMA mission, placed in orbit in March 2019, hence allowing to collect a reasonable number of cloud-free images of inland and coastal waters. The PRISMA observations were targeted over inland and marine waters in which reference field Rrs measurements have been made available. As for ACIX-Aqua, *in situ* data were originated from two sources: hyperspectral data offered by the international community (henceforth called Community Validation Database, CVD) and by the Ocean Color component of AERONET multispectral measurements (AERONET-OC). Five AC methods participated in ACIX-III Aqua. Additionally, the standard AC product of PRISMA L2C was included in the comparison. Separately, a method focusing solely on adjacency effect correction, was also evaluated in combination with the other ACs. This volume of data permitted the evaluation of the AC models individually, per site and finally comparatively, across seven different Optical Water Types, (OWTs). In the work, the Quality Water Index Polynomial (QWIP) [19] is also included to perform a spatial analysis (per image, per AC processor) to identify Rrs spectra that fall outside the general trends observed in aquatic optics for the entire water surface, and hence not limited to the small area corresponding to *in situ* location.

We also include intercomparisons and evaluation of four different AC methods applied to EnMAP (the Environmental Mapping and Analysis Program) [20,21] data which is an advanced Earth observation satellite funded and operated by the German Aerospace Center (DLR) since April 2022. Since the

mission is much younger than PRISMA, less matchups with *in situ* data are available and only four different AC methods are considered in this report. The evaluation of the data by *in situ* data takes advantage mostly of the same sites as used for the PRISMA evaluation. The data, methods, results and discussion of the EnMAP AC evaluation is based on the study by [22] which focuses on 2022-2023 matchups only and was complemented by the recently developed atmospheric correction method PACO-WASI.

In addition to the presented Section 2, the report is composed by Section 3, which presents the *in situ* and satellite data and the AC models applied to both PRISMA and EnMAP. In Section 4 and Section 5 the report presents the results of PRISMA and EnMAP separately, for the sake of clarity. Section 6 is based on the conclusions and combining the results of PRISMA and EnMAP.

4 MATERIALS AND METHODS

4.1 *IN SITU* DATA

In order to validate satellite mission data, it is essential to have a large amount of *in situ* data, collected at the same time as the satellite overpasses [18]. This section introduces the *in situ* data used to carry out this work: global networks, fixed radiometer data and fieldwork data, as presented in Table 2. The data are presented similarly to those provided in ACIX-Aqua, for purposes of continuity across the two exercises.

Table 2 In situ data used in the study, percentage of location in inland and coastal waters (the % are computed with respect to the number of sites for each of the instruments). * highlights *in situ* data only used for matchups in the EnMAP data evaluation.

Network	<i>In situ</i> instrument	Example of instrument use	Characteristics	Location and representativeness of the system
AERONET-OC	CIMEL CE-318T	[23]	Fixed radiometer, multispectral data	85% coastal waters 15% inland waters
COMMUNITY VALIDATION DATABASE (CVD)	WISPSStation	[11]	Fixed radiometer, hyperspectral data	100% inland waters
	PANTHYR	[24]	Fixed radiometer, hyperspectral data	100% coastal waters
	THETIS	[25]	Fixed radiometer, hyperspectral data	100% inland waters
	HYPSTAR	[26]	Fixed radiometer, hyperspectral data	67% coastal waters 34% inland waters
	WISP-3	[4]	Ad-hoc campaigns, hyperspectral data	75% inland waters 25% coastal water
	Hyper-Pro*	[27]	Ad-hoc campaigns, hyperspectral data	100% oligotrophic water
	Satlantic HyperOCR*	[28]	Fixed radiometer, hyperspectral data	100% coastal water
	OOSS*	[22,29]	Ad-hoc campaigns, hyperspectral data	100% inland waters

4.1.1 AERONET-OC NETWORK

Several protocols can be followed for validation activities, the most common of which is the global multispectral network AERONET-OC [23,30]. The network covers over 40 aquatic sites worldwide, each with different optical characteristics. The main advantages of the network are autonomous operation and data availability within hours of collection, high quality and consistency of data due to standardised collection methodology, annual instrument calibrations and data re-processing techniques, and open access products through a specific data policy. AERONET-OC provides measurements of normalised water radiance (LWN) measured by modified CIMEL (Paris, France) CE-318T solar photometers installed on fixed offshore platforms, multispectral data in the spectral range 400-1020 nm (~10 nm bandwidth). Previously, AERONET-OC supported the radiometric characterisation of Landsat-8 OLI and Sentinel-2 MSI for aquatic applications, with the previous ACIX-

Aqua exercise [18]; in this report it is used for the assessment of PRISMA and EnMAP hyperspectral data.

4.1.2 COMMUNITY VALIDATION DATABASE

The global AERONET-OC network valuably provides a global coverage of water sites (mostly marine, with lakes are still underrepresented) in a multi-spectral setting, while the availability of equivalent data in a hyperspectral band setting remains rather limited. As for ACIX-Aqua, in this work, the dataset collected by the CVD was hence exploited along with the AERONET/OC. The CVD is the result of a collaboration of different scientific teams that provided *in situ* hyperspectral data to validate the different AC models. In particular, the following fixed position autonomous radiometers deployed to collect either above or underwater measurements were used in the study: WISPStation [11], Hypstar [26,31], Panthyr [24,32], HyperOCR [28] and Thetis [25]. Furthermore, CVD includes also data collected by the following hand-held spectroradiometers used during fieldworks: Hyper-Pro [27], OOSS [29] and WISP-3 [4,33]. All data were supplied by providers in physical units of above water Rrs (sr^{-1}).

4.2 ATMOSPHERIC CORRECTION MODELS

This section presents the characteristics of the different AC models. A summary of the main features is given in Table 3.

Table 3 Table 3 Main characteristics of the AC models and T-Mart model. Notably ACOLITE, POLYMER and MIP are applied to both PRISMA and EnMAP; hGRS, iCOR and T-Mart only to PRISMA; PACO-WASI only to EnMAP.

AC model	ACOLITE	hGRS	POLYMER	iCOR	MIP	PACO-WASI	T-Mart (adjacency-effect correction only)
Gaseous	O2, O3 (OMI)	O2, O3, O4, NO2, CO, CO2, CH4 (from CAMS)	O3 and NO2	O2, O3, NO2, CO, CO2, CH4 (O3 climatology)	O2, O3, CO, CO2, NO, NO2, CH4, SO2	H2O, O3, CO2, CO, CH4, N2O, O2, NH3, NO, NO2, So2, HNO3	MERRA2
Water vapor	NCEP	ECMWF/CAMS	No	ECMWF (OLI) [34]	No	Yes [34]	MERRA2
Sun-glint	Fit to residuals at <i>prc</i> (1609) & <i>prc</i> (2200)	Optimal estimation from SWIR bands	Treated as bulk signal	Subtraction of minimum	Implicit	[35]	No
Sky-glint	[36]	through radiative transfer LUT	No	[37]	[35]	No	No
Adjacency effects	No	No	No	SIMEC [38]	[39]	Yes [40]	[41]
Aerosol	Dark target approach (area-based)	Optimal estimation with OPAC models	Polynomial fitting (per-pixel)	Dark target and AOT multi-parameter inversion	Pixel-wise coupled retrieval	Dark Dense Vegetation and dark target approach (area / scene based)	MERRA2

				(area-based)			
Rayleigh LUT	6SV [42]	Coupled Rayleigh-aerosol diffuse radiance LUT	SOS [43]	MODTRAN 5.0 [44]	Contained in fully coupled model	MODTRAN 5.4 [44]	Not applicable
Geometry	Scene center for OLI and 5-km grids for MSI	Per-pixel	Per-pixel	Per-pixel	Per-pixel	Per-pixel	Scene center
Aerosol model	Continental/maritime aerosols [42] [42]	OPAC	No	MODTRAN rural models [44]	modified Shettle Fenn	MODTRAN rural models [44]	Linearly mixed continental/maritime aerosols [42]
Cloud masking	$\rho t(1609) > 0.0215$	Thresholds on several spectral normalized indexes and bands around 2200 nm	$\rho t(865) > 0.2$	Cloud mask layers are provided [45]	Decision Tree based on spectral and spectral indice thresholds	Thresholds on several spectral normalized indexes	Not applicable
Output grid cell size (m)	10	30	10/20/60	60	30	Same as L1 data	Same as input
Assumptions on bio-optical conditions	No	No	Yes [46]	No	No	Yes [47]	No
Version	20231023.0	-	-	v3.2	2.3.798	EnMAP 01.05.02 (PACO), 7 (WASI)	2.2.2
Open source access	Yes (ACOLITE)	No (Under construction)	Yes (POLYMER)	No	No	No (PACO) Yes (WASI)	Yes (T-Mart)
Organizations	RBINS	Magellium	HYGEOS	VITO	EOMAP	DLR	University of Ottawa
References	[48,49]	[50]	[51,52]	[45]	[39]	[47,53,54]	[41]

4.2.1 ACOLITE

ACOLITE, developed at Royal Belgian Institute of Natural Sciences, is a software developed for the AC of satellite images for aquatic applications. It is applicable to images acquired by numerous satellite sensors, among which Landsat 8/9 [55], Sentinel-2 MSI [48,56,57] and Sentinel-3 OLCI [58] and to data acquired by several hyperspectral missions, including PRISMA [24] and EnMAP [22]. ACOLITE is available on GitHub² and in this study the version 20231023.0 has been used, without and with the option of glint correction. ACOLITE is based on the Dark Spectrum [48,57] in which multiple dark targets in the scene or subscene are chosen to construct a dark spectrum. This is then used to estimate the AOT at 550 and atmospheric path reflectance according to the best-fitting aerosol model. The AOT and aerosol type were imposed to be fixed over the 30 × 30 km PRISMA acquisition. ACOLITE used the Continental and Maritime aerosol models from 6SV. For ACOLITE DSF processing both a PRISMA L1 image and the matching L2C data are required as inputs. At runtime, band specific

² <https://github.com/acolite/acolite>

Gaussian relative spectral response functions are generated for both VNIR and SWIR detectors, using the central wavelength and FWHM information provided in the HDF5 metadata. Geometry information is currently not included in the L1 data, and hence the per-pixel sun and view geometry (i.e. sun and view zenith and relative azimuth angles) is extracted from the matching L2C file. Rrs is output by dividing the corrected water reflectance by π . Hereafter we will refer to Rrs obtained from the ACOLITE AC of PRISMA L1 as ACOLITE DSF. In addition to the DSF procedure, ACOLITE has an optional image-based sun glint correction [48]. This correction is performed by estimating the interface reflectance signal in the SWIR from the average ps between 1500 and 2400 nm - i.e. assuming zero water leaving radiance in this spectral range. To extend this average SWIR observation towards the VNIR, the interface reflectance is modelled with OSOAA [59] for the current scene average sun-sensor geometry, the estimated aerosol model and AOT for a high (20 m s^{-1}) wind speed. Remote sensing reflectance is output by dividing the air–water interface reflectance corrected water reflectance by π .

4.2.2 hGRS

The processor hGRS is a hyperspectral adaptation of the previous Glint Removal for Sentinel-2-like (GRS) algorithm which was developed to handle proper correction for the sunglint signal [50] and was evaluated through the previous intercomparison exercise ACIX-Aqua [18]. The new hyperspectral algorithm hGRS provides a two-step algorithm with (i) a correction for the gaseous absorption followed by (ii) a coupled correction of the atmospheric effect (with aerosol estimation) and the reflection of the sun on the water surface (sunglint). Note that this correction for sunglint is of utmost importance for high-spatial resolution and nadir-viewing sensors such as PRISMA for which the sunglint signal might be severely pronounced. The proposed implementation for the gaseous absorption is based on the LibRadTran package. The hyperspectral atmospheric transmittance was precomputed at 0.1-nm spectral resolution for various concentrations of each absorbing gas (O_3 , O_2 , water vapor, CH_4 , CO_2 ...). Based on those pre-computed transmittances the final gaseous transmittance is computed from the gas concentration values taken from the CAMS database and then convoluted with the spectral response functions of the PRISMA sensor. As to the aerosol component of the signal, the radiative modeling is based on the models from the Optical Properties of Aerosol and Clouds (OPAC), version 4. Those aerosol models are built upon the OPAC database [60] encompassing spectral complex refractive index, size distribution, hygroscopicity changes and non-spherical particles. Aerosol models are generated based on a mixture of pure single components. One advantage of those models is to consider the spectral variation of the complex refractive index of the individual aerosols. the scattering matrix based on Mie theory for homogeneous sphere, T-matrix for ellipsoidal/spheroidal particles; those computations were extended for large particle sizes with the “Improved Geometric Optics Method” [61]. The computations were performed through the MOPSMAP package (Modeled optical properties of ensembles of aerosol particles) based on pre-computed look-up tables [62]. These aerosol optical properties LUT were used to generate the intrinsic reflectance of the atmosphere and the total Rayleigh-aerosol transmittances through the full vector radiative transfer code OSOAA [59]. The aerosol content, water vapor and sunglint component are finally

retrieved from the optimal estimation using the Levenberg-Marquardt approach providing the final information for AC and associated uncertainty pixel-wise.

4.2.3 POLYMER

The POLYMER processor, developed by HYGEOS, is an AC algorithm purposely developed for retrieving the ocean colour when the observation is contaminated by the sun glint [51,52]. It has been developed for MERIS on Envisat and is currently applicable to images acquired by other sensors: MODIS Aqua, SeaWiFS, VIIRS, Sentinel-3 OLCI, Sentinel-2 MSI, PRISMA, HICO and EnMAP. POLYMER is available on GitHub³ and in this study the version 4.17beta2 has been used. The POLYMER algorithm uses the image bands in the whole spectral range from the blue to the near infrared, to decouple the atmospheric and surface components of the signal from the water reflectance. The bands near strong atmospheric absorption features are filtered out. The algorithm relies on two models, an analytical model for the atmosphere which uses a second-order polynomial formulation with respect to the wavelength, and a water reflectance model based on two parameters, one for the chlorophyll concentration and one for the backscattering coefficient. The latter is based on the bio-optical model of [46]. Water-leaving reflectance is further normalised to the nominal wavelength and for the water-leaving reflectance bidirectional effects (BRDF), such that the radiometric output of Polymer is the fully normalised water-leaving reflectance spectrum corrected for bidirectional effects. Detailed information on the pre-correction (e.g., estimation of the gaseous transmittance, Rayleigh scattering, and pre-glint correction), spectral matching, and the atmospheric model was presented in [51,52]; information on the water-leaving reflectance model can be found in [46] and its modifications, water-leaving reflectance normalisation, and BRDF correction were described in [52]. Rrs is output by dividing the corrected normalised water-leaving reflectance by π .

4.2.4 iCOR

iCOR (image CORrection for atmospheric effects) is a MODTRAN-5-based AC tool designed to process satellite data collected over coastal, inland, or transitional waters and land [45]. Basic iCOR versions for Landsat-8, Sentinel-2, and OLCI-Sentinel-3 are publicly available as free plugins for the SNAP toolbox. For ACIX-III-Aqua, an advanced version of iCOR has been developed to enable the correction of hyperspectral PRISMA data. Starting from PRISMA TOA data, iCOR identifies land, water, and cloud pixels through a sensor-specific thresholding approach. The AOT values are then retrieved from the image using iCOR's image-based AOT retrieval method. When cloud cover is too extensive, or the scene lacks sufficient spectral variability for accurate AOT retrieval, an automatic fallback mechanism uses Near-Real Time (NRT) AOT values from the Copernicus Atmospheric Monitoring Service (CAMS). Water vapor retrieval is performed directly from PRISMA imagery using the Atmospheric Pre-corrected Differential Absorption (APDA) approach [34]. Additionally, SIMEC adjacency correction [38] is applied to minimize adjacency effects, especially near land-water

³ <https://github.com/hygeos/polymer>

boundaries. Following AOT retrieval and adjacency correction, spectral bands are atmospherically corrected using pre-calculated MODTRAN-5 look-up tables (LUTs). These LUTs incorporate (1) solar and viewing geometry, (2) terrain altitude from the GLOBE DEM, (3) the retrieved AOT values, (4) water vapor concentrations, and (5) monthly ozone climatology data from the Total Ozone Mapping Spectrometer (TOMS). Finally, for water pixels, a Fresnel reflectance correction is applied, while land pixels are modelled as Lambertian surfaces. To address uncertainties in Fresnel correction related to glint and haze, the minimum water-leaving reflectance in selected NIR-SWIR bands is calculated for each water pixel. This value, if greater than zero, is subtracted from the retrieved water-leaving reflectance values across all spectral bands.

4.2.5 MIP

MIP is an operational processing chain that is in principle sensor-independent. It is optimized to most accurately predict in water properties and uses a coupled atmosphere-water model stored in a lookup-table. An inversion algorithm searches for the most likely set of model parameters that explain the observed sensor radiances. Those parameters include surface altitude, geometry, aerosol properties, water ingredient concentrations and water surface roughness. Except for the adjacency correction, the parameters are retrieved pixel-wise. Reflectance products are not directly used in the retrieval process, but are a side product that can be reconstructed using the retrieved atmospheric and water surface properties and propagating those through the radiative transfer simulation. To produce water reflectance data, the chain creates a pixelwise classification into land/water/cloud. It removes the adjacency effect that land pixels have on water and then retrieves all relevant parameters for each water pixel. From those parameters the reflectance products can be created using the method mentioned above.

4.2.6 PACO-WASI

For the EnMAP satellite data only, a combination of two software tools, PACO and WASI, was applied. The EnMAP Level-2A data can be downloaded as water product, processed using MIP, as land product, processed using PACO, or as a combined product. PACO-WASI refers to the postprocessing of the land product with the software WASI to convert surface reflectance to remote sensing reflectance. PACO (Python-Based Atmospheric Correction, [53]) is the Python version of the software package ATCOR [40,63] which is optimized for the atmospheric correction of multi- and hyperspectral satellite and aerial images over land surfaces. It makes use of precomputed lookup tables, generated with Modtran 5.4, and accounts for ground effects such as terrain elevation and adjacency effects. The resulting Level-2A product is Hemispherical Directional Reflectance (HDR) at bottom of atmosphere, commonly called surface reflectance. WASI (Water Color Simulator) is a software designed for the simulation and data analysis of spectral measurements in and above water. It can be downloaded from [54]. Originally developed for field spectrometers [64], WASI has since been adapted to process multi- and hyperspectral image data over water from any sensor [47]. The input

data must be atmospherically corrected and can be in units of reflectance or radiance. The simulation of remote sensing reflectance is based on the analytical models of [65] for optically deep and shallow waters, which had been developed using radiative transfer simulations with Hydrolight [66]. The reflections at the water surface are simulated using the model of [67] which decomposes the sky radiance reflected in sensor direction into three spectrally different components originating from the sun (sun glint), scattering at molecules (Rayleigh glint) and scattering at particles (aerosol glint). The wavelength-dependent glint components are parameterized in terms of aerosol optical thickness, Angström exponent of aerosol scattering, water vapor and ozone scale height using the irradiance model of [68]. All model parameters are experimentally accessible and all files specifying the optical properties of the components in the water and the atmosphere can be exchanged easily, hence WASI allows the simulation of measurements for a wide range of environmental conditions. Data analysis applies inverse modelling (IM) to spectral measurements, and in case of image data, it additionally employs a neural network (NN) that is trained image-specifically using the IM results from a representative subset of several hundred pixels. The flexibility of WASI allows a regional fine-tuning of the simulations and of data processing, which can provide more accurate results compared to global algorithms, yet the optimization of IM for the actual conditions requires expert knowledge. Since the same physical processes are responsible for path radiance and sky glint, IM cannot distinguish between path radiance errors from atmospheric correction and sky glint, which has the advantage for the derivation of remote sensing reflectance that both effects are corrected together. The glint correction algorithm is described in [35]. In the combined PACO-WASI workflow, PACO is first applied to correct the atmosphere, followed by WASI, which processes the surface reflectance output of PACO to correct for sun glint, sky glint and path radiance errors. It is important to note that PACO-WASI is not yet an operational workflow as the step of inverse modelling requires manual fine-tuning of WASI for each individual scene by an experienced user. This tuning process involves iterative adjustments to the IM settings – including the selection of fit parameters, initial values of fit parameters, and spectral range used for data processing – until two criteria are fulfilled: (1) the modelled spectra fit the surface reflectance spectra as close as possible, (2) the noise caused by spectral ambiguities is minimized. Spectral ambiguities, which are a common problem in optically complex waters [69], are identified using correlation plots of pixels that have been processed using both IM and NN approaches; these diagnostic plots are generated automatically by WASI. An automatization of these fine-tuning steps is currently under development.

4.2.7 ACOLITE-T-Mart

As mentioned earlier, in addition to the five AC models, the correction of the adjacency effect using T-Mart combined with ACOLITE was included. In particular, in this exercise, a pre-processing step using T-Mart [41,70] was applied to correct for the adjacency effect at the TOA level, followed by ACOLITE AC (version: 20231023) with the same setting as the ACOLITE-only implementation. T-Mart adjusts the TOA reflectance for each spectral band to satisfy the homogeneous-surface assumption, i.e. pixels are corrected to the TOA reflectance they would exhibit if each pixel were surrounded by pixels of

identical reflectance. The correction process begins by calculating the atmospheric point spread function (PSF) specific to an image's solar-sensor geometry, followed by convolving the image with the PSF as the kernel. The difference between the original and convolved images is scaled, based on radiative transfer simulations, by a factor that approximates the ratio of upward diffuse to upward direct transmittance. The scaled difference is then subtracted from the original image, followed by a matrix multiplication that accounts for variations in surface-level irradiance due to surface heterogeneity using a scene-specific look-up table, to finalize the adjacency effect correction [41]. When computing the PSFs and scaling factors in T-Mart, the atmospheric composition, including ozone, water vapor, and aerosol properties from the GMAO MERRA2 reanalysis data [71], is used to characterize the optical properties of the atmosphere at various altitudes via the 6S radiative transfer model [72].

5 PRISMA DATA ANALYSIS

PRISMA (PRecursore IperSpettrale della Missione Applicativa) is an advanced Earth observation satellite funded and operated by the Italian Space Agency (ASI). Launched on 22nd March 2019 aboard the Vega rocket, PRISMA orbits in a low Earth Sun-synchronous orbit at an altitude of approximately 614.8 km [24,73–77]. It is designed to revisit the same area every 29 days, though this period can be reduced to less than one week using off-nadir pointing capabilities. This flexibility allows PRISMA to capture specific areas more frequently, making it suitable for diverse environmental monitoring applications. The PRISMA payload is a combination of two key instruments: a hyperspectral sensor with a Ground Sampling Distance (GSD) of 30 meters, and a panchromatic (PAN) camera with a GSD of 5 meters. The hyperspectral sensor captures data in 238 contiguous spectral bands ranging from 400 to 2500 nm, enabling precise detection of features across the visible, near-infrared (VNIR), and short-wave infrared (SWIR) regions. This imaging spectrometer creates a hyperdata cube, allowing for detailed analysis of spectral and spatial features in a wide range of environmental contexts. Meanwhile, the PAN camera provides high-resolution context for the hyperspectral data, aiding in applications that require finer-scale mapping. PRISMA's system can acquire, downlinking, and archiving up to 200,000 km² of hyperspectral and panchromatic images daily, covering areas between 70°S and 70°N in latitude and from 180°W to 180°E in longitude. In a single pass, it can capture images up to 1000 km apart by adjusting its viewing angles. This flexibility enhances its temporal resolution, which is crucial for tracking dynamic environmental changes over time. PRISMA products range from Level 0 (L0) to Level 2 (L2): L0 represents formatted data products, Level 1 (L1) represents radiance data radiometrically corrected and calibrated in physical units, and L2 represents the result of the conversion of Top-of-Atmosphere (TOA) spectral radiance measurements into Bottom-of-Atmosphere (BOA) remote sensing reflectance measurements. L2 data are divided into:

- L2B (geolocated ground spectral radiance product);
- L2C (geolocated at-surface reflectance product);
- L2D (the geocoded version of L2C products).

The AC process is described in section 2.2.1 PRISMA mission is recognized for its potential in various domains, including agriculture, forestry, mining, and aquatic remote sensing. Its data is particularly valuable for algorithm development and innovative environmental monitoring techniques.

5.1 FEATURES OF THE PRISMA DATASET USED IN THE EXERCISE

The data used in the exercise are the PRISMA L1 data (version 4.1-0) and PRISMA L2C data (version 02.05). The quality of L1 data was assessed in [73] by comparison with TOA radiances simulated with a radiative transfer code, from *in situ* measurements, obtained from a series of fixed-position autonomous radiometers. The results showed that PRISMA provides TOA radiances with the same amplitude and shape as those simulated *in situ* with slightly larger uncertainties at shorter

wavelengths. The AC process to generate L2C data starting from L1 data is based on the MODTRAN v 6.0 radiative transfer model, uses look-up tables (LUTs) to remove atmospheric distortions, leveraging auxiliary data such as solar irradiance and digital elevation models. PRISMA's automatic correction algorithms are optimized for land applications, though they are sometimes limited in aquatic environments due to the use of a "rural" aerosol model in the LUTs, rather than a "maritime" model more suited for coastal areas. Water vapor and AOT are estimated using the Dense Dark Vegetation (DDV) algorithm, with hyperspectral bands aiding in these retrievals.

5.2 MATCH-UPS ANALYSIS

This section presents the dataset used for the analysis conducted to evaluate the performance of the different AC models. For the comparison with both AERONET-OC and CVD data, the mean Rrs from PRISMA products was extracted based on a 5 x 5 pixels Region Of Interest (ROI) [78], centered around the *in situ* station. To ensure the reliability of the results, the Rrs values of the ROIs were filtered to obtain spatial homogeneity, removing measurements of insufficient quality (similarly to [24]). A ± 1 h time window was considered in accordance with [23], with the exception of the AERONET-OC sites where no data were available closer in time to the satellite acquisition (time window extended to maximum ± 4 h, around 15% of the dataset).

In situ Rrs data were mostly operating from 400 to 800 nm, a wavelength range that is covered by 43 PRISMA bands, between 406 and 796 nm. Within this range there are six predefined bands (reported in Table 4) that are common to AERONET-OC, CVD and PRISMA. These bands were used in the match-up analysis, for which the statistics are presented in section 2.4.3; the entire spectrum range was considered for the hyperspectral CVD dataset. For this purpose, the higher spectral resolution of the CVD data was spectrally resampled according to the full width at half maximum (FWHM) of the PRISMA products. For AERONET-OC, the *in situ* Rrs data were assumed to be directly comparable to the PRISMA data, since both sensors have a bandwidth of ~ 10 nm, despite their band centers differing by a few nanometers (up to 4.7 nm).

Table 4 shows the band setting across the different datasets: the nominal band that is used in the match-up analysis (e.g., computation of the statistical metrics and scatterplot between *in situ* and PRISMA reflectance data at a given band) is provided along with the corresponding AERONET-OC and PRISMA band settings (notably, the central wavelengths of PRISMA channels do not necessary match the nominal bands).

Table 4 Band settings in the different datasets: the nominal band used in the match-up analysis and the corresponding band settings of AERONET-OC and PRISMA.

	Nominal band	AERONET-OC band setting	PRISMA band setting
AERONET-OC & CVD datasets	443 nm	443 ± 5 nm	446.0 ± 4.6 nm
	490 nm	490 ± 5 nm	489.8 ± 4.5 nm
	560 nm	560 ± 5 nm	559.0 ± 5.0 nm

	620 nm	620 ± 5 nm	618.7 ± 5.5 nm
	667 nm	667 ± 5 nm	664.9 ± 5.9 nm
	709 nm	709 ± 5 nm	713.7 ± 6.2 nm

5.2.1 DATASET

A graphical representation of the dataset used in this study is shown in Figure 1: empty dots indicate study areas with *in situ* data from the AERONET-OC network, while filled dots indicate those from the CVD network.

The PRISMA images were selected based on the synchronicity with the *in situ* data and the percentage of cloud coverage, which was required to be less than 2%. The dataset consists of 174 images with *in situ* data derived from the AERONET-OC network (21 sites) and 65 images with *in situ* data obtained from the CVD network (six sites), for a total of 239 images.

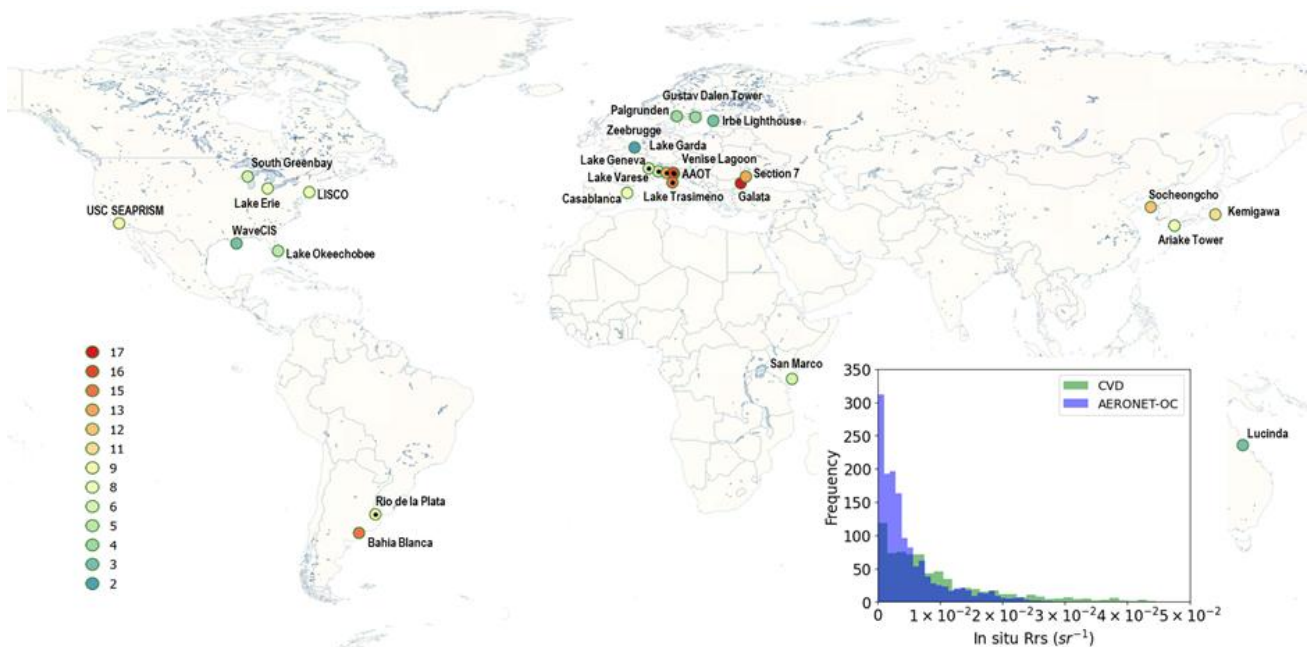


Figure 1 Dataset of the globally distributed sites and number of available match-ups between PRISMA and field data. The colour of the dots indicates the number of available match-ups ranging from a minimum of 1 to a maximum of 17 for every study area. The Location of AERONET-OC are indicated with circles only, the black dots indicate CVD sites; Rio de la Plata and AAOT (Venice) are both AERONET-OC and CVD. The bottom-right bar plot shows the frequency distribution of R_{rs} on the y-axis, with the values in sr^{-1} reported on the x-axis. This is shown for both multispectral (AERONET-OC, light blue) and hyperspectral (CVD, green) *in situ* data collection. The darker blue area shows the overlap between the two distributions. (Image taken from Figure 1 [79]).

5.2.2 PERFORMANCE ASSESSMENT

The performance analyses are described in two main subsections: a) per site assessment considering AERONET-OC and CVD networks separated and b) OWTs analysis of all test sites aggregated. To perform the latter, the entire *in situ* dataset was divided into OWTs allowing an assessment of AC processors across widely variable coastal and inland water conditions. To do this, 10 reference OWTs, shown in Figure 2 along with their description in Table 5, were selected among the ones proposed by

[80]. After the identification of the most significant OWTs in accordance with the dataset, the spectral signatures of both AERONET-OC and CVD networks were resampled at their same spectral configuration; to assign each of them to the 10 OWTs, the spectral similarity (SA) has been calculated.

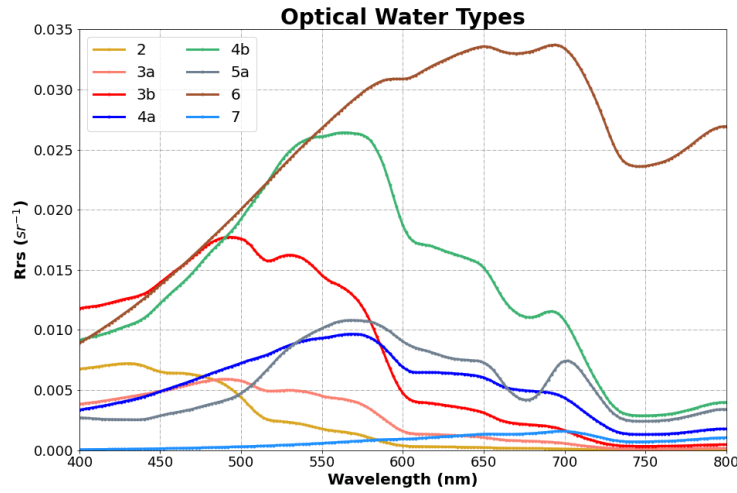


Figure 2 Reference OWTs for the different AC models performance assessment [80].

Table 5 Conceptual description of OWTs [80].

2	Blue waters with low detritus content and CDOM.
3a	Turquoise waters with slightly higher phytoplankton, detritus, and CDOM compared to the first type.
3b	A special case of OWT 3a with similar detritus and CDOM distribution but with strong scattering and little absorbing particles like in the case of Coccolithophore blooms. This type usually appears brighter and exhibits a remarkable ~490 nm reflectance peak.
4a	Greenish water found in coastal and inland environments, with higher biomass compared to the previous water types. Reflectance in short wavelengths is usually depressed by the absorption of particles and CDOM.
4b	A special case of OWT 4a, sharing similar detritus and CDOM distribution, exhibiting phytoplankton blooms with higher scattering coefficients, e.g., Coccolithophore bloom. The color of this type shows a very bright green.
5a	Green eutrophic water, with significantly higher phytoplankton biomass, exhibiting a bimodal reflectance shape with typical peaks at ~560 and ~709 nm.
6	Bright brown water with high detritus concentrations, which has a high reflectance determined by scattering.
7	Dark brown to black water with very high CDOM concentration, which has low reflectance in the entire visible range and is dominated by absorption.

5.2.3 STATISTICS

The common statistical metrics were used to assess the agreement of R_{rs} between satellite and *in situ* data. In the following equations, n represents the number of concurrent observations, and x_i and y_i are the sensors-estimated R_{rs} data and *in situ* measurements, respectively. The last metric has been introduced, in line with ACIX-Aqua, for the OWT analysis; to facilitate the comparison of the AC processors across bands and OWTs, a normalized index (Norm(ϵ)) was applied to the values of ϵ .

- Root Mean Square Difference (RMSD)

$$RMSD (sr^{-1}) = \sqrt{\frac{\sum_{i=1}^n (x_i - y_i)^2}{n}}$$

- Mean bias

$$Mean\ bias\ (\%) = \frac{100}{n} \sum_{i=1}^n \frac{x_i - y_i}{y_i}$$

- Mean Absolute Difference (MAD)

$$MAD (sr^{-1}) = \frac{\sum_{i=1}^n |y_i - x_i|}{n}$$

- Bias (β)

$$\beta (\%) = 100 * sign (Median(log_{10}(\frac{x_i}{y_i}))) * (10^{|Median(log_{10}(\frac{x_i}{y_i}))|} - 1)$$

- Median Symmetric Accuracy (MdSA, ϵ)

$$\epsilon (\%) = 100 * (10^{Median|log_{10}(\frac{x_i}{y_i})|} - 1)$$

- Spectral Angle (SA)

$$SA (^\circ) = \frac{\sum_{i=1}^n y_i x_i}{\sqrt{\sum_{i=1}^n y_i^2} \sqrt{\sum_{i=1}^n x_i^2}}$$

- Mean Absolute Percentage Difference (MAPD)

$$MAPD (\%) = \frac{100}{n} \sum_{i=1}^n \left| \frac{x_i - y_i}{y_i} \right|$$

- Normalized Median Symmetric Accuracy (Norm(ϵ))

$$Norm(\epsilon) = \frac{Max(\epsilon) - \epsilon_i}{Max(\epsilon) - Min(\epsilon)} * 100$$

5.2.4 QUALITY WATER INDEX POLYNOMIAL

The Quality Water Index Polynomial (QWIP) approach provides a simple, quantitative tool to evaluate the quality of remote sensing reflectance data [19]. The relationship between the Apparent Visible Wavelength (AVW) [81] and a multi-channel waveband index is used to identify spectra that fall outside the general trends observed in aquatic optics for optically deep waters. The approach was developed with a large global dataset representing blue, green, and brown waters and was further tested extensively with field and satellite datasets. Algorithm Theoretical Basis Documents for both AVW and QWIP methodologies can be found at this link⁴.

⁴ <https://oceancolor.gsfc.nasa.gov/resources/atbd/>

In summary, the AVW is calculated over the reflectance range of 400 – 700 nm as follows:

$$AVW = \frac{\sum_{i=400}^{700} R_{rs}(\lambda_i)}{\sum_{i=400}^{700} \frac{R_{rs}(\lambda_i)}{\lambda_i}}$$

The QWIP score is calculated as the difference between a measured and AVW-predicted normalised difference index (NDI). To initiate, the measured NDI is determined as:

$$NDI = \frac{R_{rs}(\lambda_2) - R_{rs}(\lambda_1)}{R_{rs}(\lambda_2) + R_{rs}(\lambda_1)}$$

where $\lambda_1 = Rrs_489$, and $\lambda_2 = Rrs_664$

The predicted NDI is related to the Apparent Visible Wavelength, described as a polynomial, the Quality Water Index Polynomial (QWIP):

$$QWIP = p_1 AVW^4 + p_2 AVW^3 + p_3 AVW^2 + p_4 AVW + p_5$$

$$p = (-8.399855E^{-09}, 1.715532E^{-05}, -1.301670E^{-02}, 4.357838E^{00}, -5.449532E^{02})$$

Finally, the QWIP score is calculated as the difference between the NDI and QWIP:

$$QWIP\ Score = NDI - QWIP$$

The distance either above or below the central tendency (QWIP) is scored with a positive or negative value. Generally, hyperspectral data with |QWIP| scores exceeding a value of 0.2 may be subject to additional screening to determine any evident spectral anomalies. This simple approach can provide a level of uncertainty about a retrieved spectrum and flag questionable or unusual spectra for further analysis. The QWIP scores were calculated and mapped for all of the processed imagery. A subset of the results and supporting diagnostic tools are presented in this manuscript, but the reader is referred to the supporting online documentation for access to results from all scenes.

5.3 RESULTS

In this section, the results of the spectral comparison between the different models and the *in situ* data (AERONET-OC and CVD) are shown, together with statistics, the performance assessment after dividing the dataset into OWTs and finally the spatial WQIP analysis.

5.3.1 OVER THE SITES

5.3.1.1 AERONET-OC

Figure 3 - Figure 9 show the spectral comparisons between satellite and *in situ* data for the 21 AERONET-OC sites. In this section, results from the comparison of PRISMA standard L2C products, AC models and T-Mart model with *in situ* measurements are presented. Spectral Angles are calculated on the mean spectra. Overall, the R_{rs} spectra of AERONET-OC range from peaks slightly lower than 0.005 sr^{-1} in the blue region to maxima of around 0.025 sr^{-1} in the green region.

A brief characterisation of the sites follows:

- Casablanca platform, Venice, USC SeaPrism and Socheongcho sites, where R_{rs} spectra are higher in the blue region and generally tend to decrease after about 505 nm, represent the typical shape of the clear water spectra. In particular, the Casablanca and USC-SeaPrism spectra represent extremely clear water types with absent CDOM and Chl-a concentration.
- Ariake Tower, Bahia Blanca, San Marco platform, Zeebrugge, Wave CIS, South Greenbay and Kemigawa (lower R_{rs} values) sites, where R_{rs} spectra are higher in the green region (around 560 nm), represent the typical shape of the turbid water spectra. Bahia Blanca site presents the peak in the green region with the highest value of R_{rs} , this site is characterised as an area subject to diffuse erosion and strong tidal currents which are responsible for the typically high suspended loads in the channel.
- In the South Greenbay site, the peak around 710 nm is very evident, compared to the other cases, this could be due to the fact that this site is characterised by a condition of hyper-eutrophication (super-richness of nutrients). A less noticeable peak around 680 nm is also visible in the case of LISCO site.
- In the Lake Erie site, the dip in reflectance around 620 nm may indicate a specific feature of secondary pigments absorption, associated to the presence of phycocyanin (PC).
- In the Palgrunden site the spectra seem to be characterised by the presence of CDOM.
- In the Lake Okeechobee site, the spectra are atypical. This peculiarity of the spectral signature of this lake may be due to its characteristics: a shallow lake with high sediment concentrations near the surface and seasonal cyanobacterial blooms.
- In the Rio de la Plata site, a typical brown spectral water signature is evident, the R_{rs} peak is around 600 nm. This is a highly active area subject to human impact, receiving the discharge of domestic and industrial effluents, which lead to a significant increase in nutrient load, showing symptoms of eutrophication.

- In the Gustav Dalen Tower and Irbe Lighthouse sites, the spectral signatures are similar: peak Rrs ($< 0.005 \text{ sr}^{-1}$) around 550 nm, which then tends to decrease to zero.
- In the Galata platform site, the spectrum is associated with optically complex waters, with Rrs maxima typically observed in the 490-560 nm range, properties common to the Section 7 site).
- In the Lucinda site (in the tropical coastal waters of the Great Barrier Reef lagoon near the Herbert River estuary), the spectrum shows a peak just before 550 nm and a standard deviation of $\pm 0.005 \text{ sr}^{-1}$.

PRISMA L2C

In all cases, an overestimation of the Rrs PRISMA L2C spectra compared to the *in situ* data can be observed; better agreement between satellite data and *in situ* data is seen in more eutrophic waters, where the water-leaving signal is higher. Thus, the lower SA value (8.92°) was identified in the case of the Bahia Blanca site. In more clear waters where there is a low signal, PRISMA's performance is often sub-optimal, as has also been reported in other studies [24]: mean SA $\sim 18^\circ$. For the Lake Erie site, the Rrs PRISMA spectra presents the highest standard deviation ($\pm 0.015 \text{ sr}^{-1}$). In Lake Okeechobee, where pronounced absorption and reflection peaks are observed, there is a low level of agreement ($\text{SA}=32.86^\circ$). The unrealistic spectral variability at some sites (e.g., Casablanca, Galata platform, Socheongcho, USC SeaPrism) should also be noted. This non-physical variability indicates the presence of image artefacts (e.g., scattered light), particularly in the blue part of the spectrum and at sites with low-magnitude spectra (i.e. blue or organic-rich waters). The SA ranges from 8.92° (Bahia Blanca site) to 47.49° (Palgrunden site).

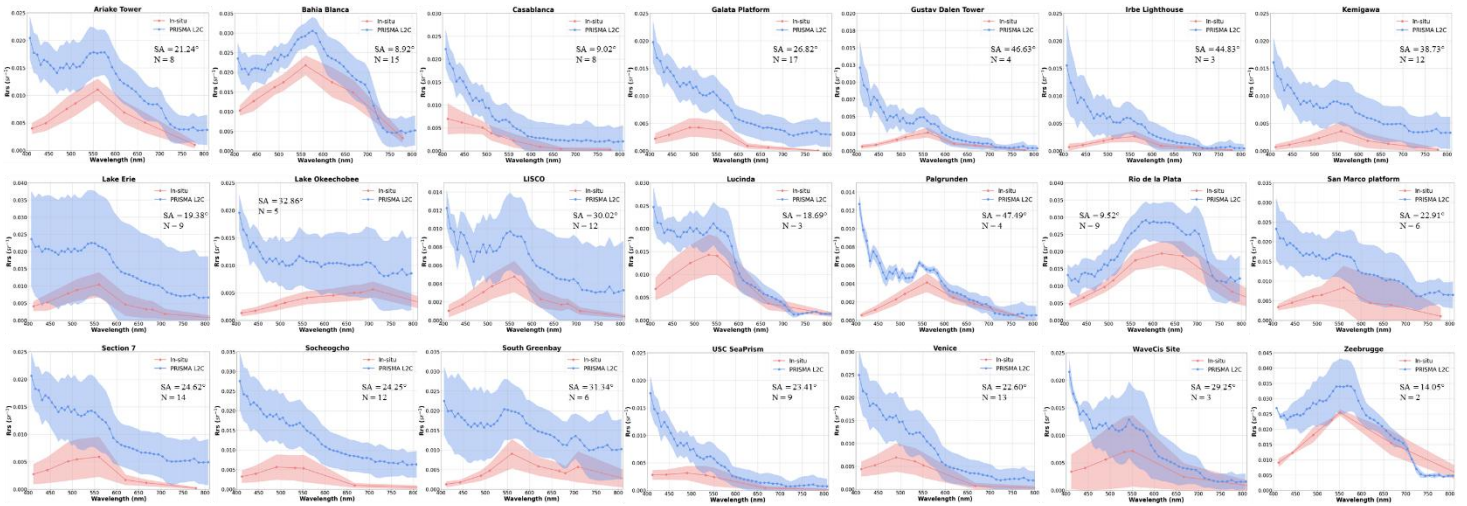


Figure 3 Spectral comparisons between PRISMA L2C and *in situ* data in the 21 globally distributed AERONET-OC sites. The variability across the dataset in the mean spectra of PRISMA L2C is displayed as blue curves, with the shaded blue area representing the standard deviation. The mean and standard deviation of the *in situ* data are equivalently shown in orange. SA represents the Spectral Angle and N represents the number of the images.

ACOLITE

A comparison between ACOLITE and *in situ* data shows a good fit between the data. Particularly in the case of the Bahia Blanca (SA=2.93°), Casablanca platform (SA=8.21°), Lake Erie (SA=10.68°) and Zeebrugge (SA=9.37°) sites. The highest standard deviation values were recorded in the cases of LISCO ($\pm 0.002 \text{ sr}^{-1}$), San Marco platform ($\pm 0.007 \text{ sr}^{-1}$) and South Greenbay ($\pm 0.01 \text{ sr}^{-1}$). The SA ranges from 2.93° (Bahia Blanca site) to 36.98° (Irbe Lighthouse site).

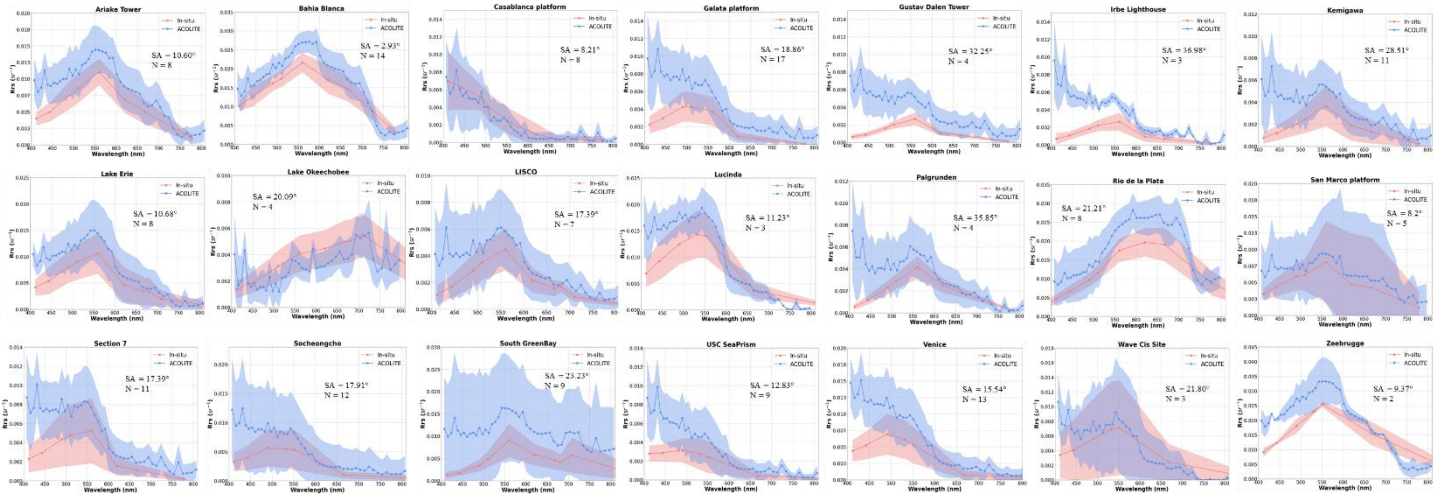


Figure 4 Spectral comparisons between ACOLITE and *in situ* data in the 21 globally distributed AERONET-OC sites. The variability across the dataset in the mean spectra of ACOLITE is displayed as blue curves, with the shaded blue area representing the standard deviation. The mean and standard deviation of the *in situ* data are equivalently shown in orange. SA represents the Spectral Angle and N represents the number of the images.

hGRS

Here, the products obtained by applying hGRS model to satellite data; SA was lower than 20° for the 62% of the study areas. There is high concordance in the NIR region, and some difference with *in situ* data in the blue region. The highest agreement was reached in Bahia Blanca (SA=5.1°), followed by Zeebrugge and Casablanca (both with SA=8.9°). Least agreement was noted in Kemigawa (SA=46.1°), while a good performance can be noted in the case of the South Greenbay site, where a hyper-eutrophic condition (super nutrient richness) is present. In San Marco platform and Lake Erie a high standard deviation was registered ($\pm 0.015 \text{ sr}^{-1}$ and $\pm 0.008 \text{ sr}^{-1}$ respectively).

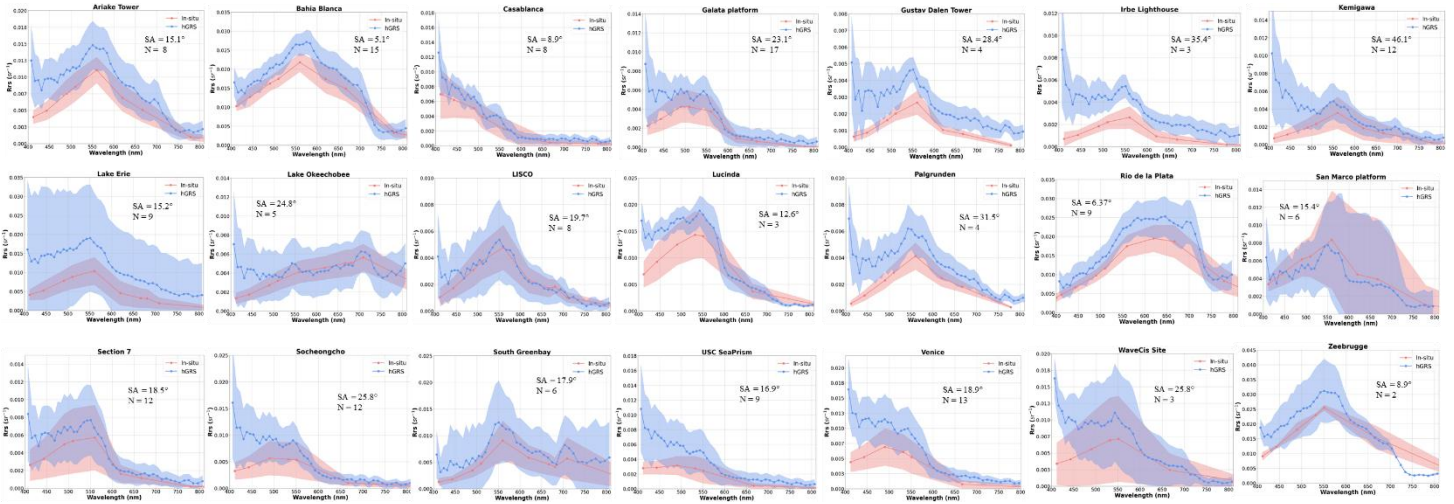


Figure 5 Spectral comparisons between *hGRS* and *in situ* data in the 21 globally distributed AERONET-OC sites. The variability across the dataset in the mean spectra of *hGRS* is displayed as blue curves, with the shaded blue area representing the standard deviation. The mean and standard deviation of the *in situ* data are equivalently shown in orange. SA represents the Spectral Angle and N represents the number of the images.

POLYMER

In the case of POLYMER, there is a good level of agreement with *in situ* measurements, particularly in the case of the Ariake Tower, Casablanca platform, Lake Erie, Lucinda and Rio de la Plata sites, with mean SA = 3.5°. Only in a few cases is the blue spectrum somewhat noisy and there is an overestimation of the *Rrs* spectrum compared to the *in situ* data. In the case of Lake Okeechobee, the result of the comparison is weak. The SA varies from 2.54° (Casablanca site) to 73.33° (Lake Okeechobee site).

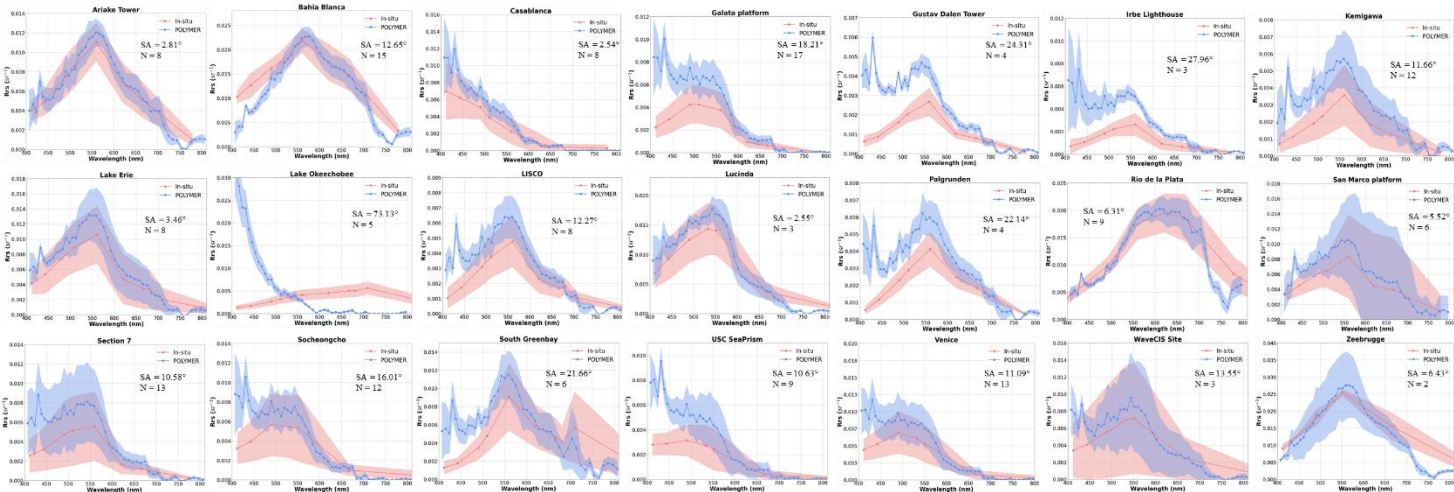


Figure 6 Spectral comparisons between *POLYMER* and *in situ* data in the 21 globally distributed AERONET-OC sites. The variability across the dataset in the mean spectra of *POLYMER* is displayed as blue curves, with the shaded blue area representing the standard deviation. The mean and standard deviation of the *in situ* data are equivalently shown in orange. SA represents the Spectral Angle and N represents the number of the images.

iCOR

The Rrs spectra derived from the correction with iCOR showed a good agreement for all the study areas with *in situ* data. The highest agreement was reached in Zeebrugge (SA=4.87°), followed by Bahia Blanca (SA=6.88°), and Ariake Tower (SA=7.34°), while lower concordance was found in Palgrunden (SA=31.01°). In Lake Erie, LISCO and South Greenbay the reflectance peak, due to the eutrophic conditions of the water, can be noticed (0.007 sr⁻¹, 0.003 sr⁻¹ and 0.012 sr⁻¹ respectively). A standard deviation of about ±0.010 sr⁻¹ was registered in San Marco Platform and Lake Okeechobee.

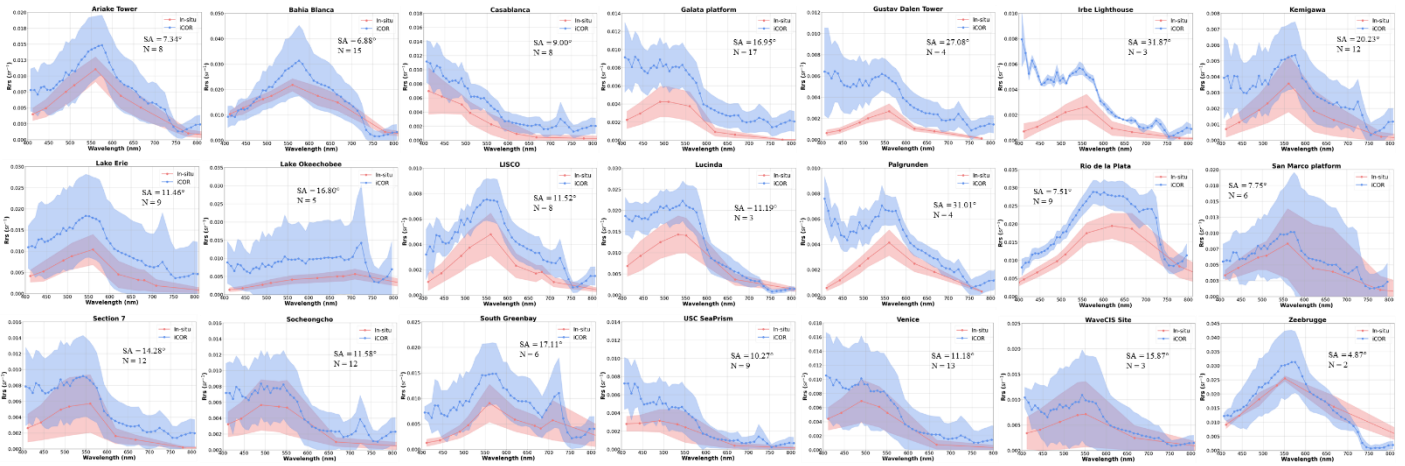


Figure 7 Spectral comparisons between iCOR and *in situ* data in the 21 globally distributed AERONET-OC sites. The variability across the dataset in the mean spectra of PRISMA iCOR is displayed as blue curves, with the shaded blue area representing the standard deviation. The mean and standard deviation of the *in situ* data are equivalently shown in orange. SA represents the Spectral Angle and N represents the number of the images.

MIP

The Rrs spectra derived from the correction with MIP showed a good agreement for all the study areas with *in situ* data (SA lower than 20° for the 75% of the study areas), particularly in the blue region, although this area, together with the NIR spectral region presented some unusual peaks (around 700 nm). The spectral feature at 760 nm is probably due to the oxygen absorption. The SA ranges from 5.02° (Zeebrugge site) to 33.01° (Palgrunden site). In San Marco platform high standard deviation was registered (±0.009 sr⁻¹).

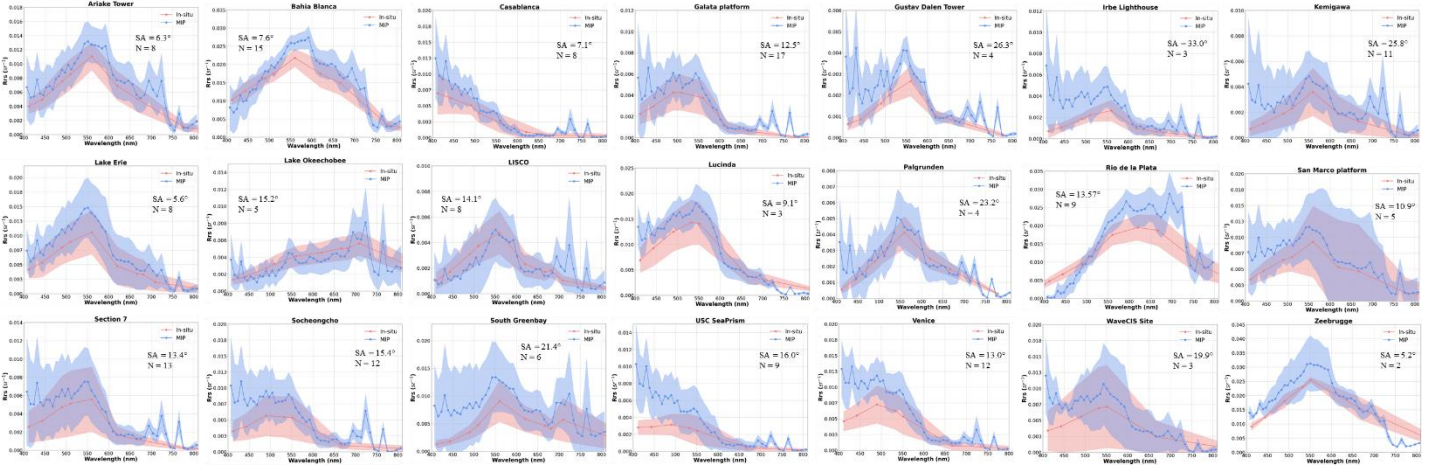


Figure 8 Spectral comparisons between MIP and in situ data in the 21 globally distributed AERONET-OC sites. The variability across the dataset in the mean spectra of MIP is displayed as blue curves, with the shaded blue area representing the standard deviation. The mean and standard deviation of the in situ data are equivalently shown in orange. SA represents the Spectral Angle and N represents the number of the images.

ACOLITE-T-Mart

Similar results (respect to ACOLITE) obtained from the ACOLITE-T-Mart model, there is a slight improvement at sites closer to the coast, i.e. those that may be more subject to the adjacency effect. In fact, the improvement is most noticeable in the cases of LISCO and South Greenbay (distance from the coast of 1.6 and 0.5 nautical miles), SA improved by about 20%. The SA ranges from 2.81° (Bahia Blanca site) to 32.00° (Irbe Lighthouse site).

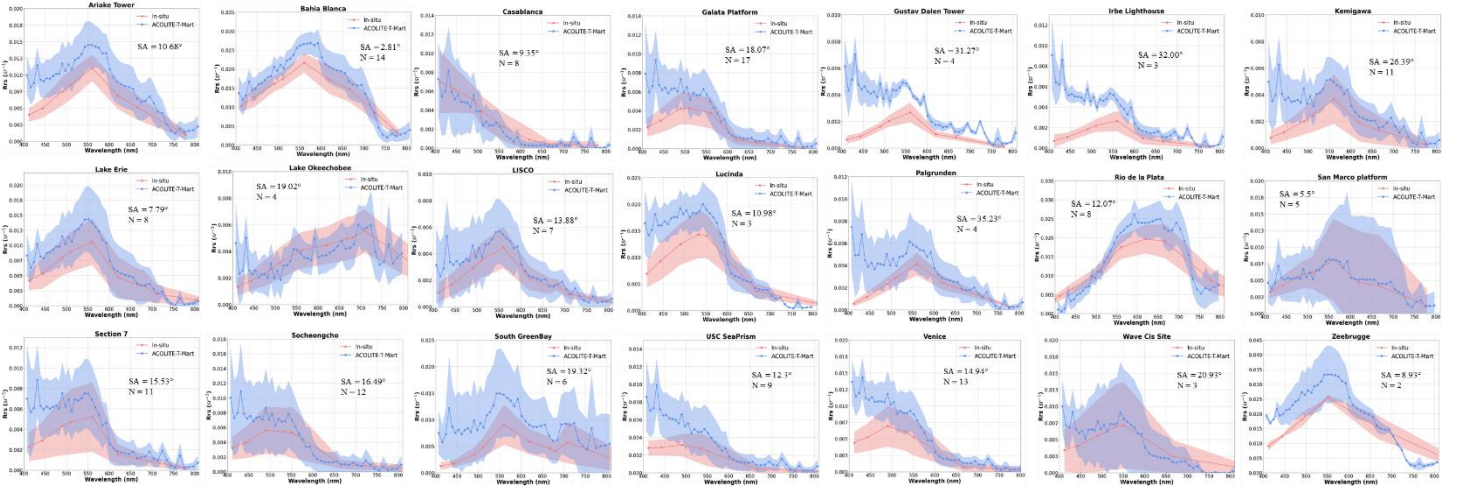


Figure 9 Spectral comparisons between ACOLITE-T-Mart and in situ data in the 21 globally distributed AERONET-OC sites. The variability across the dataset in the mean spectra of ACOLITE-T-Mart is displayed as blue curves, with the shaded blue area representing the standard deviation. The mean and standard deviation of the in situ data are equivalently shown in orange. SA represents the Spectral Angle and N represents the number of the images.

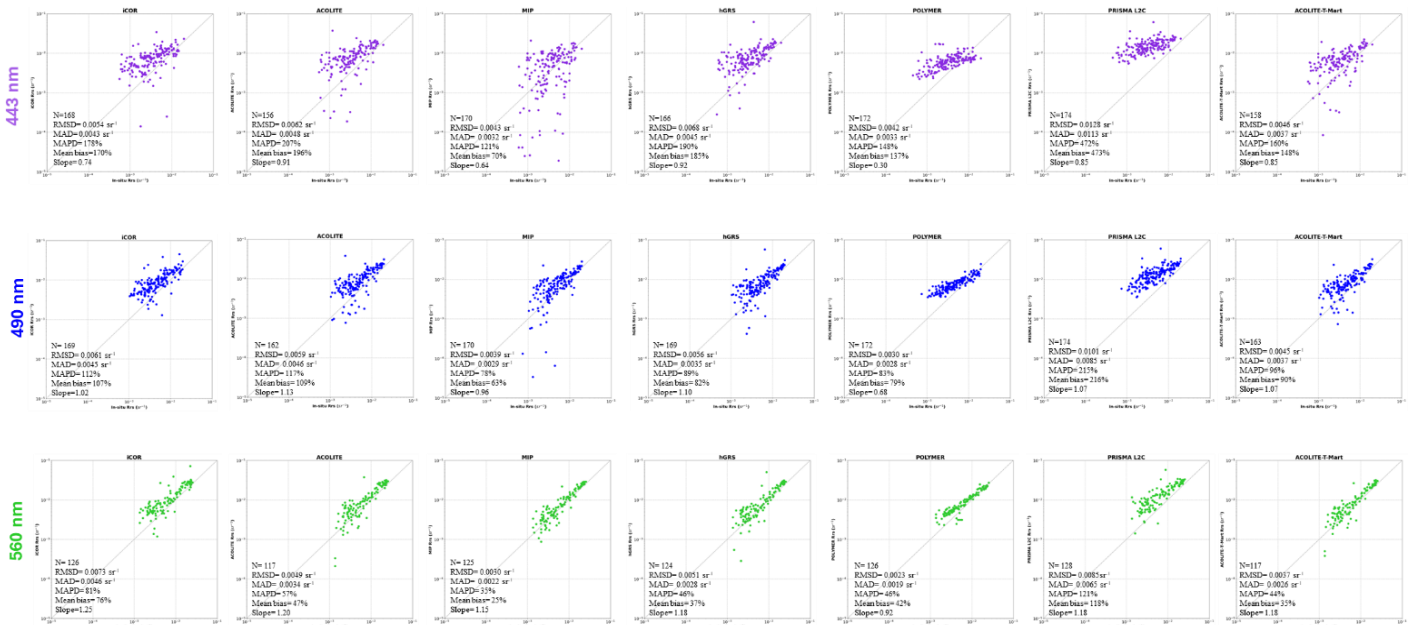
5.3.2 OVER THE SPECTRAL BANDS

After performing the spectral comparison, satellite and *in situ* data from all 21 sites were aggregated by AC model and resampled to the spectral configuration of AERONET-OC, selecting the PRISMA bands closest to the corresponding AERONET-OC bands. Table 6 shows the name assigned to each corresponding band that is used from now on.

Table 6 Band names

Name	b_443	b_490	b_560	b_620	b_667	b_709
Band	443 nm	490 nm	560 nm	620 nm	667 nm	709 nm

Figure 10 shows the scatterplots in the 6 selected bands together with the sample size value (N) and statistics (RMSD, MAD, MAPD, Mean bias, Slope). In general, more dispersion was noted in the UV/blue region, particularly at b_443 (RMSD ranged 0.0042 - 0.0128 sr⁻¹) and b_490 (RMSD ranged 0.0030 - 0.0101 sr⁻¹). Good fitting at b_560 (RMSD ranged 0.0023 - 0.0073 sr⁻¹) and b_620 (RMSD ranged 0.0018 - 0.0076 sr⁻¹). Slight dispersion in the case of the red band at b_667 (RMSD ranged 0.0014 - 0.0065 sr⁻¹). The dispersion at b_709 may also be due to the presence of few samples (RMSD ranged 0.0019 - 0.0099 sr⁻¹). For all bands POLYMER showed the lowest RMSD values, followed by MIP (better performance at b_443). Slightly higher RMSD values in the case of ACOLITE-T-Mart and hGRS (lowest values at b_490). The sample size (N) changes at different wavelengths due to the different configurations of the *in situ* instruments; for the same wavelength, it also changes depending on the model due to the presence of negative values (removed from the analysis) and the complete non-return in output of the product.



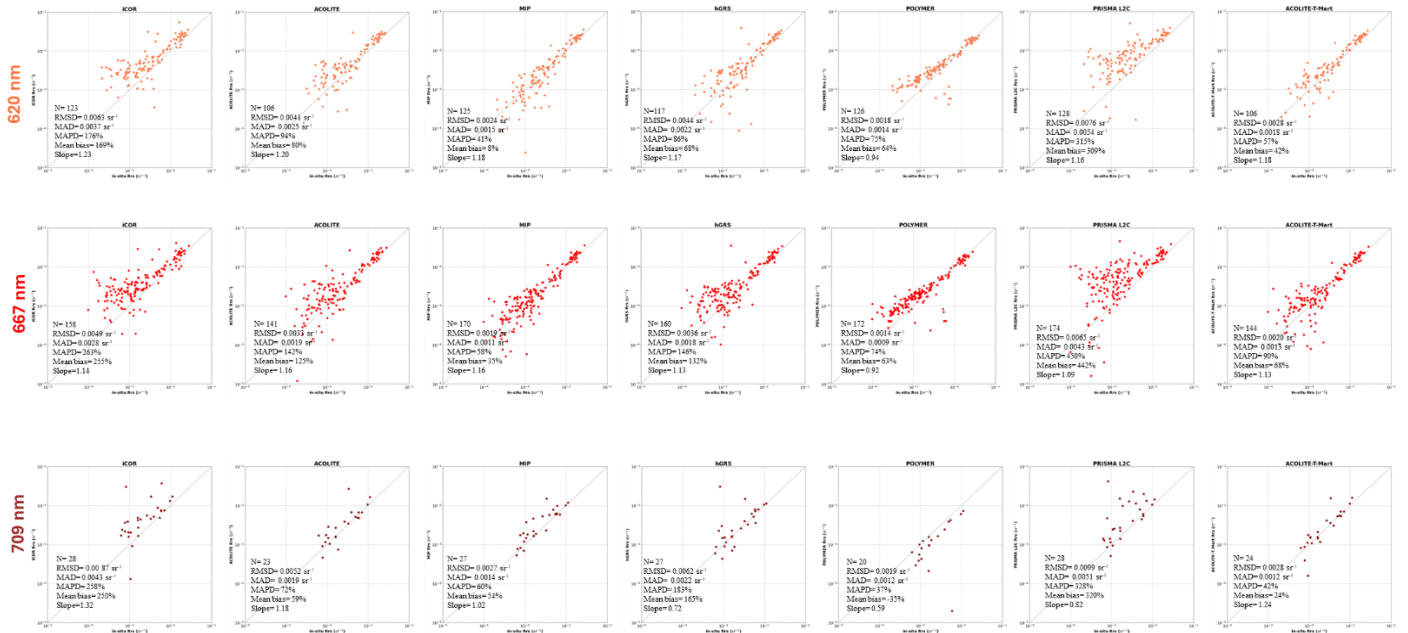


Figure 10 Overall performance of AC processors using the AERONET-OC match-ups with all the satellite data combined. The number of matchups per processor and per band is reported in the scatterplots (N) along with the statistics. The black lines refer to the 1:1 line. (Image adapted from [79]).

Figure 11 shows the two statistics MdSA and Bias used previously in the ACIX-Aqua project paper in bar plot format. In general, the noisiest band, where the highest error values were recorded, was b_443, while a lower error was found at b_560 and b_620. Lower values of MdSA and Bias, hence better agreement between the data, were obtained in the case of MIP. Furthermore, for almost all bands MIP showed MdSA values slightly higher than the 30% threshold. Higher uncertainties shown in the case of PRISMA.

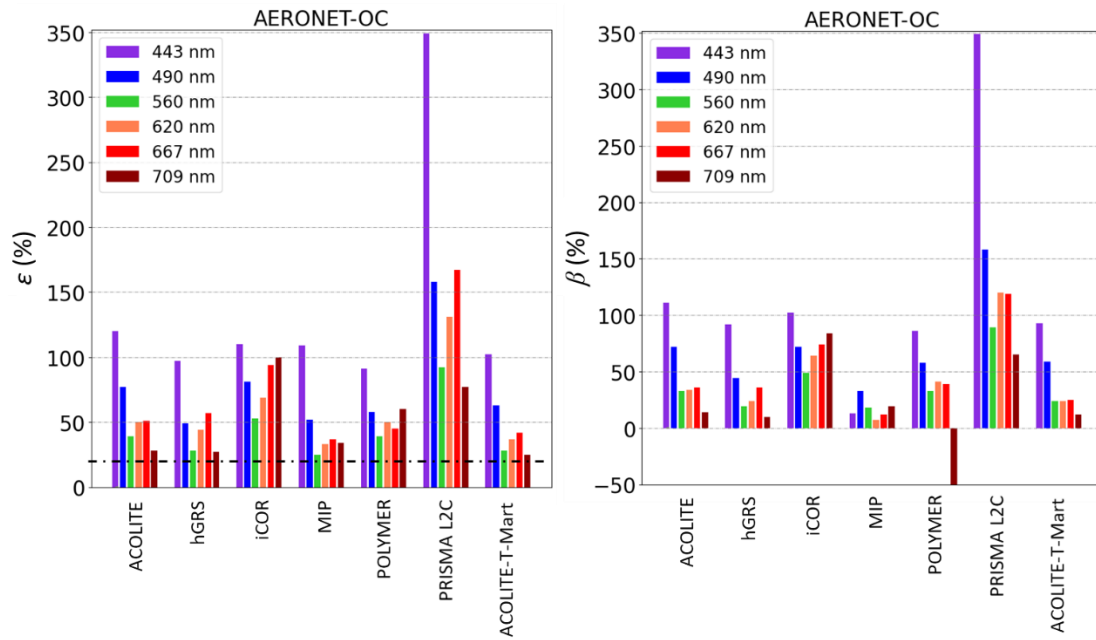


Figure 11 Performance assessments as determined by the Median Symmetric Accuracy (ϵ) and Bias (β) for all the match-ups combined. The dashed line corresponds to a 30% threshold [18]. (Image taken from Figure 4 [79]).

To perform a more robust analysis, the statistical comparison was also carried out by considering samples with equal size: to do this, the records of each model were removed when even one model had negative values or did not provide the output. In this case, POLYMER showed again the lower mean bias, followed by MIP (from b_443 to b_667) and hGRS at b_709. Slightly higher values in the case of ACOLITE-T-Mart and iCOR; while the first one performed particularly well at b_620, b_667 and b_709, iCOR showed better results at b_443 and b_490. Overall, the error values reported in the bar plot (Figure 13) are slightly decreased and MIP has MdSA error values slightly under the 30% threshold.

ACIX-III Aqua report

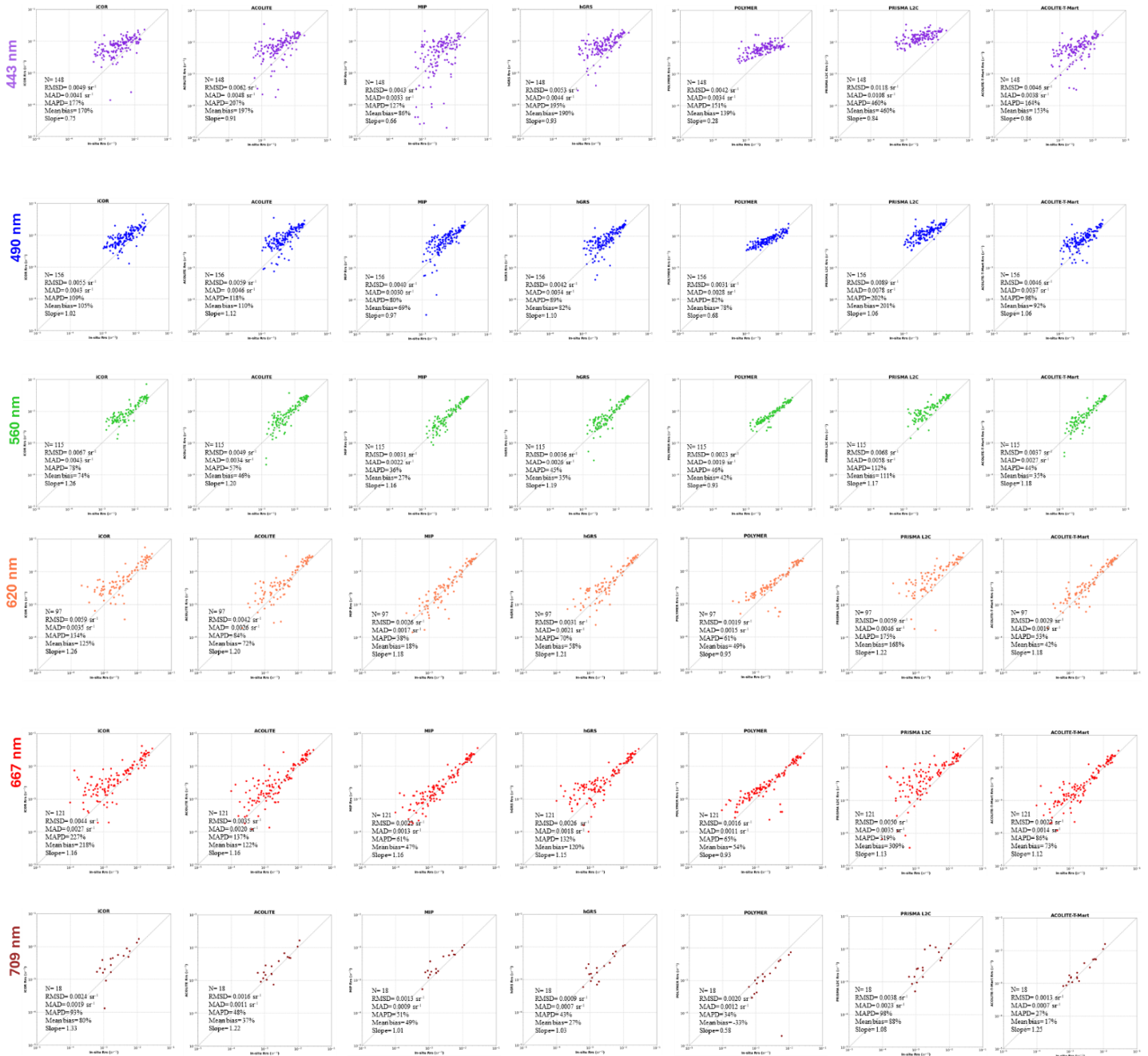


Figure 12 Overall performance of AC processors using the AERONET-OC match-ups with all the satellite data combined (equal size samples). The number of matchups per processor and per band is reported in the scatterplots (N) along with the statistics. The black lines refer to the 1:1 line.

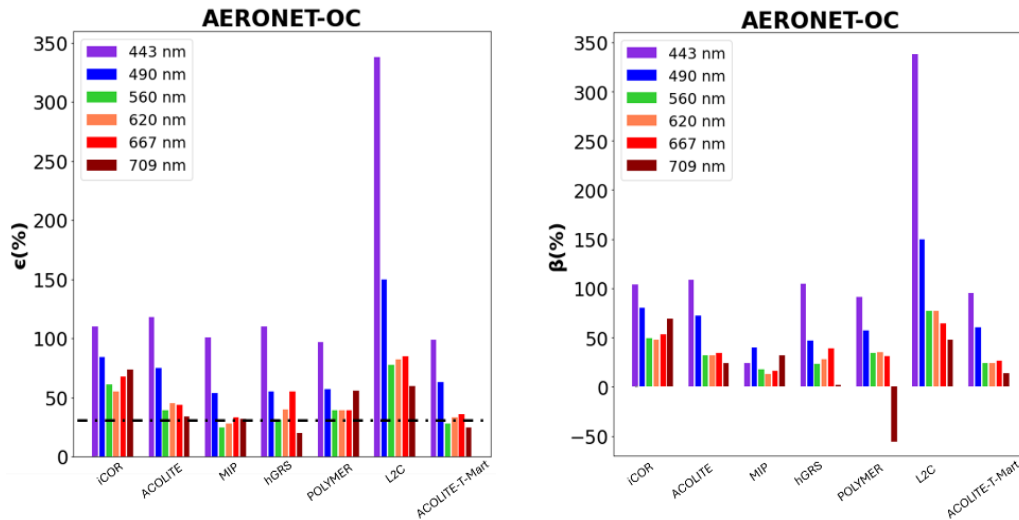


Figure 13 Performance assessments as determined by the Median Symmetric Accuracy (ϵ) and Bias (β) for all the match-ups combined (equal size samples). The dashed line corresponds to a 30% threshold [18].

5.3.2.1 CVD

Figure 14 - Figure 20 show the spectral comparisons between satellite and *in situ* data for the seven CVD sites. The selected study areas are four lakes (three in Italy and one in Switzerland), Venice (lagoon and AAOT), and Rio de La Plata (Argentina). The study areas have significant optical and morphometric differences; for all of them, *in situ* radiometric data were available for calibration and validation purposes. For Lake Garda the analysis has been performed differentiating between optically deep and shallow waters (2 m average depth, close to Sirmione peninsula). A brief characterisation of the sites follows:

- Lake Garda (oligo-mesotrophic): is a deep subalpine glacial lake, where the R_{rs} spectrum is around 0.007 sr^{-1} with a small standard deviation; instead, in the shallow waters the R_{rs} spectrum is about double (peak around 550 nm) and has a larger standard deviation.
- Lake Geneve (oligo-mesotrophic): is a deep subalpine glacial lake, the R_{rs} spectrum is around 0.006 sr^{-1} with a standard deviation of about 0.004 sr^{-1} .
- Rio de la Plata (eutrophic): is a basin estuary with a typical spectral signature of brown water, the R_{rs} peak is about 0.030 sr^{-1} (around 600 nm).
- Lake Trasimeno (meso-eutrophic): is a shallow tectonic lake, with the R_{rs} peak around 0.0025 sr^{-1} in the green region, absorption and reflectance peaks (around 670-700 nm) related to the presence of Chl-a are noticeable from the spectral signature.
- Lake Varese (meso-eutrophic): is a shallow glacial lake, presenting a spectral signature similar to Lake Trasimeno with slightly lower R_{rs} peak values.
- Venice (AAOT) (oligo-mesotrophic): is a transitional region between open sea and coastal waters, the R_{rs} peak is about 0.007 sr^{-1} (around 500 nm), the spectral signature tends roughly to zero after the reflectance peak.
- Venice Lagoon (meso-eutrophic): is a shallow coastal environment, the R_{rs} peak is about 0.020 sr^{-1} , with high standard deviation (about 0.010 sr^{-1}).

Overall, Lake Garda (deep), Lake Geneva and Venice (AAOT) show R_{rs} spectra highest in the blue region and generally decreasing after around 550 nm, representing the typical shape spectra of clear water sites. Lake Trasimeno, Lake Varese, and Venice Lagoon on the other hand, showed the typical spectral shape of turbid waters, with peak reflectance in the green region (around 570 nm) and a secondary peak around 700 nm (associated with the presence of phytoplankton).

PRISMA L2C

The graphs show variable agreement between the satellite spectra (PRISMA L2C) and the *in situ* spectra of each site in terms of the shape of the spectral signature and its magnitude, depending on the water conditions and relative optical complexity. The R_{rs} PRISMA L2C spectra range from peaks slightly lower than 0.015 sr^{-1} to maxima of around 0.040 sr^{-1} in the green region. Generally, in all cases, an overestimation of the R_{rs} PRISMA L2C spectra compared to the *in situ* data can be observed, particularly for Lake Garda (deep waters), Lake Geneva and Venice; better agreement between satellite data and *in situ* data was shown in waters with higher eutrophic load. The highest agreement was indeed reached by Lake Trasimeno ($SA=7.67^\circ$), followed by Rio de La Plata ($SA=7.9^\circ$), and Venice Lagoon ($SA=12.9^\circ$), due to their water optical characteristics, where PRISMA L2C has been able to retrieve the information in the green region (around 570 nm) and at around 700 nm, associated with the presence of phytoplankton and suspended sediments. High standard deviation, quite consistent with the values of *in situ* data, was found for Lake Garda (deep), Lake Trasimeno and Venice Lagoon. In all the study areas the agreement decreased in the blue region, such as in Venice where there were 0.0020 sr^{-1} of difference from *in situ* data.

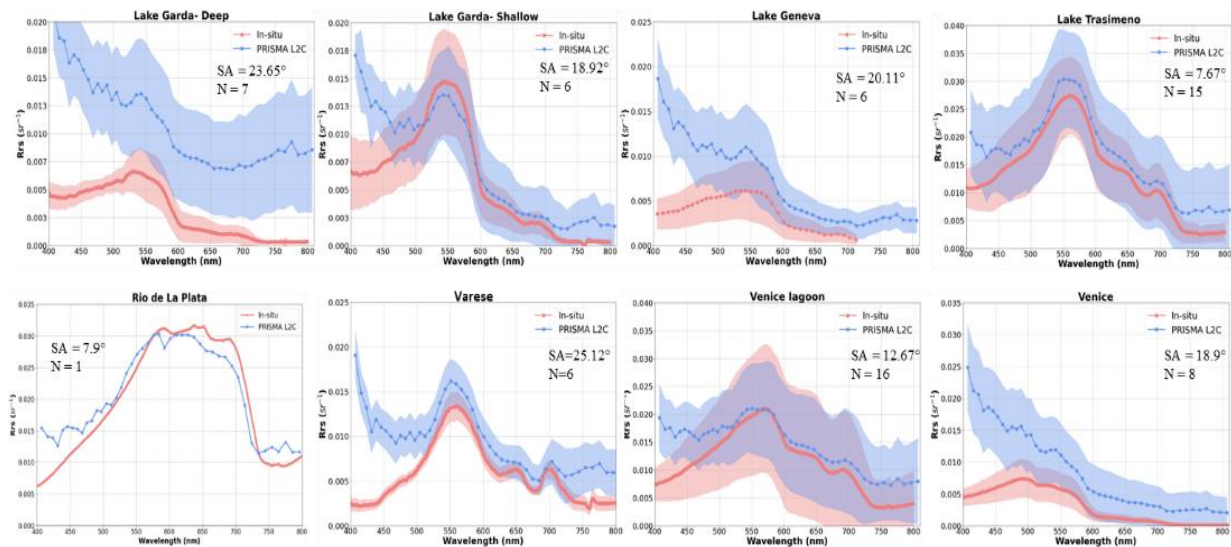


Figure 14 Spectral comparisons between PRISMA L2C and hyperspectral *in situ* data in the 8 sites of the CVD. The variability across the dataset in the mean spectra of PRISMA L2C is displayed as blue curves, with the shaded blue area representing the standard deviation. The mean and standard deviation of the *in situ* data are equivalently shown in orange. SA represents the Spectral Angle and N represents the number of the images.

ACOLITE

The Rrs spectra derived from ACOLITE model range from peaks slightly lower than 0.015 sr^{-1} to maxima of around 0.030 sr^{-1} in the green region. A good agreement can be observed between *in situ* and satellite data especially in waters with high eutrophic load; SA inferior to 20° have been registered in the 88% of the study areas. The highest agreement was indeed reached by Lake Trasimeno (SA= 3.55°), followed by Rio de La Plata (SA= 6.9°), and Venice Lagoon (SA= 9.98°). High standard deviation was found particularly for Lake Geneva, Venice Lagoon and Lake Trasimeno (here the standard deviation of satellite data is in accordance with *in situ* data). In all the study areas the agreement decreased in the blue region, such as in Lake Geneva where there were 0.0011 sr^{-1} of difference from *in situ* data.

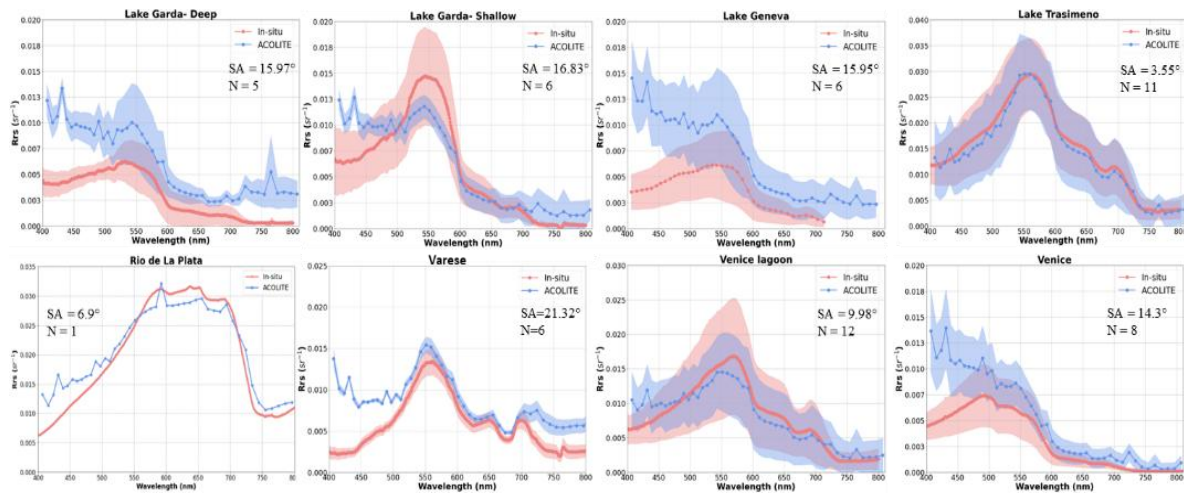


Figure 15 Spectral comparisons between ACOLITE and hyperspectral *in situ* data in the 8 sites of the CVD. The variability across the dataset in the mean spectra of ACOLITE is displayed as blue curves, with the shaded blue area representing the standard deviation. The mean and standard deviation of the *in situ* data are equivalently shown in orange. SA represents the Spectral Angle and N represents the number of the images.

hGRS

Here, the products obtained by applying hGRS model to satellite data; the Rrs spectra generally seemed to underestimate the *in situ* Rrs, for all the sites, with the exception of Lake Geneva and Venice. SA was lower than 20° for the 75% of the study areas, while for Lake Garda (deep) and Lake Varese SA were 60.96° and 34.87° respectively. There is high concordance in the NIR region (no reflectance anomalies), and some difference with *in situ* data in the blue region. The highest agreement was reached in Rio de La Plata (SA= 3.2°), followed by Venice Lagoon (SA= 6.36°), and Lake Trasimeno (SA= 10.49°); the last two CVD presented showed high standard deviation, together with Lake Geneva.

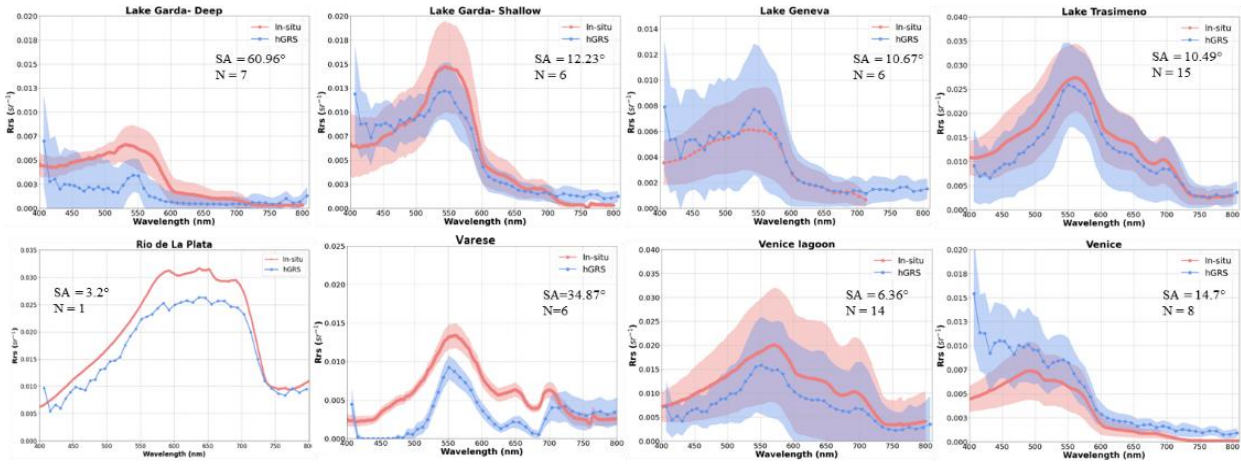


Figure 16 Spectral comparisons between hGRS and hyperspectral in situ data in the 8 sites of the CVD. The variability across the dataset in the mean spectra of hGRS is displayed as blue curves, with the shaded blue area representing the standard deviation. The mean and standard deviation of the in situ data are equivalently shown in orange. SA represents the Spectral Angle and N represents the number of the images.

POLYMER

The Rrs spectra derived from the correction with POLYMER showed a good agreement for all the study areas with *in situ* data; SA was less than 20° in each CVD, with the exception of Lake Varese (SA=22.7°). The highest agreement was reached in Lake Trasimeno (SA=4.22°), followed by Rio de La Plata (SA=6.5°), and Lake Geneva (SA=7.52°). A high concordance was reached also in water with oligotrophic conditions, such as Lake Garda (deep waters). Lake Geneva, although the good performance, showed high standard deviation, and a difference from *in situ* data of about 0.0011 sr⁻¹ in the blue region.

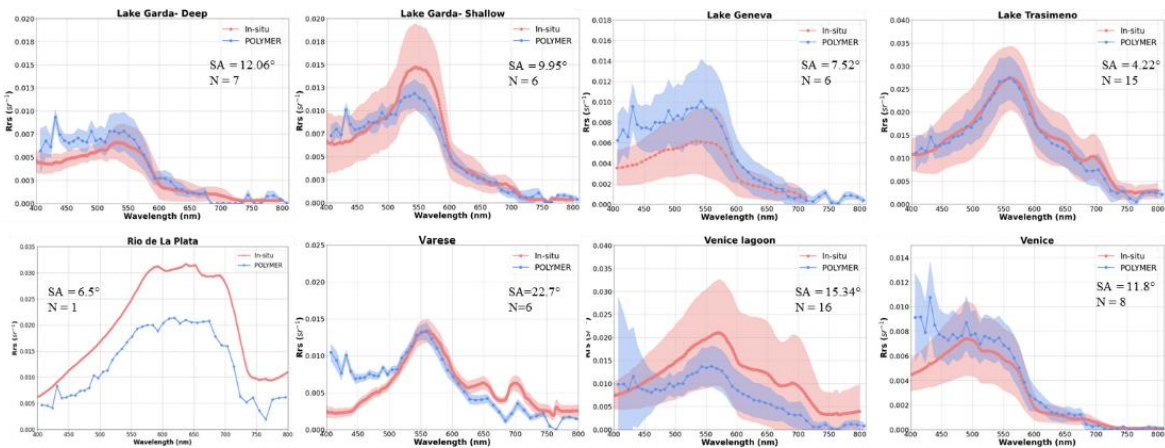


Figure 17 Spectral comparisons between POLYMER and hyperspectral in situ data in the 8 sites of the CVD. The variability across the dataset in the mean spectra of POLYMER is displayed as blue curves, with the shaded blue area representing the standard deviation. The mean and standard deviation of the in situ data are equivalently shown in orange. SA represents the Spectral Angle and N represents the number of the images.

iCOR

The Rrs spectra derived from the correction with iCOR showed a good agreement for all the study areas with *in situ* data, with SA always lower than 20°. The highest agreement was reached in Lake Trasimeno (SA=3.54°), followed by Rio de La Plata (SA=5.3°), and Venice Lagoon (SA=5.35°). A good concordance was reached also in water with oligotrophic conditions, such as Lake Garda (deep waters), although an anomalous peak was registered around 720 nm (0.0065 sr⁻¹). Lake Geneva, Lake Trasimeno, Venice Lagoon and Venice showed high standard deviation (0.010 sr⁻¹).

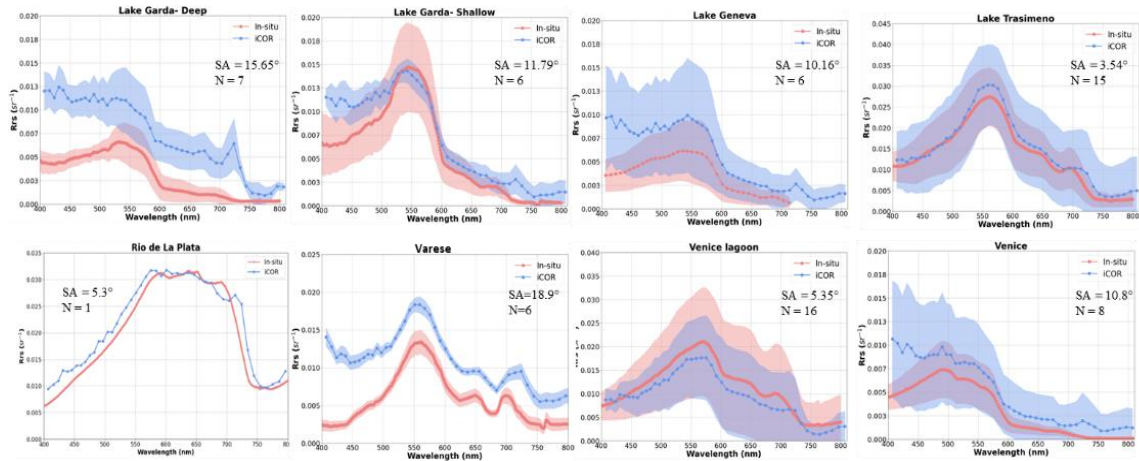


Figure 18 Spectral comparisons between iCOR and hyperspectral *in situ* data in the 8 sites of the CVD. The variability across the dataset in the mean spectra of iCOR is displayed as blue curves, with the shaded blue area representing the standard deviation. The mean and standard deviation of the *in situ* data are equivalently shown in orange. SA represents the Spectral Angle and N represents the number of the images.

MIP

The Rrs spectra derived from the correction with MIP showed a good agreement for all the study areas with *in situ* data (SA lower than 20° for the 88% of the study areas), particularly in the blue region, although this area, together with the NIR spectral region presented some spikes. The highest agreement was reached in Lake Trasimeno (SA=4.98°), followed by Venice Lagoon (SA=6.48°), and Lake Garda (shallow waters, SA=7.85°). An underestimation of Rrs was registered in Lake Garda (both deep and shallow waters), and in Venice Lagoon; both sites presented reflectance peaks in the NIR region (0.005 sr⁻¹). Lake Geneva showed high standard deviation (± 0.010 sr⁻¹).

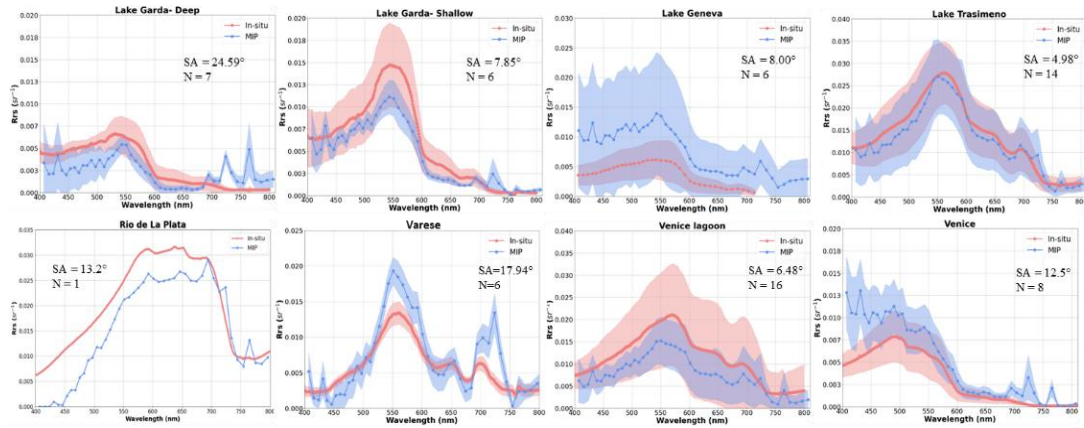


Figure 19 Spectral comparisons between MIP and hyperspectral in situ data in the 8 sites of the CVD. The variability across the dataset in the mean spectra of MIP is displayed as blue curves, with the shaded blue area representing the standard deviation. The mean and standard deviation of the in situ data are equivalently shown in orange. SA represents the Spectral Angle and N represents the number of the images.

ACOLITE-T-Mart

The results obtained applying ACOLITE-T-Mart were quite similar to the one obtained with ACOLITE, with an improvement for the small lakes or the sites close to the coast, due to the adjacency effect correction. The enhancement was in fact notable in Lake Varese, a small lake, where SA decreased of about 15% (from 21.32° to 18.02°) and in Lake Geneva (from 15.95° to 13.02°, with a 18% improvement).

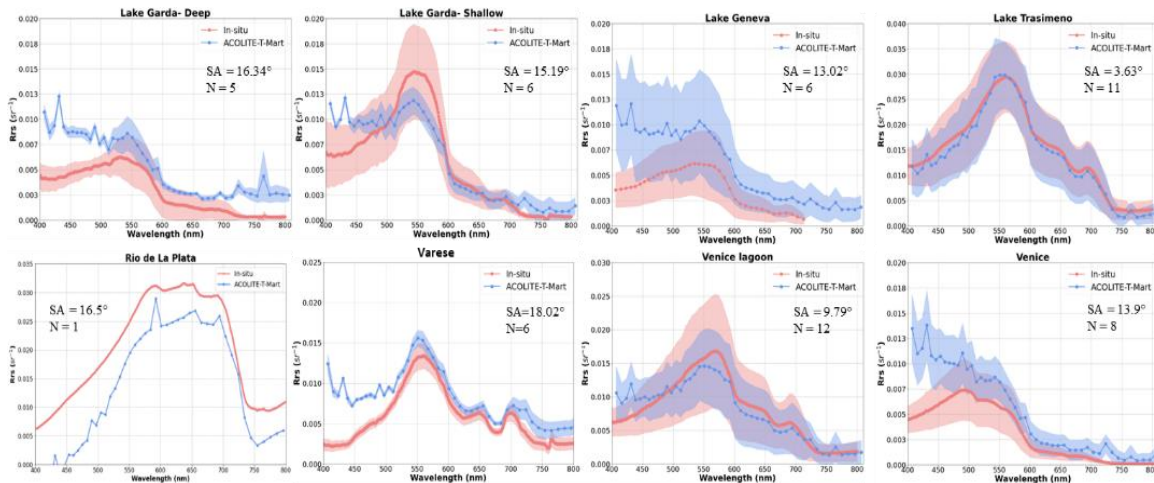
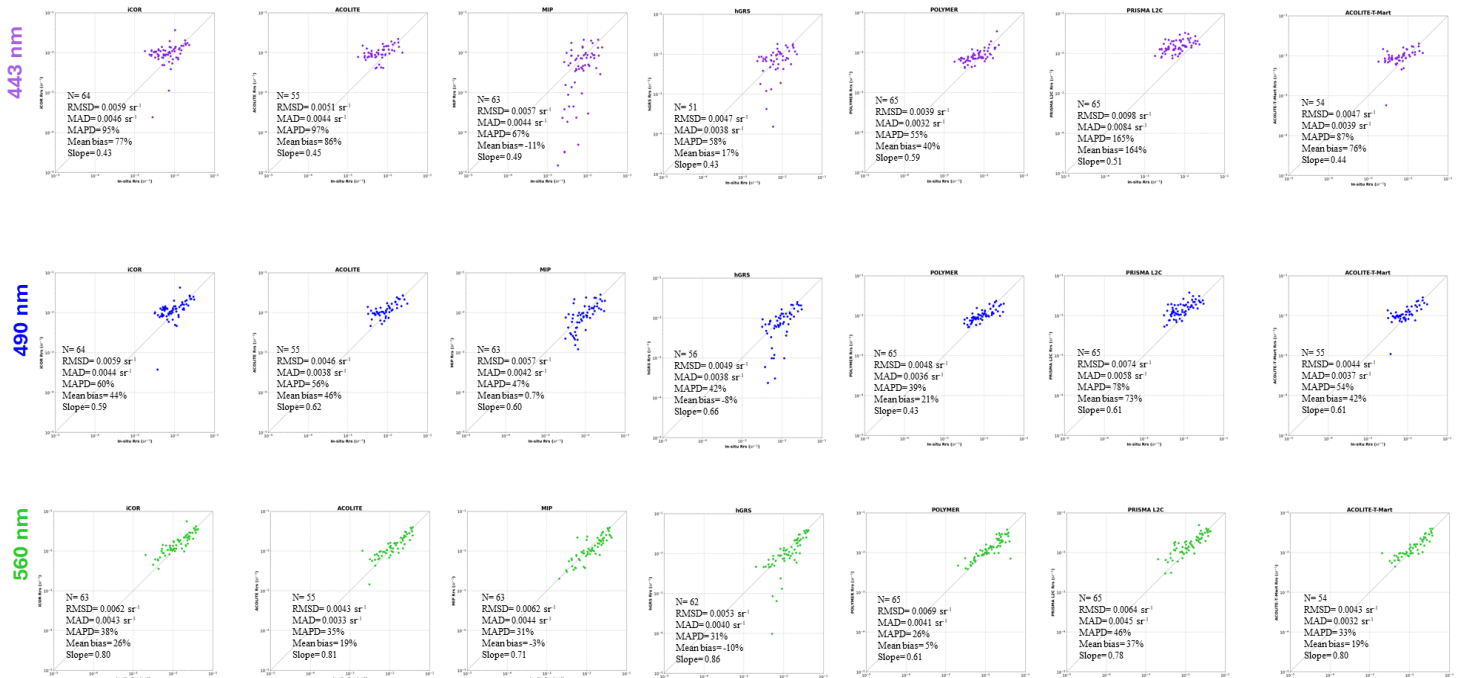


Figure 20 Spectral comparisons between ACOLITE-T-Mart and hyperspectral in situ data in the 8 sites of the CVD. The variability across the dataset in the mean spectra of ACOLITE-T-Mart is displayed as blue curves, with the shaded blue area representing the standard deviation. The mean and standard deviation of the in situ data are equivalently shown in orange. SA represents the Spectral Angle and N represents the number of the images.

Similarly to the previous analysis performed with AERONET-OC data, after performing the spectral comparison, satellite and *in situ* data from all 8 sites were aggregated by AC model and resampled to

the same 6 significant bands. Figure 21 shows the scatterplots in the selected bands together with the sample size value (N) and statistics (RMSD, MAD, MAPD, Mean bias, Slope). As highlighted in AERONET-OC, more dispersion was noted in the blue region, mainly at b_443 (RMSD range: 0.0039-0.0098 sr⁻¹) and at b_490 (RMSD range: 0.0044-0.0074 sr⁻¹). Good fitting for b_560 (RMSD ranged 0.0043-0.0069 sr⁻¹), where the mean MAPD across the 7 AC models changed from 89% to 34%. Slight dispersion in the case of b_620 (RMSD ranged 0.0026-0.0064 sr⁻¹) and b_667 (RMSD ranged 0.0020-0.0052 sr⁻¹). For all the bands, POLYMER showed good fitting with *in situ* data (reaching values of MAPD of 26% at b_560), particularly for wavelengths greater than b_490, while at b_443 the method with the lowest values of MAPD (58%) is hGRS. MIP reached the lowest values at b_620, b_667, and b_709, and ACOLITE-T-Mart at b_560 nm (MAPD=33%). ACOLITE is giving good results too, especially at b_560 (MAPD=35%). Figure 22 shows the two statistics MdSA and Bias used previously in the ACIX-Aqua project in bar plot format. Also, in this subset of the dataset (CVD) the sample size (N) changes at different wavelengths and depending on the processor, for the same reasons explained before.



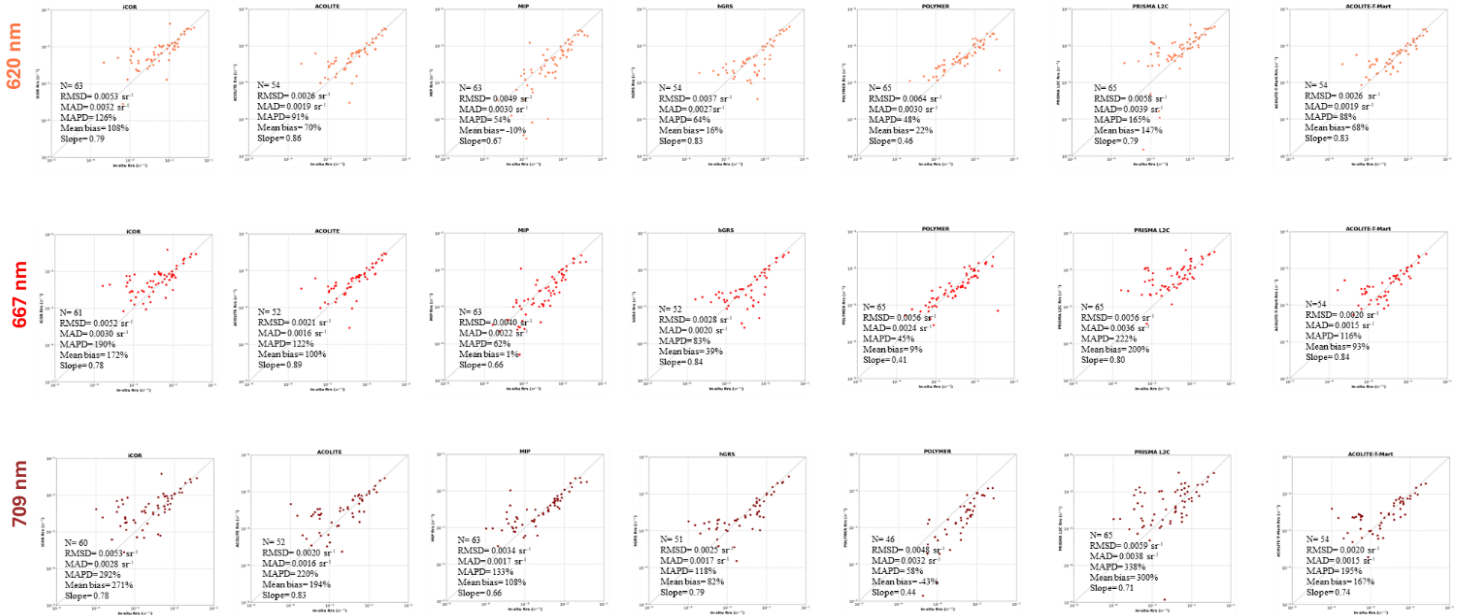


Figure 21 Overall performance of AC processors using the CVD match-ups with all the satellite data combined. The number of matchups per processor and per band is reported in the scatterplots (N) along with the statistics. The black lines refer to the 1:1 line. (Image adapted from [79])

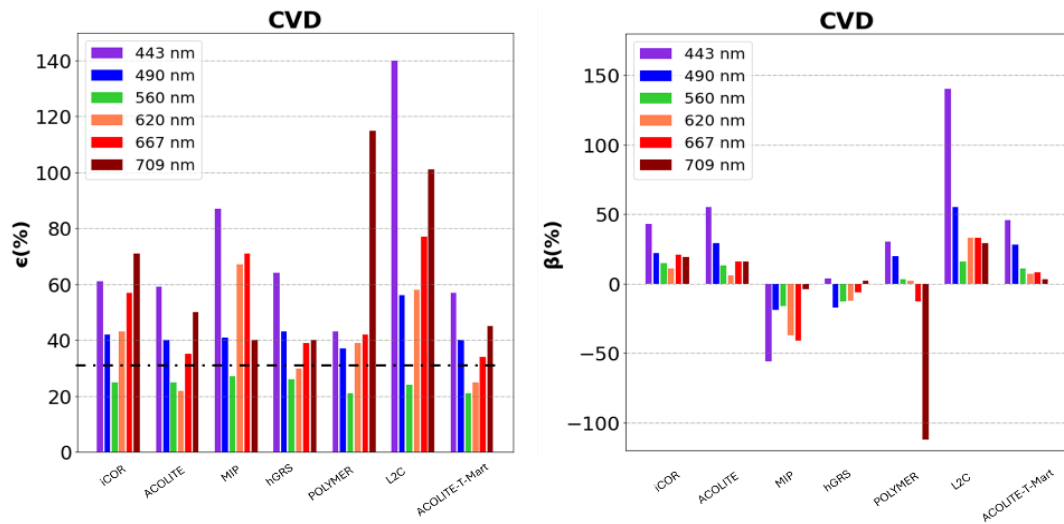


Figure 22 Performance assessments as determined by the Median Symmetric Accuracy (ϵ) and Bias (β) for all the match-ups combined. The dashed line corresponds to a 30% threshold⁵.

The statistical comparison was repeated with the same modalities considering samples with equal size, as did for AERONET-OC. The results can be found in Figure 23 and Figure 24. As in the previous analysis, POLYMER showed the lowest MAPD values in all the bands, except for b_709 where MIP (MAPD=37%) and hGRS (MAPD=42%) agreed more with *in situ* data. MIP is performing well also at b_620 and b_667 (MAPD=38%), while hGRS at b_443 and b_490 (MAPD=59% and 42% respectively).

⁵ <https://gcos.wmo.int/en/essential-climate-variables/lakes/ecv-requirements>

ACIX-III Aqua report

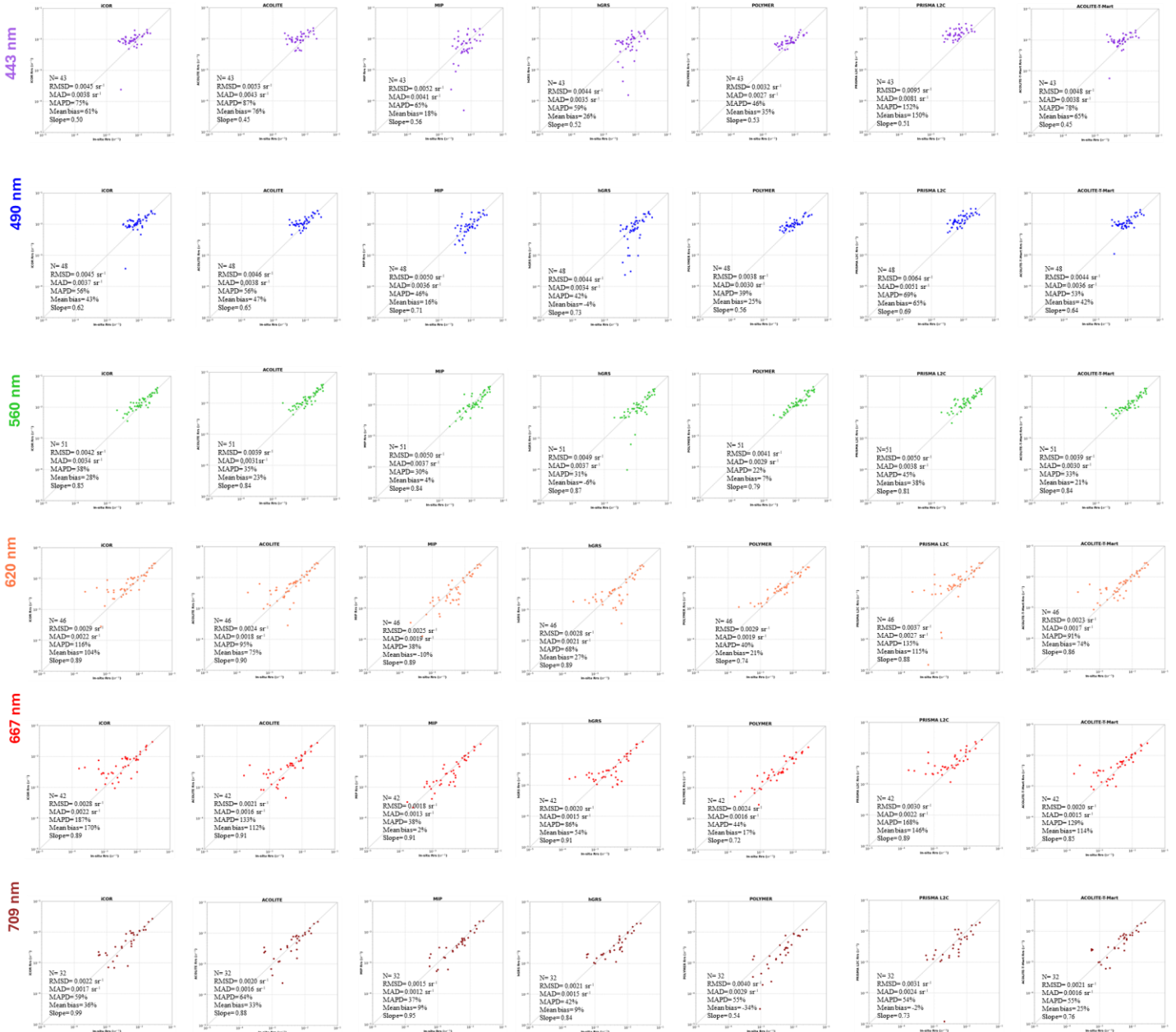


Figure 23 Overall performance of AC processors using the CVD match-ups with all the satellite data combined (equal size samples). The number of matchups per processor and per band is reported in the scatterplots (N) along with the statistics. The black lines refer to the 1:1 line.

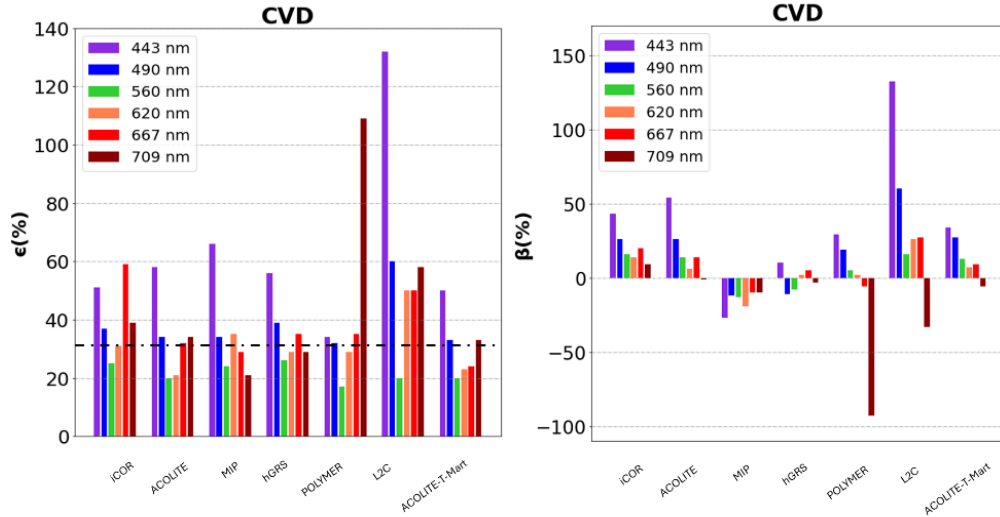


Figure 24 Performance assessments as determined by the Median Symmetric Accuracy (ϵ) and Bias (β) for all the match-ups combined (equal size samples). The dashed line corresponds to a 30% threshold [18].

Deploying hyperspectral data, which provides a wider range of bands, a more detailed analysis was carried out considering the entire spectrum (Figure 25). Concerning all AC methods, higher errors occurred in the blue and red spectral regions, as previously demonstrated for both PRISMA (Pellegrino et al., 2023) and EnMAP [22]. PRISMA L2C has higher ϵ and β values than the other AC methods; POLYMER provides lower ϵ values in the blue band, while hGRS provides lower ϵ values in the red-NIR bands.

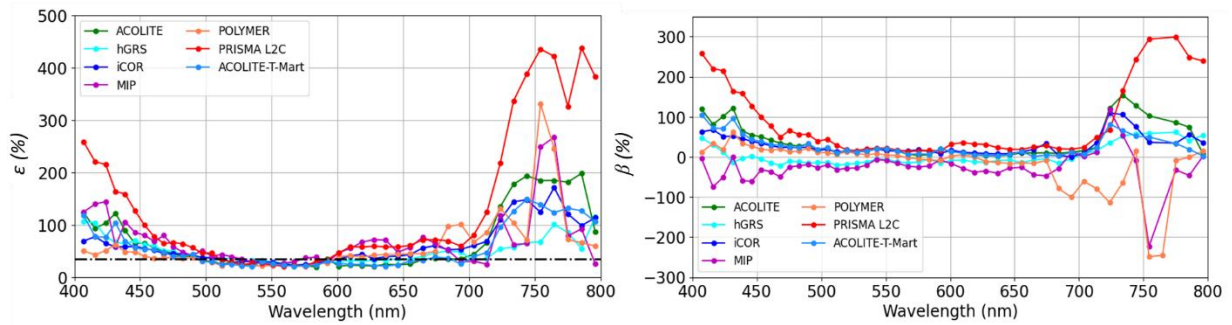


Figure 25 Performance assessments as determined by the spectral Median Symmetric Accuracy (ϵ) and Bias (β) for the AC methods. The dashed-dotted line corresponds to the 30% accuracy threshold suggested by GCOS and adopted also by ACIX-Aqua [18]. (Image taken from Figure 6 [79]).

5.3.3 OPTICAL WATER TYPES

The pairwise intercomparison strategy of in situ Rrs resulted in eight OWTs (selected among the 10 proposed by [80]) that were then used to classify the corresponding PRISMA-derived Rrs spectra from the AC methods (Figure 26). In the first OWT classes (OWT 2, 3a and 3b), representing blue waters with increasing loads of suspended and dissolved matters, the number of in situ Rrs spectra to be used in the pairwise intercomparison with PRISMA ranges from 10 for OWT 2 to 57 for OWT 3b. For OWT 2, the spectral shape of PRISMA-derived Rrs values generally conforms to the in situ measurements for all

AC processors except PRISMA L2C. In the case of OWT 3a and 3b PRISMA-derived R_{rs} values exhibit systematic overestimation at wavelengths shorter than 450 nm for all AC methods. The most represented class of in situ R_{rs} was the OWT 4, with a higher predominance of OWT 4b (82 spectra) than OWT 4a (22 spectra). This class is typical of greenish water, with high phytoplankton biomass and with low reflectance at the shortest wavelengths due to absorption by particles and yellow substances. Generally, PRISMA-derived R_{rs} spectra maintain the features of the in situ data collection with some exceptions in the blue bands, mostly from PRISMA L2C. OWT 5 is also representative of green eutrophic water, with substantially higher phytoplankton biomass and a local R_{rs} maximum around 700 nm; this is also captured by PRISMA as corrected with all the AC methods. OWT 6 is instead characteristic of bright water with high detritus concentrations, which has a high reflectance determined by scattering. These waters are also captured by PRISMA, with some exceptions for MIP and ACOLITE-T-Mart, which underestimate the shortest wavelengths. OWT 7, typical for dark water dominated by absorption from high concentration of yellow substances, shows high divergence in spectral shape for PRISMA L2C and POLYMER, while the other AC methods provide spectra more uniform with the in situ spectra.

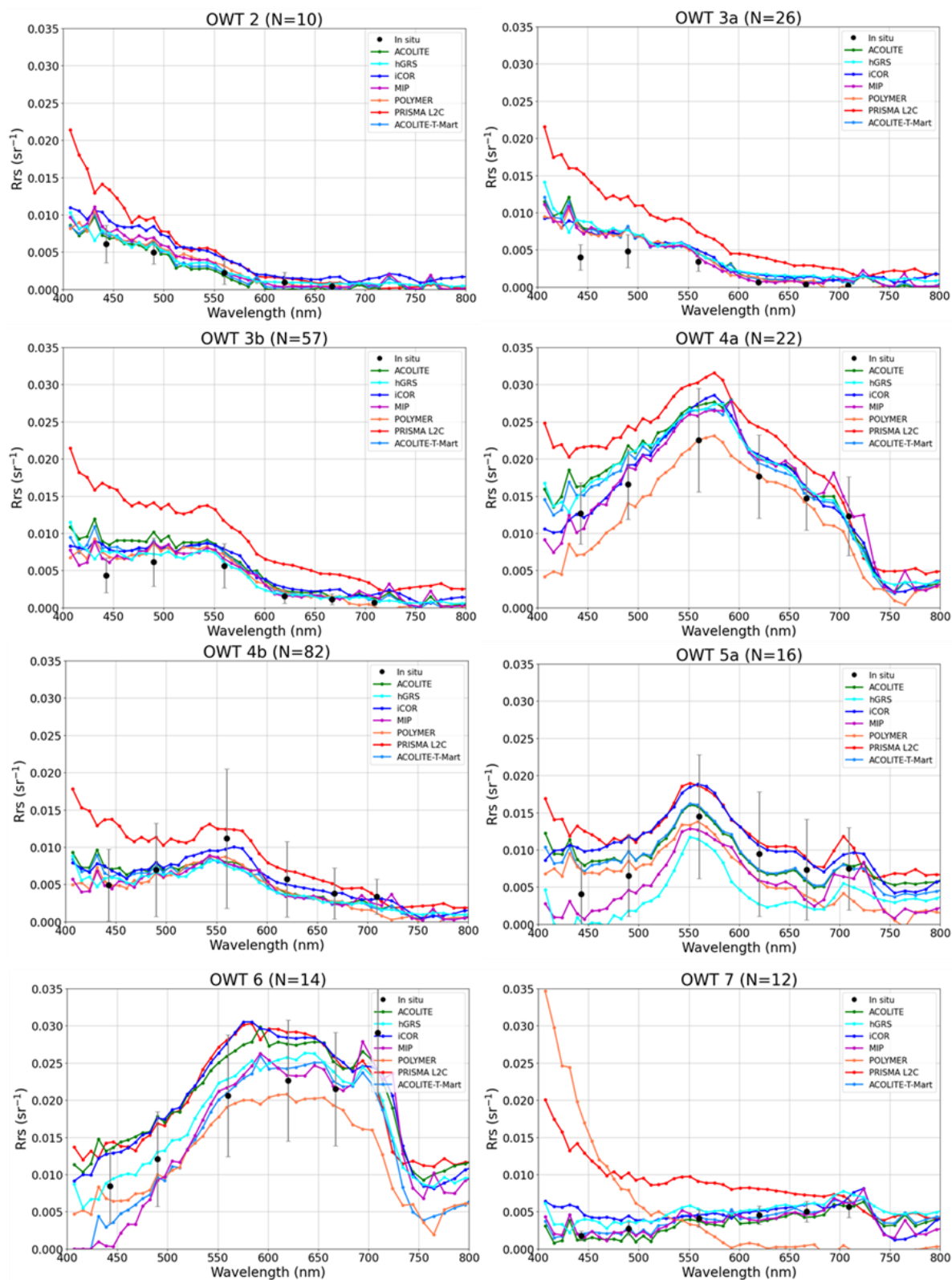


Figure 26 Mean values of PRISMA-derived R_{rs} spectra for each AC method, by OWT. For in situ data, AERONET-OC and CVD have been aggregated and plotted as mean values with standard deviations, from 443 to 667 nm. N provides the number of averaged in situ spectra per OWT. (Image taken from Figure 7 [79]).

OWTs were then used to build heatmaps (Figure 27) to illustrate per band and per OWT performances estimated via win rates, as computed by [18]. The cells of the heatmaps for each AC model have been colored according to the normalized index ($\text{Norm}(\epsilon)$); the AC methods that can generate the highest-quality products for a given OWT and a given band are highlighted with brighter colors. The absolute value of ϵ (%) is also shown in each cell for completeness.

The heatmaps are computed only for the first five of the six pre-defined bands due to the low number of samples in the band at 709 nm. The PRISMA L2C provides the lowest performance across all OWTs and bands, while brighter colors generally emerge for MIP, POLYMER and ACOLITE-T-Mart. A closer inspection of the heatmaps reveals that, depending on both the OWT and the band, each AC method performed differently. For example, at 443 nm, hGRS showed the lowest value of ϵ (33%) for OWT 2, POLYMER for OWTs 3a, 3b, 4b, 5a and 6, iCOR for OWT 4a (22%) and ACOLITE-T-Mart for OWT 7 (9%). The Table 7 provides an overview of the method's performance, based on ϵ , for each OWT in the five significant bands.

ACIX-III Aqua report

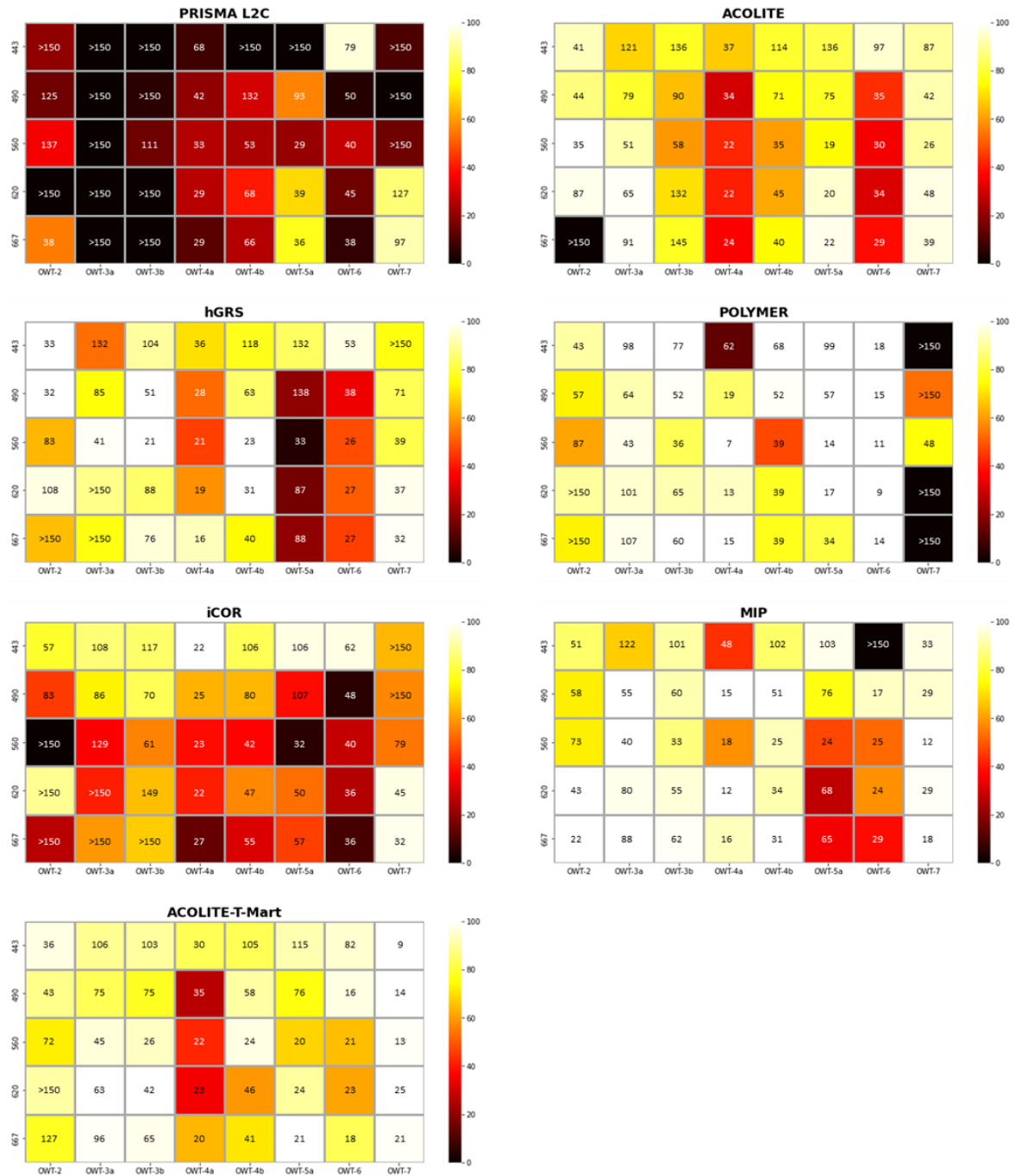


Figure 27 Aggregation of pairwise inter-comparisons (heatmaps) obtained from the MdSA (%) reported in each cell. Processors with lighter colours (white/yellow) are likely to generate high quality for a given OWT and band. (Image taken from Figure 8 [79]).

Table 7 AC models performance by wavelength and OWT (including also the T-Mart model). (Table taken from Figure 8 [79]).

OWT	443 nm	490 nm	560 nm	620 nm	667 nm
2	hGRS	hGRS	ACOLITE	MIP	MIP
3a	POLYMER	MIP	MIP	ACOLITE-T-Mart	MIP
3b	POLYMER	hGRS	hGRS	ACOLITE-T-Mart	POLYMER
4a	iCOR	MIP	POLYMER	MIP	POLYMER
4b	POLYMER	MIP	hGRS	hGRS	MIP
5a	POLYMER	POLYMER	POLYMER	POLYMER	ACOLITE-T-Mart

6	POLYMER	POLYMER	POLYMER	POLYMER	POLYMER
7	ACOLITE-T-Mart	ACOLITE-T-Mart	MIP	ACOLITE-T-Mart	MIP

Additionally, the following Table 8 shows the SA results for each OWT class. The mean SA for each class is considered, N indicates the class size.

Table 8 Average SA results for each OWT class. N indicates the size of each class.

AC Models	2 (N=10)	3a (N=26)	3b (N=57)	4a (N=22)	4b (N=82)	5a (N=16)	6 (N=14)	7 (N=12)
PRISMA	14.3°	19.3°	23.2°	10.0°	26.4°	22.1°	14.4°	34.0°
ACOLITE	31.4°	20.8°	18.9°	7.0°	20.1°	17.4°	21.5°	20.2°
hGRS	9.2°	13.1°	19.6°	6.5°	22.4°	26.9°	11.9°	35.5°
POLYMER	9.3°	12.0°	12.6°	10.3°	13.3°	18.5°	15.2°	74.4°
iCOR	12.6°	14.9°	24.2°	7.3°	17.1°	14.7°	11.7°	18.4°
MIP	10.3°	12.0°	14.9°	10.7°	16.1°	15.4°	18.0°	15.1°
ACOLITE-T-Mart	30.5°	19.2°	19.3°	6.9°	18.1°	15.6°	17.5°	16.6°

5.4 INTERPRETING THE QWIP OUTPUT

The intent of utilising the QWIP in the ACIX-III Aqua was not to quantify the comparative skill of AC approaches, but instead to provide a scene-by-scene conceptualization of spectral reflectance behaviour and a set of diagnostic tools to provide spatial/spectral context to algorithm performance. The QWIP does not provide metrics that convey the absolute accuracy of spectral returns, but it does convey whether the spectral returns are outputting reasonable shapes that resemble typical *in situ* reflectance patterns. A known caveat is that QWIP is largely insensitive to random noise or small residual atmospheric features in the spectra. There may be limitations in regards to the representativeness of the dataset used to develop the QWIP, however, there appears to be an underlying mechanistic rationale for optical properties to behave somewhat reliably (i.e. some relative covariance of absorption and backscatter) in natural waters, which likely explains the consistent tendency for the spectral shape of reflectance to closely follow the NDI (490,665) over a broad range of water types. Nevertheless, false positives and negatives may be present, and the spectral reflectance output should be considered in the interpretation of results. The supporting online materials provide nine figures for each independent scene and AC approach. Figure 28 (A, B, C, D) visually display results of the QWIP analysis, while Figure 29 (A, B, C, D, E) provide output of the extracted spectral reflectance matching a given quality control criteria defined by QWIP scores. Interpretation guidelines, limitations, and caveats of the results and figures are listed below.

Detailed explanations of each plot are given as follows:

- Figure 28 (A) - Map of Apparent Visible Wavelength (AVW). The magnitude of values corresponds to the weighted harmonic mean of the reflectance spectra. Conceptually, this represents the relative balance point of the visible reflectance spectrum. Typically, far red-shifted values (>580 nm) are characterised by high sediment/CDOM or very high biomass and far blue-shifted values (440 –450 nm) represent clear, oligotrophic conditions. Note, the

colour-scale used in Figure 29 that of the AVW image, to help conceptualise where in the image the spectra are coming from.

- Figure 28 (B) - Map of the QWIP score. The Quality Water Index Polynomial itself (Figure 28 (C), black line) represents an empirical relationship between a 2-band Normalised Difference Index (NDI) and the AVW. The difference between a spectrum's NDI and the QWIP equals its QWIP score. Spectra corresponding to lower absolute QWIP scores ($|QWIP| \leq 0.2$) tend to exhibit features that are more closely aligned with *in situ* data (and are coloured in grayscale here) while higher absolute QWIP scores (red/yellow shading; $|QWIP| > 0.2$) are flagged as potentially suspect data. The threshold criteria are based on analysis of *in situ* data, however, these are arbitrary guidelines to aid in conceptualization and should not be considered absolute.
- Figure 28 (C) - This scatter plot displays how each data point in the image compares to the QWIP. Divergent values typically exhibit a proportional reduction in spectral quality. Using a decision tree based on reflectance values, each point is additionally classified as one of three water types [82]. Type I (blue-green), Type II (green), and Type III (brown) waters typically have AVW ranges of 440–530 nm, 500–600 nm, and 540–600 nm, respectively. Spectra are independently flagged if they fall out of a given water type range (see Figure 29 (E)). While not a universal rule, spectra with higher scores ($QWIP > 0.4$; Figure 29 (C)) tend to exhibit more egregious spectral anomalies relative to lower scores ($QWIP < 0.4$; Figure 29 (D)).
- Figure 28 (D) - A histogram showing the frequency distribution of QWIP scores, binned in $|0.1|$ increments. The total number of pixels falling into each bin are also shown. Spectral quality can vary along a continuum of QWIP scores, i.e. exercise caution in designating an absolute pass/fail criteria.
- Figure 29 (A) – The mean normalised spectral shapes corresponding to $|QWIP| \leq 0.2$, as a function of AVW. For example, all spectra meeting the criteria of $550 \text{ nm} < AVW < 551 \text{ nm}$ & $QWIP < |0.2|$ are averaged and displayed as one representative spectra, the spectra is colour-coded as $AVW = 550 \text{ nm}$, and so forth for incremental AVW values ranging from $AVW = 440 - 600 \text{ nm}$. Note, all spectra are normalised by the trapezoidal integration of the area under the reflectance curve prior to averaging. These QWIP criteria tend to yield spectral reflectance shapes that correspond most closely to *in situ* data, relative to higher absolute QWIP scores. This is not always the case, hence the availability of these figures as a qualitative check. These spectra correspond to the grey-scale areas in Figure 28 (B), and the colour coding of the spectra correspond to the AVW map in Figure 28 (A).
- Figure 29 (B) - The mean normalised spectral shapes corresponding to an intermediate range of QWIP scores ($0.2 > |QWIP| > 0.4$), as a function of AVW. Some of these spectra are still in the range of the developmental dataset for QWIP (i.e. they're not all 'bad' spectra), but some obvious processing failures may start to present in this range. These are their own categories representing a mix of 'good' and 'bad' spectra.
- Figure 29 (C) - The mean normalised spectral shapes corresponding to $QWIP > 0.4$, as a function of AVW. While not a unilateral rule, QWIP scores meeting this criterion tend to

capture some evident AC failures. Of all the QWIP output, this particular criterion tends to consistently flag problematic spectra, with few Type II exceptions.

- Figure 29 (D) - The mean normalised spectral shapes corresponding to $QWIP < -0.4$, as a function of AVW. While this criteria will often capture AC failures, sometimes otherwise good-looking spectral shapes may meet this criteria if a large portion of the spectrum contains slightly negative or near-zero values, i.e. be on the lookout for reasonable shapes that were perhaps just overcorrected, usually in the far-blue or far-red portion of the spectrum.
- Figure 29 (E) – The mean normalised spectral shapes corresponding to spectra with an AVW – water type mismatch. According to [19], sometimes a spectrum will have a low QWIP score (indicating better quality), but the water type [82] seems to fall out of range of the expected AVW value. For example, in this instance there were several “green” waters that were shifted much too far towards the blue end of the spectrum compared to what we typically see with *in situ* data. These criteria tend to be robust in terms of flagging suspect spectra.

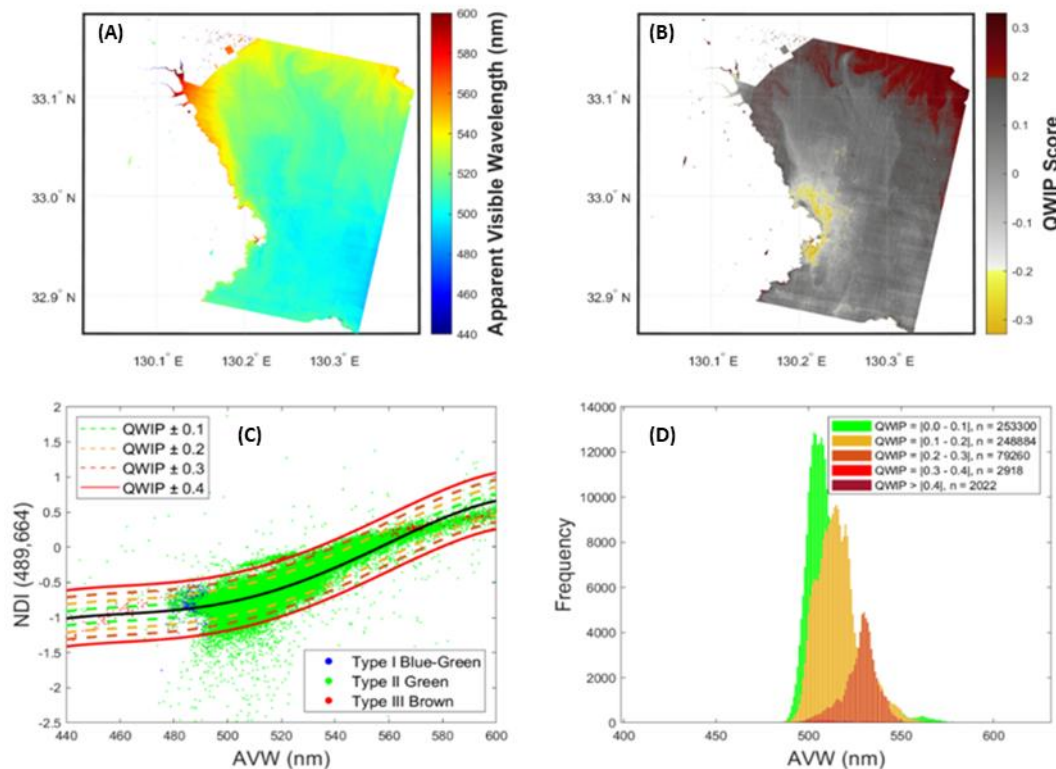


Figure 28 An example of QWIP analysis output for a scene at Ariake Tower AERONET-OC site on May 11, 2020, processed using the hGRS AC approach. (A) Map of AVW, (B) Map of the QWIP score, (C) scatter plot of QWIP analysis, and (D) frequency distribution of incremental QWIP scores.

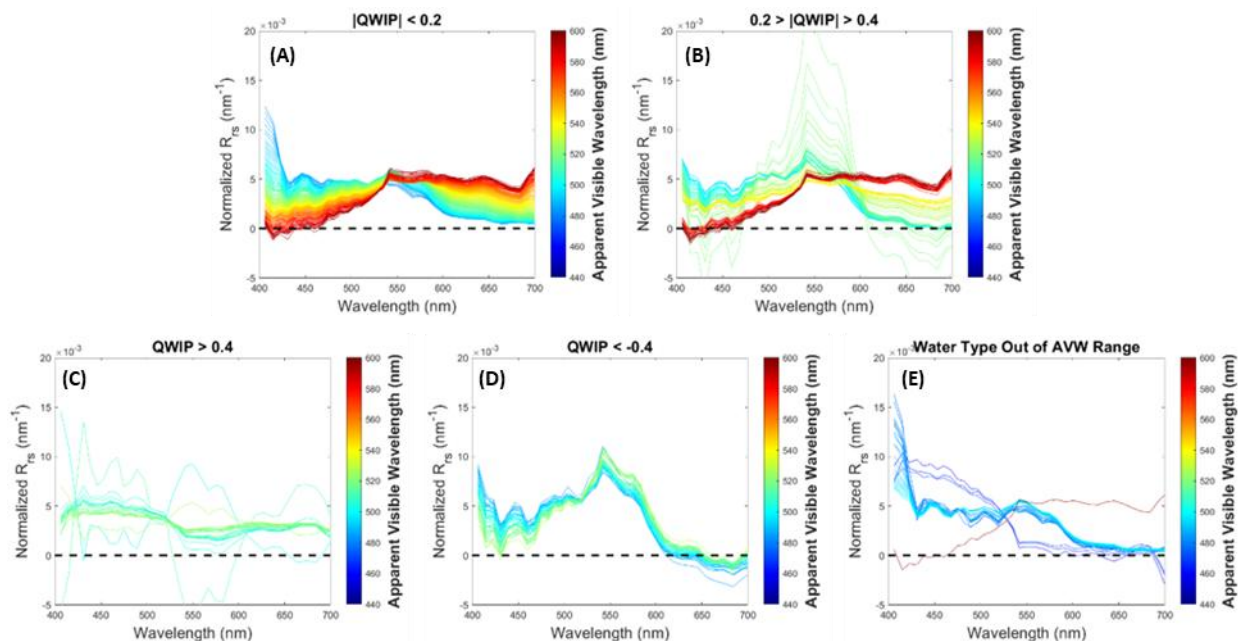
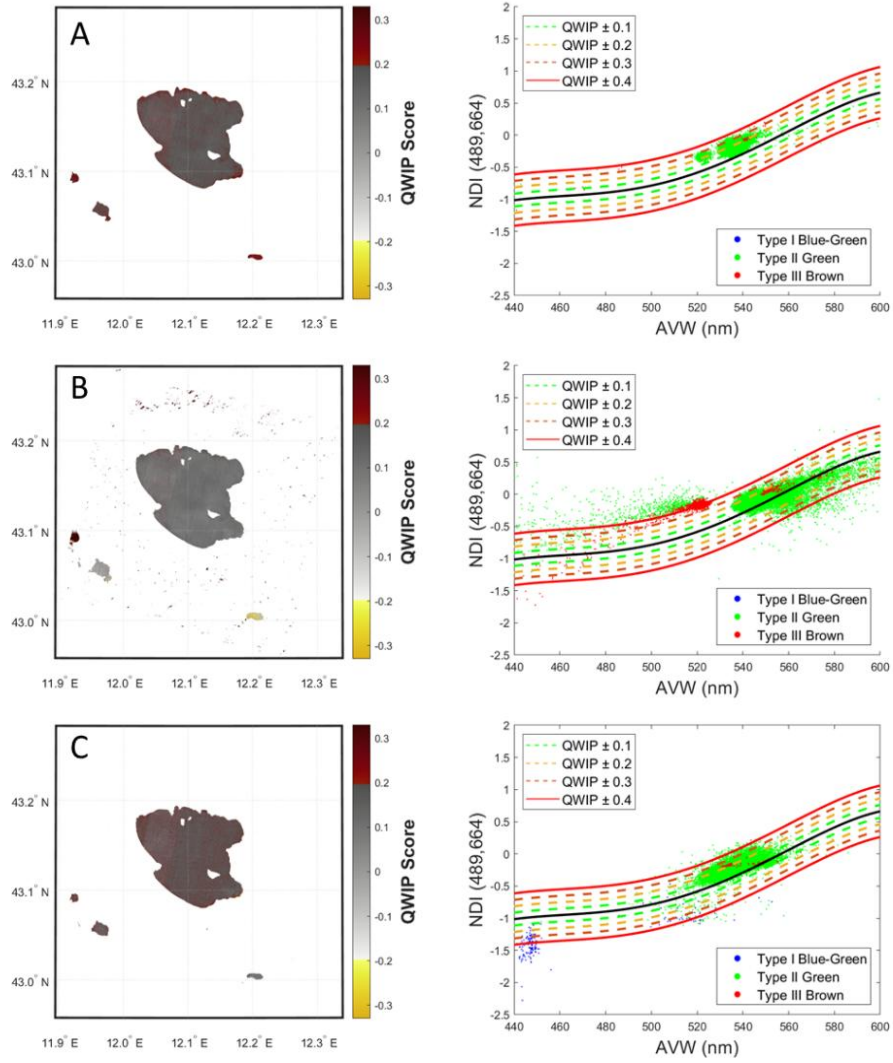


Figure 29 An example of QWIP analysis output for a scene at Ariake Tower AERONET-OC site on May 11, 2020, processed using the hGRS AC approach. These plots display the mean normalised spectral shapes meeting various criteria (A) $|QWIP| < 0.2$, (B) $0.2 > |QWIP| > 0.4$, (C) $QWIP > 0.4$, (D) $QWIP < -0.4$, and (E) out of range water type.

In addition, the example below (Figure 30) shows the results obtained for a Lake Trasimeno scene considering all five AC models and T-mart products (only the Map of the QWIP score and the scatterplots of the QWIP analysis are shown).

ACIX-III Aqua report



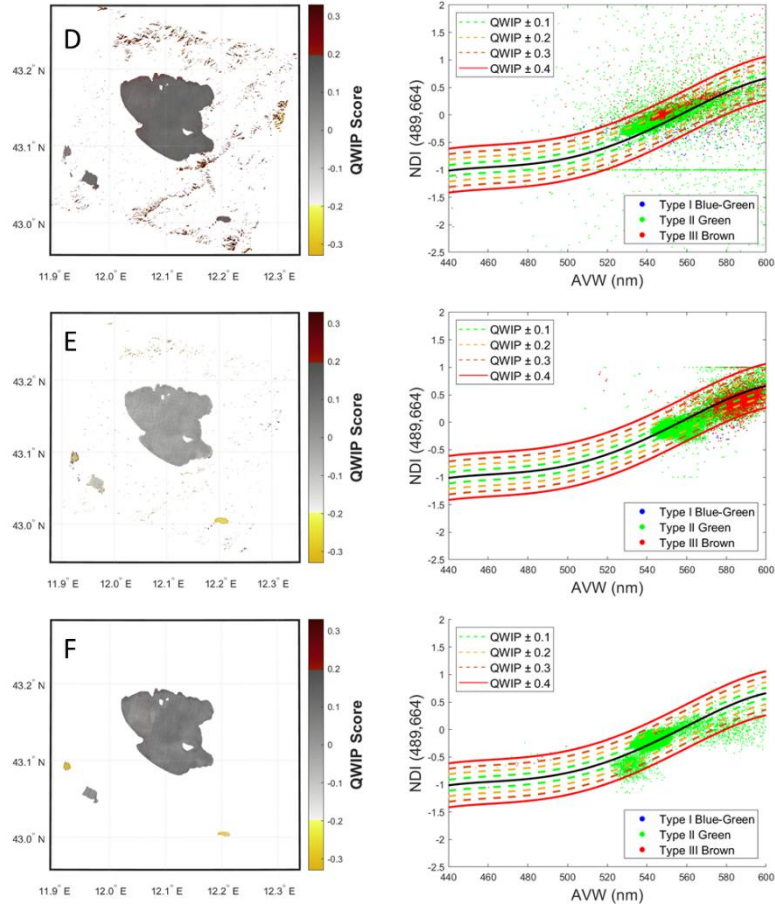


Figure 30 Results obtained for a Lake Trasimeno scene considering all five AC models (A: ACOLITE, B: hGRS, C: POLYMER, D: iCOR, E: MIP) and T-Mart product (F). On the left it is shown the QWIP score map and on the right the scatterplots of the QWIP analysis.

6 EnMAP DATA ANALYSES

6.1 DATASET AND MATCH-UP ANALYSIS

This study is based on [22] which considers matchup data from 2022 to 2023. Meanwhile many more *in situ* matchups to EnMAP acquisitions have been obtained [83]. The data are presented similarly to those provided in Chapter 5 for PRISMA for consistency across the report.

6.2 IN SITU DATA

In order to validate the EnMAP satellite mission data, similar sites and infrastructure were delivering matchup *in situ* data as for the PRISMA assessment (cf. Table 2). The *in situ* dataset contained multi- and hyperspectral (CVD) data from 17 study sites (Figure 31 and Table 9). For these study sites, 50 time-synchronous EnMAP images were generated, including 47 high quality images and four commissioning phase images classified as "low quality" by the ground segment; three at Lucinda Jetty Coastal Observatory (LJCO) and one at Lake Constance. These data were not removed as their uncertainties met the mission requirements defined by the EnMAP ground segment: a root mean square error (RMSE) outside strong atmospheric absorption regions and for aerosol optical thickness (AOT) at 550 nm < 0.04 for $400 \text{ nm} < \lambda \leq 450 \text{ nm}$; < 0.02 for $450 \text{ nm} < \lambda \leq 650 \text{ nm}$; and < 0.01 for $650 \text{ nm} < \lambda \leq 800 \text{ nm}$. For AOT at 550 nm > 0.4 , the corresponding requirement increases by 0.01. This section introduces the *in situ* data used to carry out this work.

Table 9 List of study sites, location, type of *in situ* measurements and number of images (C: Commissioning, O: Operational mission phase, LQ: Low Quality).

Abbreviation	Study Site	Location	<i>In situ</i> Measurement	Number of Images
AAOT	Acqua Alta Oceanographic Tower	43.31°N, 12.51°E	Hyperspectral and AERONET-OC	C: 2, O: 5
BB	Bahia Blanca	39.14°S, 61.72°W	AERONET-OC	C:9
BR	Banana River	28.37°N, 80.63°W	AERONET-OC	O:1
CB	Chesapeake Bay	39.12°N, 76.35°W	AERONET-OC	C:4
GP	Galata Platform	43.04°N, 28.19°E	AERONET-OC	C:1
IL	Irbe Lighthouse	57.75°N, 21.72°E	AERONET-OC	C:1
KO	Kemigawa Offshore	35.61°N, 140.02°E	AERONET-OC	C:1
LC	Lake Constance	47.63°N, 09.37°E and 47.63°N, 09.36°E	Hyperspectral	C: 1 (LQ: 1)
LT	Lake Trasimeno	43.12°N, 12.13°E	Hyperspectral	C:1
LAMP	Lampedusa	35.49°N, 12.47°E	Hyperspectral	O: 1
LJCO	Lucinda Jetty Coastal Observatory	18.52°S, 146.39°E	Hyperspectral and AERONET-OC	C: 5 (LQ: 3), O: 10
MVCO	Martha's Vineyard Coastal Observatory	41.32°N, 70.57°W	AERONET-OC	C:1
OO	Oostende	51.25°N, 02.92°E	Hyperspectral	O:1
SM	San Marco	02.94°S, 40.21°E	AERONET-OC	O:1
S7	Section-7 Platform	44.55°N, 29.45°E	AERONET-OC	C:1
SG	South Greenbay	44.60°N, 87.95°W	AERONET-OC	C:1
SO	Socheongcho	37.42°N, 124.74°E	AERONET-OC	C:3

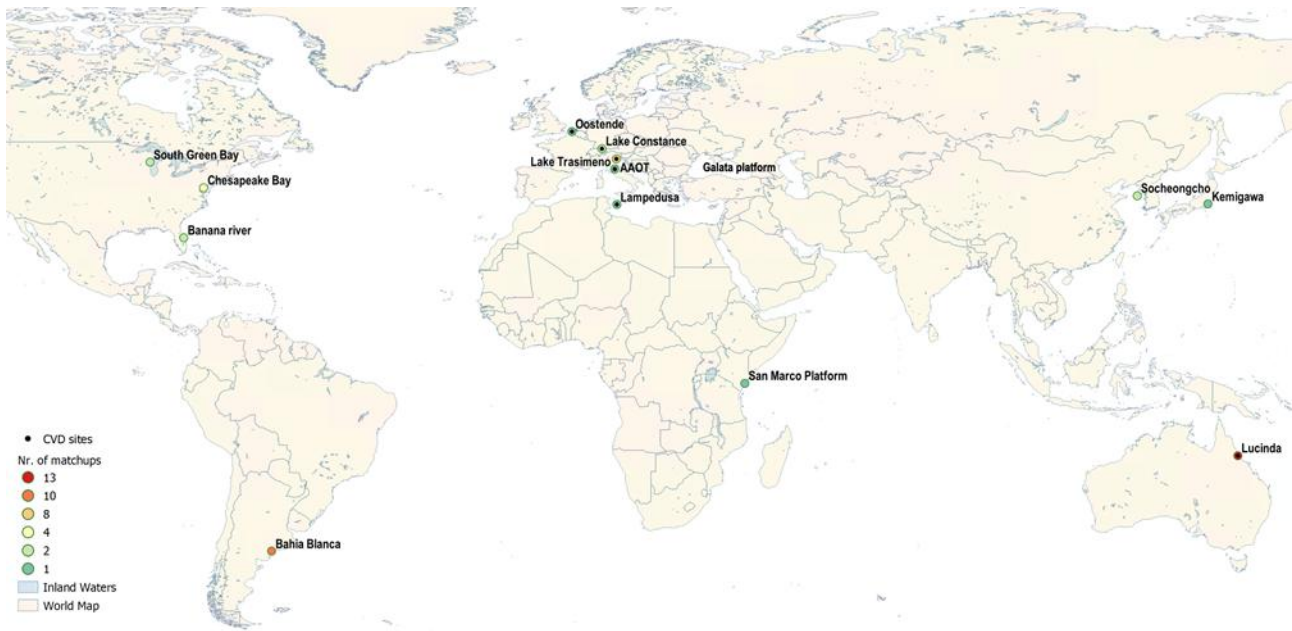


Figure 31 Dataset of the globally distributed sites and number of available match-ups between EnMAP and field data. The colour of the dots indicates the number of available match-ups ranging from a minimum of 1 to a maximum of 13 for every study area. The Location of AERONET-OC are indicated with circles only, the black dots indicate CVD sites. AAOT (Venice) is both Hyperspectral (CVD sites) and AERONET-OC.

Hyperspectral *in situ* measurements were collected with different instruments: PANTHYR (AAOT and Oostende), HYPERNETS (AAOT), Ocean Optics Sensor System (OOSS, Lake Constance), Sea-Bird Hyper-PRO hyperspectral radiometers (Lampedusa), WISPstation (Lake Trasimeno) and Sea-Bird hyperspectral ocean colour radiometers (HyperOCR, LJCO). Details on the measurement systems can be found in: PANTHYR [32], HYPERNETS [84], Sea-Bird Hyper-PRO [27], WISPstation [11,85], and HyperOCR LJCO [86]. Nearly all measurements were collected from above-water radiometry. Data were not corrected for bidirectional effects and provided either as Rrs and converted to water leaving reflectance (ρ_W) by multiplying by π , or directly as ρ_W . For Lampedusa, measurements were collected from in-water radiometry and Rrs was derived at nadir, enabling directly to convert to $[\rho_W]N$ by multiplying by π . To avoid confusion with nomenclature we adopt the term ρ_W for the hyperspectral *in situ* measurements. Following [87,88] all hyperspectral *in situ* measurements were spectrally resampled to the spectral response function as provided in the EnMAP metadata [20].

As for the PRISMA comparison, AERONET-OC measurements are collected by SeaPRISM [30]. AERONET-OC level 1.5 data (real time cloud screened) were used for validation as coincident level 2 data with the EnMAP overpasses were not available. The normalized water leaving radiance data corrected for bidirectional effects based on the IOP approach [89] ($[LW]NIOP$) were converted to normalized water leaving reflectance $[\rho_W]N$ by multiplying by π and dividing by the mean extraterrestrial solar irradiance [90].

6.3 EnMAP DATA

Level 1B, Level 1C, and Level 2A products (processing version V010400) were obtained from the DLR Portal Earth Observation Center for the period spanning June 2022 to December 2023. Briefly, Level 1B data includes radiometric corrections and spectral characterization; Level 1C is derived from the Level 1B product and geometrically corrected (orthorectified) and re-sampled to a specified grid. Level 2A is derived from the L1C product and atmospherically corrected to generate surface reflectances separately for land and water applications. More details on the EnMAP data processing levels can be found on the EnMAP website⁶ and in [20]. The EnMAP Level 2A water product [pW]N is generated by the dedicated water AC MIP developed by EOMAP GmbH (see section 2.3.5, we used processor V01.04.02). Further, we pre-processed EnMAP L1B with Polymer (see section 2.3.3) and EnMAP L1C data with ACOLITE AC (see section 2.3.1) to [pW]N and pW, respectively, to analyze and cross-compare the performances of the processors. The processing of EnMAP data with Polymer (v4.16.1) has been implemented in the publicly available, alternative EnMAP Processing Tool (EnPT⁷, [91]) and its wrapper module ACwater⁸ within the EnMAP-Box QGIS plugin [92]. The EnPT module ACwater contains all needed specifications and the technical framework required to apply the Polymer algorithm to EnMAP. ACOLITE can be obtained at GitHub⁹, and in this study, we used the version 20231023.0 without and with the option of glint correction [24,93]. As mentioned, Polymer is implemented in EnPT which processes EnMAP data from Level 1B to Level 2A, including radiometric, geometric, and AC (using POLYMER for water surfaces) and orthorectification. In contrast, ACOLITE does not perform radiometric and geometric corrections, and thus its input data is Level 1C. For PACO-WASI, the EnMAP Level 2A land product (note, here processor version V01.05.02 was used) was converted to pW by correcting for sun glint, sky glint and path radiance errors using WASI. This correction was performed by experienced users who manually fine-tuned the inverse modelling settings for each individual scene, as described in Section 2.3.6. WASI can be downloaded from [54].

The hyperspectral validation was performed in the 420 – 800 nm spectral range, which is the range covered by all *in situ* measurements; the multispectral validation from 444 to 800 nm. As the ACOLITE results do not include the O2 band around 763 nm, this band was also excluded from the MIP and Polymer retrievals in the AC intercomparison exercise.

6.4 MATCH-UP ANALYSIS

The hyperspectral validation was performed in the 420 – 800 nm spectral range, which is the range covered by all *in situ* measurements; the multispectral validation from 444 to 800 nm. For the multispectral validation we took the closest EnMAP band as provided in Table 10. As uncertainties are not provided for most of the *in situ* data, they are expected to be smaller than the mission requirements. As the ACOLITE results do not include the O2 band around 763 nm, this band was also

⁶ https://www.enmap.org/data_access/

⁷ https://enmap.git-pages.gfzpotssdam.de/GFZ_Tools_EnMAP_BOX/EnPT/doc/about.html

⁸ <https://gitlab.awi.de/phytooptics/acwater>

⁹ <https://github.com/ACOLITE/ACOLITE>

excluded from the MIP and Polymer retrievals in the AC intercomparison exercise. For the relative comparison between the ACs, it can be expected that all processors are affected to a similar extent by the instrument uncertainties [18]. To check for the high temporal variability of the *in situ* measurements close to the EnMAP overpass time, we calculated the mean and standard deviation at the ± 15 minute window when data were available. For three days at LJCO the *in situ* reflectance showed high temporal variability, and we opted to compare EnMAP data to the mean *in situ* reflectance instead of using the closest measurement in time, as for all other *in situ* matchups.

Table 10 Band settings in the different datasets: the nominal band used in the match-up analysis and the corresponding band settings of AERONET-OC and EnMAP. The first part of the table refers to the band setting used for the entire dataset, while the second part refers to the additional bands considered for the CVD dataset only.

	Nominal band	AERONET-OC band setting	EnMAP band setting
AERONET-OC & CVD datasets	443 nm	443 \pm 5 nm	444.7 \pm 3.0 nm
	490 nm	490 \pm 5nm	491.8 \pm 2.9 nm
	560 nm	560 \pm 5 nm	561.1 \pm 3.2 nm
	620 nm	620 \pm 5 nm	622.9 \pm 3.6 nm
	667 nm	667 \pm 5 nm	666.6 \pm 3.8 nm

EnMAP retrievals were compared to the *in situ* measurements following the OLCI match-up protocol [94] and using a 3 x 3-pixel box and a time window of $\pm 01:15$ h. Most of the measurements were available within ± 15 minutes from the overpass (36 out of 50); 17 during the overpass. EnMAP-MIP pixels were excluded from analysis when they were masked as cirrus, cloud, cloud shadow, and haze flags. For Polymer, we found that the default flags did not always accurately correspond to invalid match-ups, so we decided not to apply any flags and investigate this issue further. For ACOLITE we applied the default recommended flags: NIR or SWIR threshold test, CIRRUS threshold test, TOA threshold test, NEGATIVE surface reflectance test and EXTENT test. Most of the pixels of the 3 x 3-pixel box were retained in the end, usually 7 to 9 pixels, for the valid match-ups. The EnMAP spectrum represents the median of the pixel box after the flagged and outlier pixels were removed. The number of valid match-ups of each AC processor for hyper- and multispectral *in situ* data was 22 and 24 for MIP, 21 and 20 for Polymer, 11 and 17 for ACOLITE without and 3 and 8 for ACOLITE with glint correction applied, and 21 and 30 for PACO-WASI, respectively. The frequency distribution of the Rrs levels of the *in situ* matchup data are provided in Figure 32.

As for the PRISMA evaluation, we followed the statistical metrics detailed in section 2.4.3. We also analysed the spectral shape of EnMAP using the spectral angle mapper (SAM, θ°) to determine the similarity between an EnMAP and an *in situ* reference spectrum. . Spectral Angles (SA) were calculated on the mean spectra.

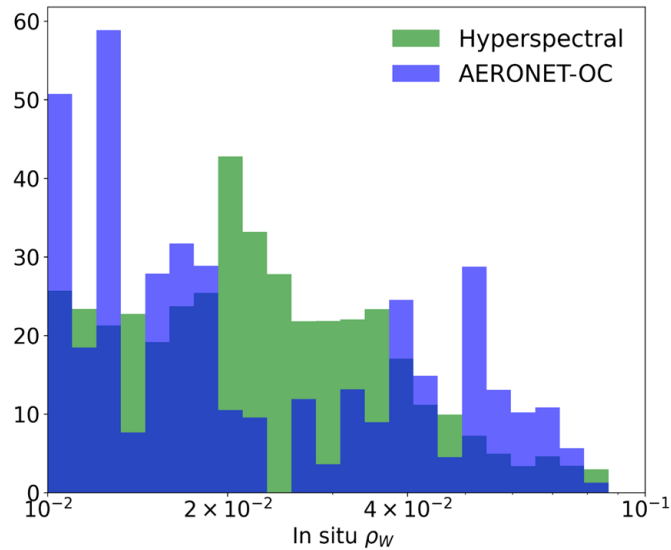


Figure 32 Frequency distribution of reflectance levels the hyperspectral (CVD) and multispectral *in situ* measurements (all wavelengths).

6.5 PERFORMANCE ASSESSMENT

In this section, results from the comparison of EnMAP standard L2A (MIP) products and ACOLITE, POLYMER and PACO-WASI AC models are presented for the comparison to AERONET-OC and to the hyperspectral matchups. Firstly, the matchups at individual sites are discussed. Then the statistical results over all common matchups for the four AC models MIP, POLYMER, ACOLITE and PACO-WASI are presented and intercompared. The study [22] additionally presents statistical results for all matchups of EnMAP-MIP to hyperspectral and multispectral *in situ* data which were much more (22 and 24, respectively) than the ones in common for all three AC models (11 and 14, respectively).

6.5.1 MULTISPECTRAL PERFORMANCE

Figure 33 - Figure 36 show the spectral comparisons between satellite and *in situ* data for the nine common AERONET-OC sites among the four EnMAP AC models. For some sites several matchups were available, but only one is shown as example. For EnMAP MIP data, two more matchups were available (MVCO and Irbe Lighthouse), and also one more for EnMAP Polymer (MVCO). Example spectra for these sites are shown as well. Overall, the R_{rs} spectra of AERONET-OC peaks slightly lower than 0.002 sr^{-1} in the blue region to maxima of around 0.025 sr^{-1} in the green region. A brief characterization of the sites and their example matchup follow:

- Venice (AAOT) and Socheongcho sites, where R_{rs} spectra are higher in the blue region and tend to decrease after about 505 nm, represent the typical shape of clear water spectra. R_{rs} is very low for Socheongcho ($<0.004 \text{ sr}^{-1}$) and shows rather large standard deviation ($\sim 20\%$).
- Bahia Blanca, Banana River, Chesapeake Bay, Irbe Lighthouse, San Marco platform, South Greenbay site, and Kemigawa sites, where R_{rs} spectra are higher in the green region (around 560 nm), represent the typical shape of turbid water spectra. While Kemigawa shows the

lowest R_{rs} values ($<0.002 \text{ sr}^{-1}$), the Bahia Blanca site presents the peak in the green region with the highest value of R_{rs} ($<0.025 \text{ sr}^{-1}$); this site is characterised as an area subject to diffuse erosion and strong tidal currents which are responsible for the typically high suspended loads in the channel, also the standard deviation is larger which is similar for Chesapeake Bay.

- In the South Greenbay site, the peak around 710 nm is very evident, compared to the other cases, this could be due to the fact that this site is characterised by a condition of hyper-eutrophication (super-richness of nutrients). A less noticeable peak around 680 nm is also visible in the case of LISCO site.
- In the Lucinda site (in the tropical coastal waters of the Great Barrier Reef lagoon near the Herbert River estuary), the spectrum shows a peak just below 550 nm and a small standard deviation of $\pm 0.0005 \text{ sr}^{-1}$.

MIP

Except for Kemigawa at all bands and for Lucinda in the blue, EnMAP-MIP matches well the AERONET-OC bands magnitudes and shape (Figure 33, $SA < 20^\circ$). For Kemigawa there is at all bands an overestimation by EnMAP-MIP, while at Lucinda for bands 400 to 490 nm EnMAP-MIP is lower than AERONET-OC. The standard deviation in R_{rs} measured by certain *in situ* measurements reflecting higher variability in the environmental conditions is similarly obtained by the EnMAP-MIP retrievals standard deviation within the 3x3 matchup pixel box.

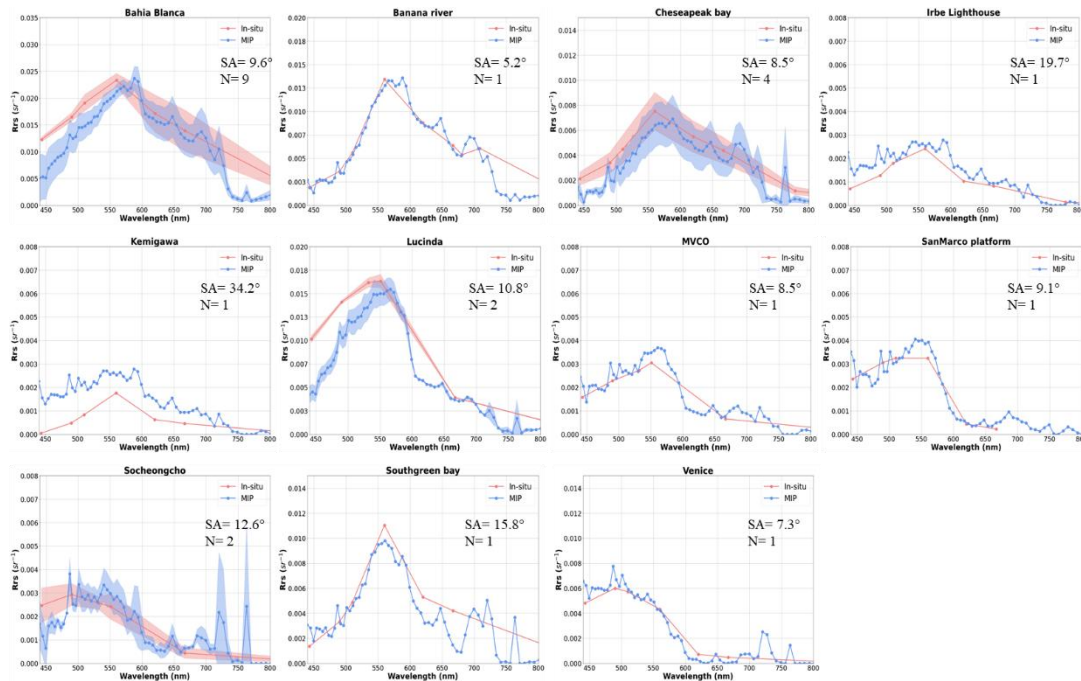


Figure 33 Spectral comparisons between EnMAP L2A water products (MIP) and in situ data in the 11 globally distributed AERONET-OC sites. The variability across the dataset in the mean spectra of MIP is displayed as blue curves, with the shaded

blue area representing the standard deviation. The mean and standard deviation of the *in situ* data are equivalently shown in red. SA represents the Spectral Angle and N represents the number of the images.

ACOLITE

EnMAP-ACOLITE overestimates Rrs at all sites significantly (Figure 34). Deviations in the spectral shape are partly large (SA 19°-40°, South Greenbay, Kemigawa, Chesapeake Bay and Banana River), but also rather low for the rest (SA 4.5°-15°). The standard deviation in Rrs measured by certain *in situ* measurements is similar to the EnMAP-ACOLITE retrievals standard deviation within the 3x3 matchup pixel box for Chesapeake Bay while it is much higher for the three other sites. Overall, the spectral shape agrees with the AERONET-OC observations; however, except for Lucinda, Kemigawa, and Bahía Blanca, the deviations are considerably larger than those observed for EnMAP-MIP.

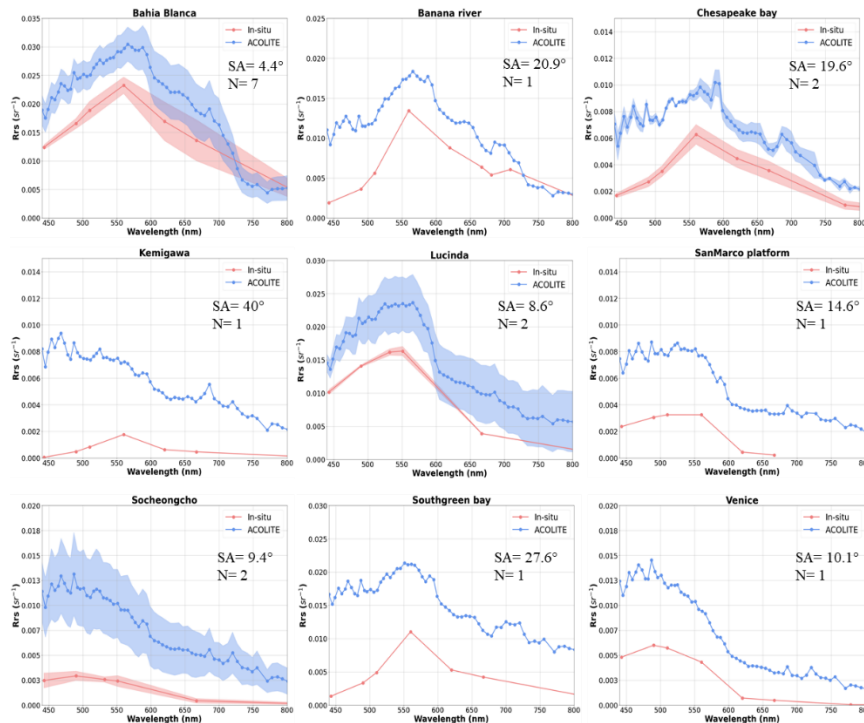


Figure 34 Spectral comparisons between ACOLITE and *in situ* data in the 9 globally distributed AERONET-OC sites. The variability across the dataset in the mean spectra of ACOLITE is displayed as blue curves, with the shaded blue area representing the standard deviation. The mean and standard deviation of the *in situ* data are equivalently shown in red. SA represents the Spectral Angle and N represents the number of the images.

POLYMER

EnMAP-Polymer deviates significantly in Rrs at all sites, except for Bahia Blanca and Chesapeake Bay where the agreement is within the standard deviation to AERONET-OC (Figure 35). Mostly the values are much higher in the blue, and much lower in the red compared to AERONET-OC. Deviation in the spectral shape are the largest among the four AC models: SA range from ~9° for Bahia Blanca and Lucinda, to ~15°-25° for Venice (AAOT), San Marco Platform, Socheongcho and MVCO and between 40° to 67° for the remaining four sites. The standard deviation in Rrs measured by certain *in situ*

measurements of AERONET-OC is only slightly larger for the EnMAP-ACOLITE retrievals standard deviation within the 3x3 matchup pixel box.

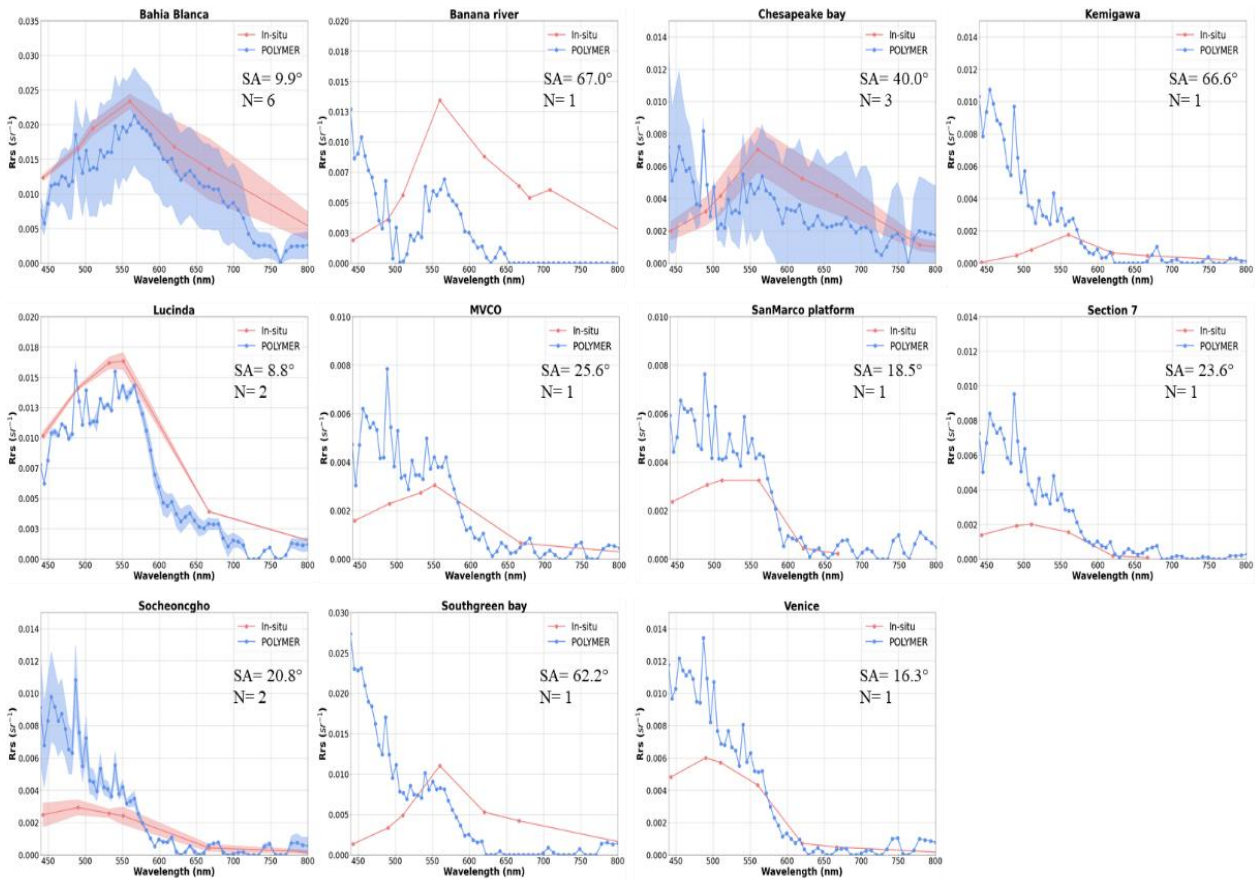


Figure 35 Spectral comparisons between POLYMER and in situ data in the 10 globally distributed AERONET-OC sites. The variability across the dataset in the mean spectra of POLYMER is displayed as blue curves, with the shaded blue area representing the standard deviation. The mean and standard deviation of the in situ data are equivalently shown in red. SA represents the Spectral Angle and N represents the number of the images.

PACO-WASI

Except for Kemigawa and MVCO, the reflectance derived by PACO-WASI matches well the AERONET-OC measurements in magnitude and shape (Figure 36). For Kemigawa, PACO-WASI overestimates reflectance in all bands strongly, and for MVCO it overestimates it from 400 to 550 nm moderately. With $R_{rs} < 0.001 \text{ sr}^{-1}$, Kemigawa has from all sites by far the lowest reflectance in the blue, which makes atmospheric correction particularly challenging. More than one matchup was available for Bahia Blanca, Chesapeake Bay, Socheoncho and Lucinda. For the first three, the standard deviation of the *in situ* measurements is high, reflecting a high temporal variability in the environmental conditions. A very similar variability is obtained from PACO-WASI. The overlapping standard deviations of both datasets indicate a good correspondence of PACO-WASI reflectance with the *in situ* measurements.

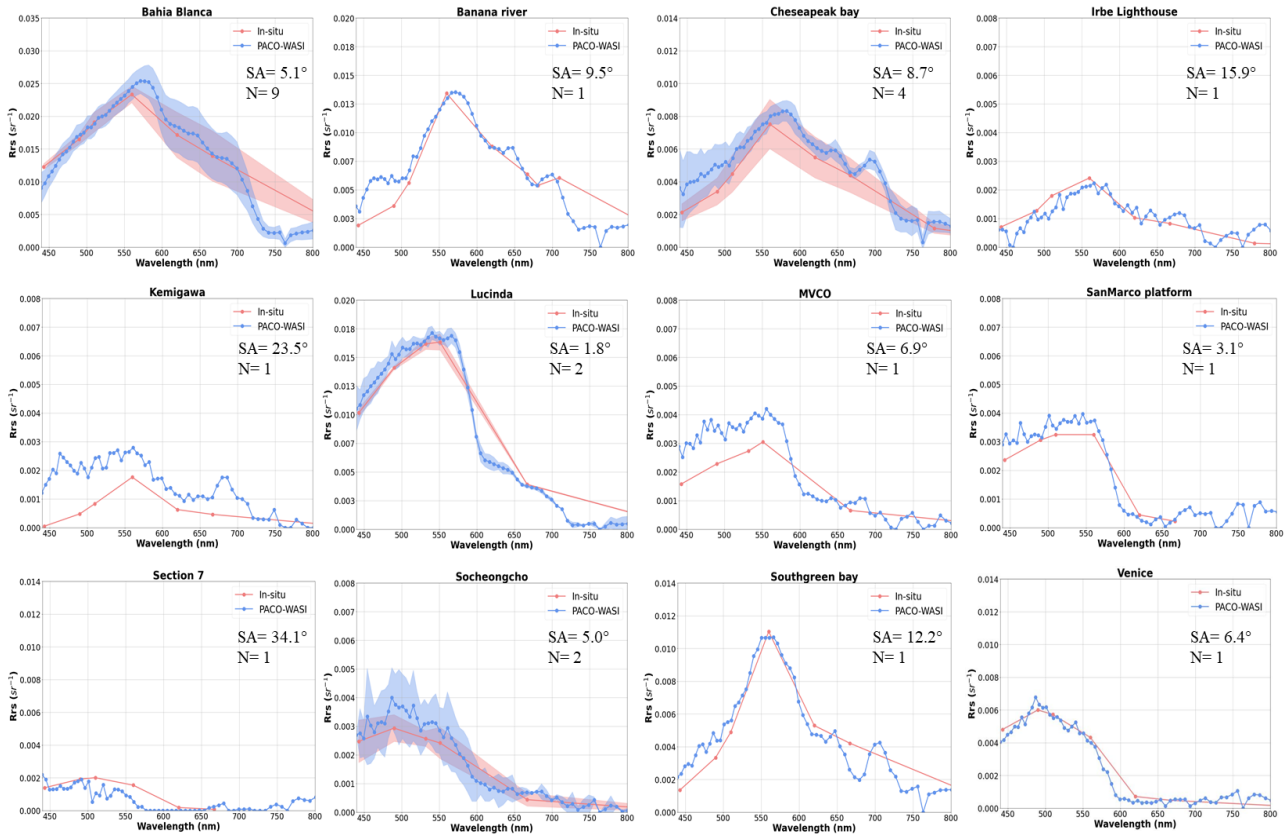


Figure 36 Spectral comparisons between PACO-WASI and in situ data in the 12 globally distributed AERONET-OC sites. The variability across the dataset in the mean spectra of PACO-WASI is displayed as blue curves, with the shaded blue area representing the standard deviation. The mean and standard deviation of the in situ data are equivalently shown in red. SA represents the Spectral Angle and N represents the number of the images.

Summary

The common multispectral dataset for EnMAP contains 14 match-ups with AERONET-OC data from nine study sites: one at AAOT, four at Bahia Blanca, one at Banana River, two at Cheasepeake Bay, one at Kemigawa Offshore, one at San Marco Platform, one at Socheongcho, one at South Greenbay and two at LJCO. Figure 37 shows the overall performance of AC processors using all the AERONET-OC match-ups for each EnMAP AC model separately with all the EnMAP satellite data combined. Table 11 summarizes the statistical metrics of the AC model performance for each reference band as plotted in Figure 37.

Regarding RMSD and MAD, the best performance, i.e. the lowest values at the five bands, was obtained for PACO-WASI, closely followed by MIP. The two other AC models show much higher values. For MAPD, MIP is best (except at 620 nm where POLYMER is slightly better), followed by POLYMER and PACO-WASI (which is even slightly better than MIP at 667 nm). The mean bias is best at 443 nm and 490 nm for MIP; at 560 nm for POLYMER and PACO-WASI; at 620 nm for PACO-WASI, and at 667 nm for POLYMER (very closely followed by MIP). Generally, the mean bias is quite high at 443 nm for all four methods (worst for PACO WASI with 131%). While ACOLITE performed worst for the previous metrics, it performed similarly well to PACO-WASI and even better than PACO-WASI at 443

nm. MIP showed the weakest results here. Concerning the slope, PACO-WASI is closest to 1 for all bands, except at 443 nm, where ACOLITE is slightly better. For all methods, the regression at 443 nm is much worse than for all other bands, ranging from anti-correlation in case of POLYMER (slope = -0.24) to not more than 0.75 (ACOLITE). POLYMER and MIP still show no convenient regression at 490 nm (slopes of 0.61 and 0.71, respectively), but ACOLITE and PACO-WASI are close to 1. All methods reveal slopes between 0.75 and 1.09 at the remaining bands at 560 nm, 620 nm and 667 nm.

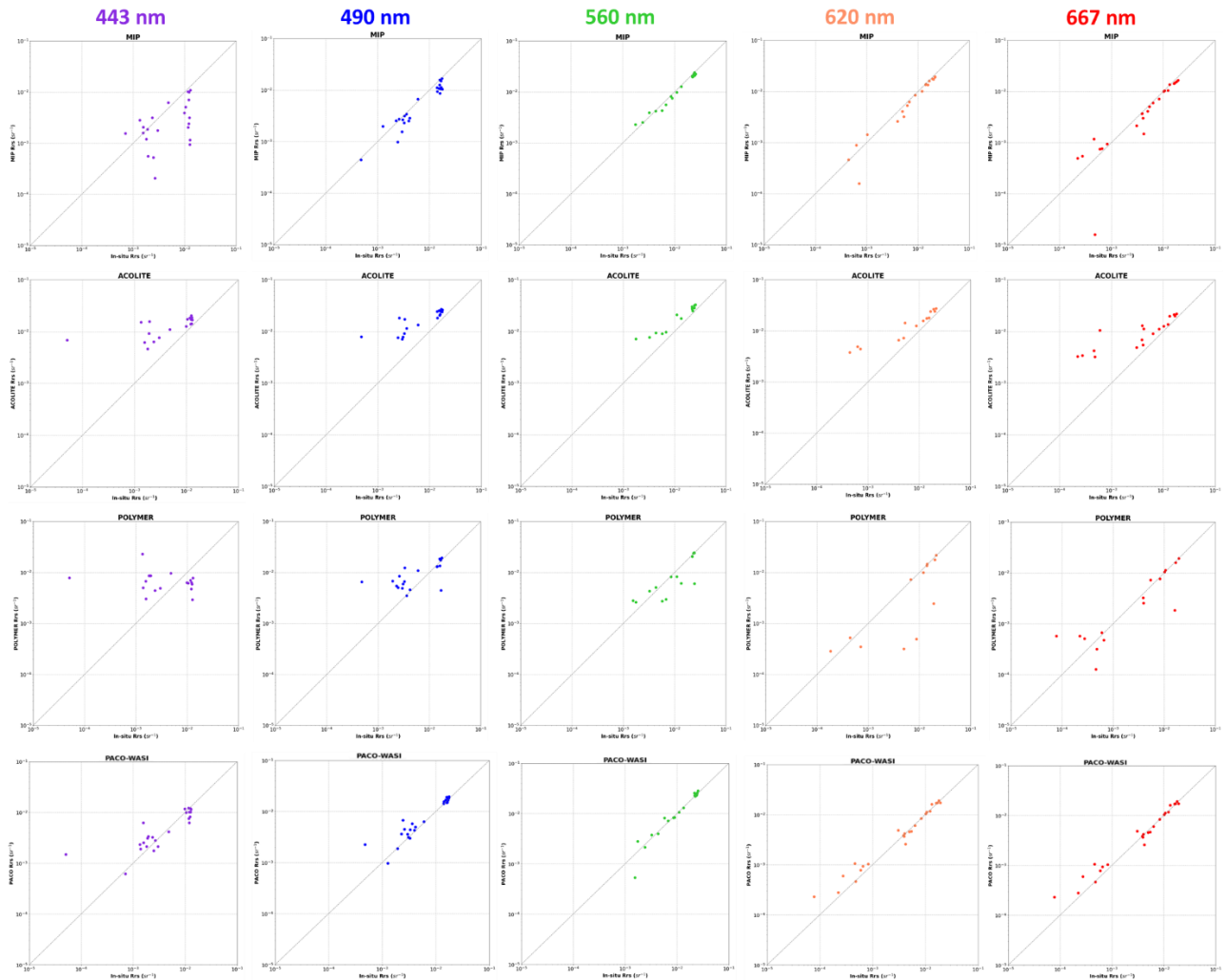


Figure 37 Overall performance of AC processors using the AERONET-OC match-ups with all the satellite data combined. The number of matchups per processor and per band is reported in Table 11 along with the statistics. The black lines refer to the 1:1 line.

Table 11 Summary of the five statistical metrics for the EnMAP matchup data shown in Figure 37. *N* represents the total number of samples for each band.

		<i>RMSD (sr⁻¹)</i>	<i>MAD (sr⁻¹)</i>	<i>MAPD (%)</i>	<i>Mean bias (%)</i>	<i>Slope</i>	<i>N</i>
443 nm	MIP	0.0053	0.0036	57	-30	0.35	24
	ACOLITE	0.0068	0.0060	936	936	0.75	18
	POLYMER	0.0074	0.0061	1023	981	-0.24	20
	PACO WASI	0.0022	0.0016	153	131	0.71	25
490 nm	MIP	0.0032	0.0022	25	-17	0.73	24
	ACOLITE	0.0084	0.0078	224	224	0.96	18
	POLYMER	0.0046	0.0034	138	127	0.61	21
	PACO WASI	0.0015	0.0011	38	34	0.97	25
560 nm	MIP	0.0017	0.0014	11	-5	0.90	19
	ACOLITE	0.0059	0.0055	69	69	1.07	14
	POLYMER	0.0054	0.0029	31	-6	0.82	16
	PACO WASI	0.0014	0.0010	14	4	1.05	20
620 nm	MIP	0.0014	0.0011	19	-10	0.92	19
	ACOLITE	0.0050	0.0046	177	177	1.09	14
	POLYMER	0.0055	0.0032	46	-34	0.83	15
	PACO WASI	0.0014	0.0009	30	-6	1.07	20
667 nm	MIP	0.0013	0.0009	32	4	0.88	24
	ACOLITE	0.0048	0.0041	355	355	0.96	18
	POLYMER	0.0036	0.0015	78	32	0.78	18
	PACO WASI	0.0009	0.0006	31	23	1.01	25

Figure 38 summarizes the results for the statistical parameters ϵ and β . In terms of Median Symmetric Accuracy (ϵ , Figure 38 left panel), PACO-WASI performs best, followed by MIP. PACO-WASI meets the 30% threshold [18] very well for all bands except 443 nm (38%), and MIP meets the 30% threshold well for the green and red bands, while the error is much higher at 443 nm (110%) and slightly above the threshold for 490 nm (32%). ACOLITE and POLYMER exhibit higher errors across all five bands, most notably for the blue bands (>95% and >75%, respectively). POLYMER shows higher accuracy than ACOLITE but has the largest error at 443 nm among the four AC models.

Regarding the Median Symmetric Bias (β , Figure 38, right panel), PACO-WASI shows the lowest median symmetric Bias, which is positive (5-10%) for all bands except 443 nm (-7%). MIP shows the second lowest values for β , which are negative for all bands (largest for 443 nm with 65%, lower for the other bands with 5-15 %). POLYMER shows a higher positive β than MIP's negative β for the blue bands, and similar negative bias for the other bands. ACOLITE obtains highest β values which are always positive.

One has to keep in mind that in this intercomparison, PACO-WASI is based on an improved version of the EnMAP L1 and L2A data as compared to the other three AC methods which may explain some of the better performance. Furthermore, processing was not done automatically as for the other softwares but required time-consuming optimization of inversion by experts. In addition, the number of valid matchups varies among the different AC methods, but also among the different wavelengths.

Comparisons only considering the same matchups are preferred for a ranking of methods, as has been provided for EnMAP-MIP, -POLYMER and -ACOLITE in [22].

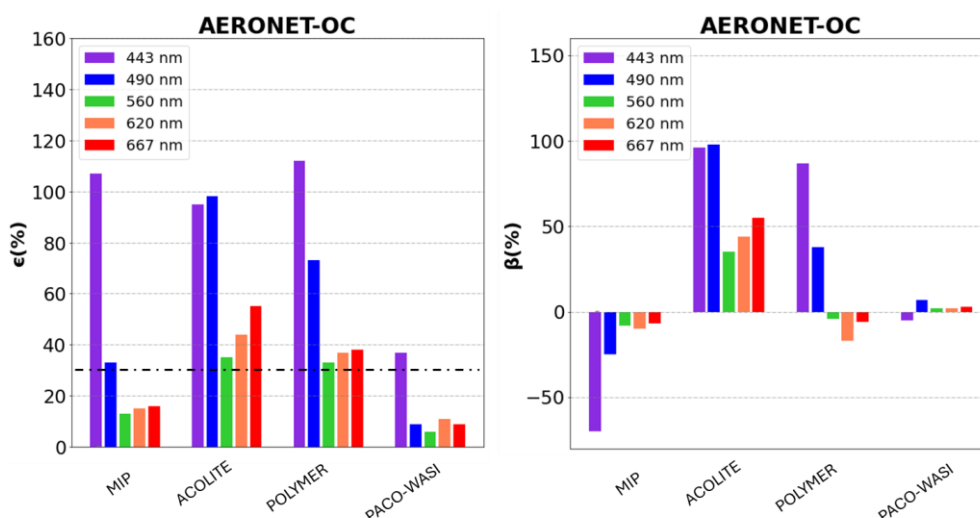


Figure 38 Performance assessments as determined by the Median Symmetric Accuracy (ϵ) and median symmetric Bias (β) for all the match-ups combined. The dashed line corresponds to a 30% threshold [18].

6.5.2 HYPERSPECTRAL PERFORMANCE

Figures 39, 40, 41 and 42 show examples of the spectral comparisons between satellite and *in situ* data for the four-common hyperspectral *in situ* data sites (AAOT, Lake Constance, Lampedusa, Lucinda) among the four EnMAP AC models. Additionally, for EnMAP-MIP two more matchups were available (Oostende and Lake Trasimeno), while for EnMAP-Polymer only matchups were available for Lake Trasimeno and for EnMAP-ACOLITE only for Oostende. Some of these sites had several matchups, but only one is shown as example. Overall, the Rrs spectra of hyperspectral *in situ* peaks slightly lower than 0.007 sr^{-1} in the blue region to maxima of around 0.027 sr^{-1} in the green region. A brief characterisation of the sites and their example matchup follows:

- Lampedusa where Rrs spectra are highest at 400nm and continuously decreasing to the red, showing very clear (open ocean) water spectra, although the water depth at the station is just 20 m. Rrs is quite low ($<0.007 \text{ sr}^{-1}$) but not as low as found for the AERONET-OC site Socheongcho (Chapter 4.2.1).
- Venice (AAOT), where Rrs spectra peak at 500-530 nm and are a bit higher in the green than the blue region, decrease a lot in the red, but still have some contribution at 600 to 700 nm, showing more mesotrophic with little CDOM but some sediment. It shows less clear water conditions as opposed to the matchup shown for AAOT in 4.2.1. There is quite a large standard deviation ($>20\%$) indicating dynamic (most likely suspended sediment) conditions during matchup.
- Lake Constance: a rather deep (mean depth 100m), subalpine glacial lake, where Rrs spectra peak at 535 nm, are much higher in the green than the blue region, indicating significant CDOM

loading as compared to sediments. There is a strong decrease in the red part, but still some Rrs left. It indicates mesotrophic water conditions with rather low chlorophyll-a concentration.

- Lucinda is in the tropical coastal waters of the Great Barrier Reef lagoon near the Herbert River estuary; the spectrum shows a peak at 560 nm and also a rather large standard deviation up to 50% indicating highly variable suspended loads during the matchup.
- Oostende is a coastal site where Rrs spectra are higher in the green region (around 560 nm), represent the typical shape of the turbid water spectra, but also significant contribution of CDOM absorption. It presents the peak in the green region with the highest value of Rrs ($<0.027 \text{ sr}^{-1}$); this site is characterised as an area subject to diffuse erosion and strong tidal currents which are responsible for the typically high suspended loads in the channel.
- Lake Trasimeno (meso-eutrophic): is a shallow tectonic lake, with the Rrs peak around 0.0025 sr^{-1} in the green region. The spectrum shows reflectance peaks and dips in the range 670-700 nm related to the presence of Chl-a.

MIP

Overall, we observe very good agreement between EnMAP-MIP and *in situ* spectra for the different water sites and reflectance magnitudes and the spectral shape is well kept (SA between 2.9 to 8.2°; Figure 39). The highest disagreement was observed at Oostende, a region with typical turbid and very turbid waters [48]. The underestimation of MIP at Oostende might be improved by the new EnMAP processor version (introduced in March 2025) that should fix the issue of the different water types in the MIP processor, as now all products are retrieved using the clear water option. Three low-quality images of LJCO were acquired on dates (July 08, August 15, and August 16, 2022) when *in situ* reflectance exhibited high temporal variability (highlighted by the shaded green region). As previously mentioned, on these days, we compared the EnMAP data to the mean of the 15-minute window (indicated by the dashed green line). In the red-NIR region, there are still atmospheric absorption features that are not completely removed, in particular the O2 band around 760 nm. Overall, spectral noise, specially at shorter wavelengths, is observed in the EnMAP-MIP product and it is mostly due to an insufficient sampling in the convolution to compute water look-up-tables in MIP. This issue was recently fixed and will be implemented in the next EnMAP processor version. These band-to-band spectral variations are also observed in the PRISMA data by [24] and [76] and CHRIS-PROBA by [95], possibly a result of inter-band calibration issues.

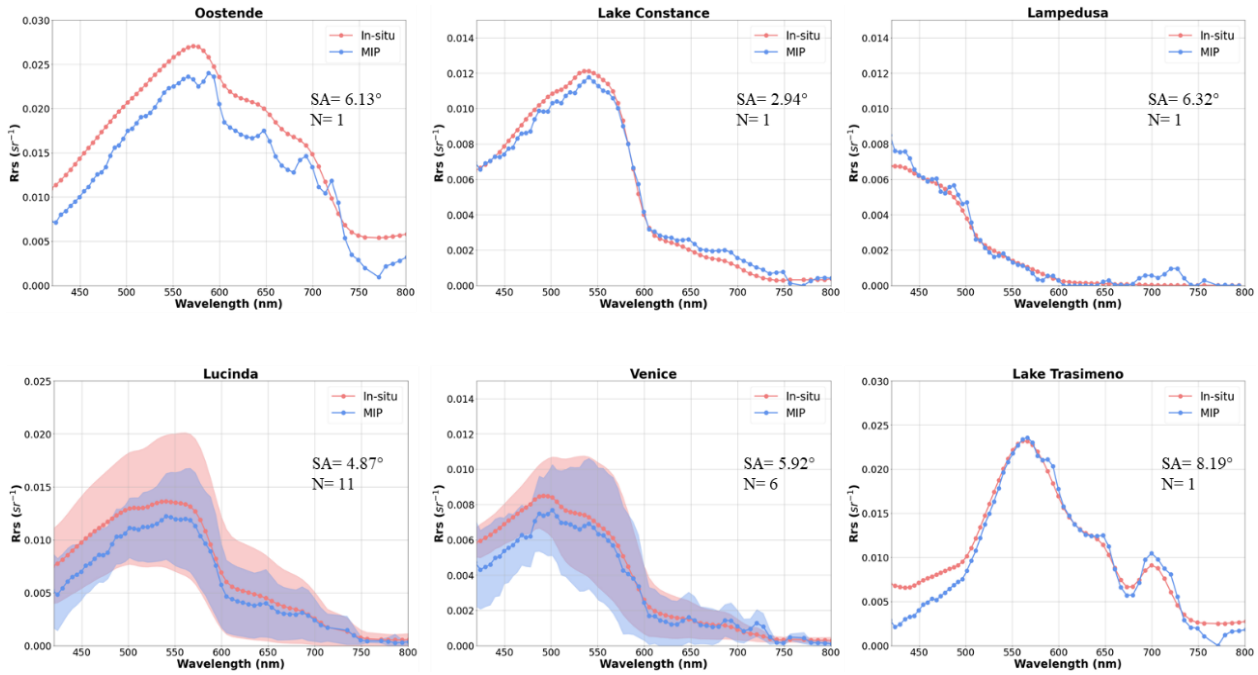


Figure 39 Spectral comparisons between EnMAP L2A standard products (MIP) and hyperspectral in situ data in the 6 sites of the CVD. The variability across the dataset in the mean spectra of MIP is displayed as blue curves, with the shaded blue area representing the standard deviation. The mean and standard deviation of the in situ data are equivalently shown in red. SA represents the Spectral Angle and N represents the number of the images.

ACOLITE

EnMAP-ACOLITE agrees very well at Oostende (better than EnMAP-MIP) and is within the standard deviations at Lucinda, but still has a significant higher mean value. It shows strong overestimation for the entire spectrum for Lake Constance and Lampedusa (Figure 40). It meets mostly well the spectral shape (SA between 4.3° to 20.1°). The overestimation along the spectrum probably results from residual sun glint or the inaccurate estimation of the aerosol model used in the AC as observed by [24] in their study of AAOT ACOLITE applied to PRISMA data. [22] tested ACOLITE with the glint correction applied to EnMAP data; it reduced the number of high quality hyperspectral match-ups from 11 to three match-ups (two at AAOT and one at Oostende). Considering the common hyperspectral match-ups, this number is reduced from 11 to two match-ups only (two at AAOT). Applying the glint correction indeed improves the overestimation (see Supplement 1 in [22]), as reported by [24] for PRISMA and by [96] for S2-MSI, but also flagged out reliable match-ups as at Lake Constance and Lucinda (and Bahia Blanca for comparison to AERONET-OC). ACOLITE is recognized to work especially well in productive and turbid waters where it is the main intended use [48,96] as confirmed by our results.

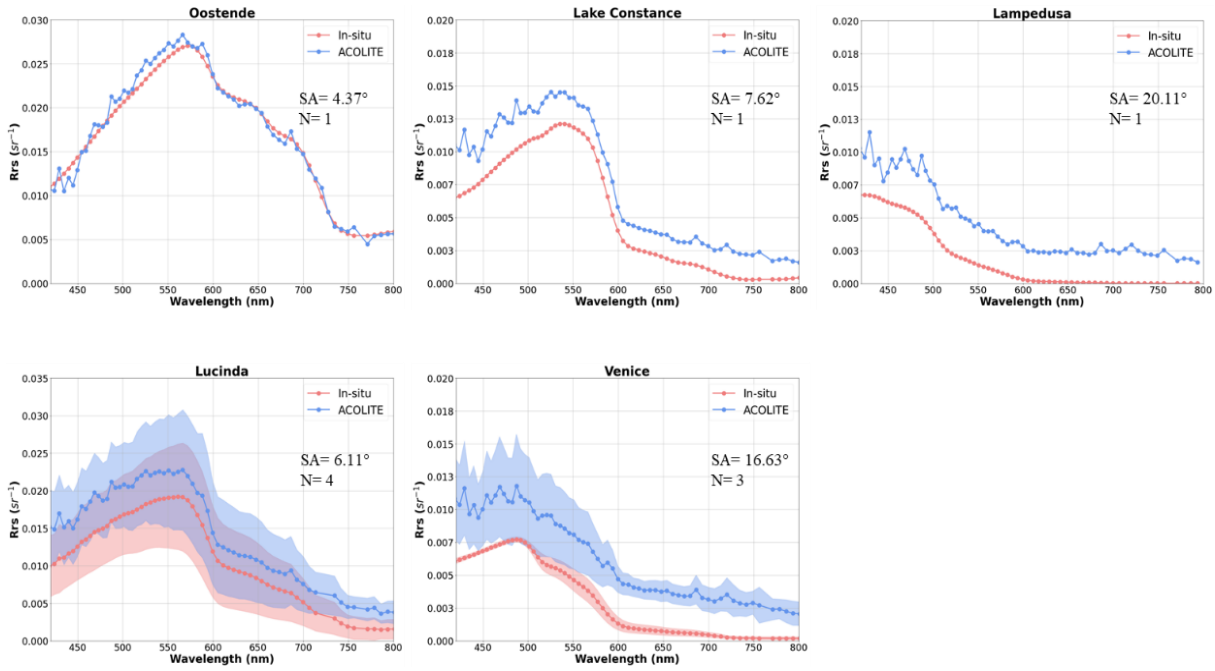


Figure 40 Spectral comparisons between ACOLITE and hyperspectral *in situ* data in the 5 sites of the CVD. The variability across the dataset in the mean spectra of ACOLITE is displayed as blue curves, with the shaded blue area representing the standard deviation. The mean and standard deviation of the *in situ* data are equivalently shown in red. SA represents the Spectral Angle and N represents the number of the images.

POLYMER

EnMAP-Polymer Rrs agrees well at Lake Constance, Lucinda and Lake Trasimeno and meets similar to EnMAP-ACOLITE mostly well for all five spectra the spectral shape of *in situ* (SA between 4.0° to 20.4°, Figure 41). It shows slightly lower standard deviation for AOT and Lucinda than *in situ*. However, it shows very strong overestimation in the 418 - 600 nm range for Lampedusa and also in the blue for Venice (AAOT). On two occasions when the *in situ* spectra at AAOT transitioned to more productive waters, the Polymer [pW]N retrievals show considerable improvement (see other matchups in Figure 8 in [22]), as observed at Lake Trasimeno too. However, the analysis of the AERONET-OC dataset (section 4.2.1) reveals that this overestimation is not restricted solely to clear waters. Multispectral match-ups of Polymer show good agreement in turbid waters, such as at Bahia Blanca and Chesapeake Bay (see other matchups in Figure 8 in [22]), but inferior performance at sites like Socheongcho, characterized by clearer waters. These results are consistent with the match-up comparisons from the hyperspectral dataset. Nevertheless, the retrievals of Polymer in inland and coastal sites as shown in Figure 35 for Banana River, Chesapeake Bay, and South Greenbay also show inferior performance. One reason for the poorer results may be our decision not to use any flag information provided by Polymer. A closer examination of the bitmask information show instances where the same flag "6144" (indicating inconsistent results and excessive differences at 412 nm between retrieved and modelled water reflectance) correctly identified a bad match-up as at the Lampedusa site but erroneously flagged reliable match-ups at LJCO or Lake Trasimeno. Employing these flags would have limited our analysis to only a few match-ups.

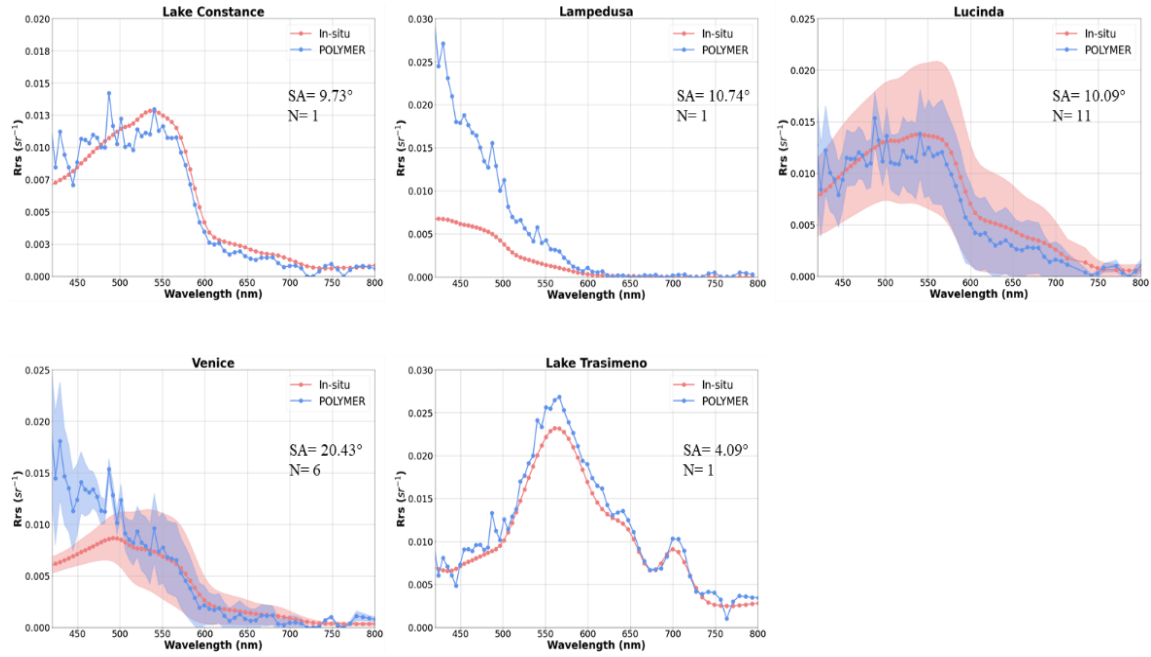


Figure 41 Spectral comparisons between POLYMER and hyperspectral *in situ* data in the 5 sites of the CVD. The variability across the dataset in the mean spectra of POLYMER is displayed as blue curves, with the shaded blue area representing the standard deviation. The mean and standard deviation of the *in situ* data are equivalently shown in red. SA represents the Spectral Angle and N represents the number of the images.

PACO-WASI

Rrs derived with PACO-WASI agrees in general very well with all *in situ* measurements, both in magnitude and spectral shape (Figure 43). The agreements and differences are similar to those of MIP (Figure 39). Excellent correspondence was obtained for Lake Constance, Lampedusa, Lucinda and Lake Trasimeno, except in the blue for Lampedusa (overestimation) and Lake Trasimeno (underestimation). For the 6 matchups of Venice, the average agreement is good and falls very well within the standard deviation. The lowest correspondence is observed for Oostende, where the *in situ* data have an offset of 0.003 sr^{-1} compared Rrs from PACO-WASI. The spectral shape of the *in situ* measurements is generally very well reproduced (SA between 1.77° to 7.96° , Figure 43).

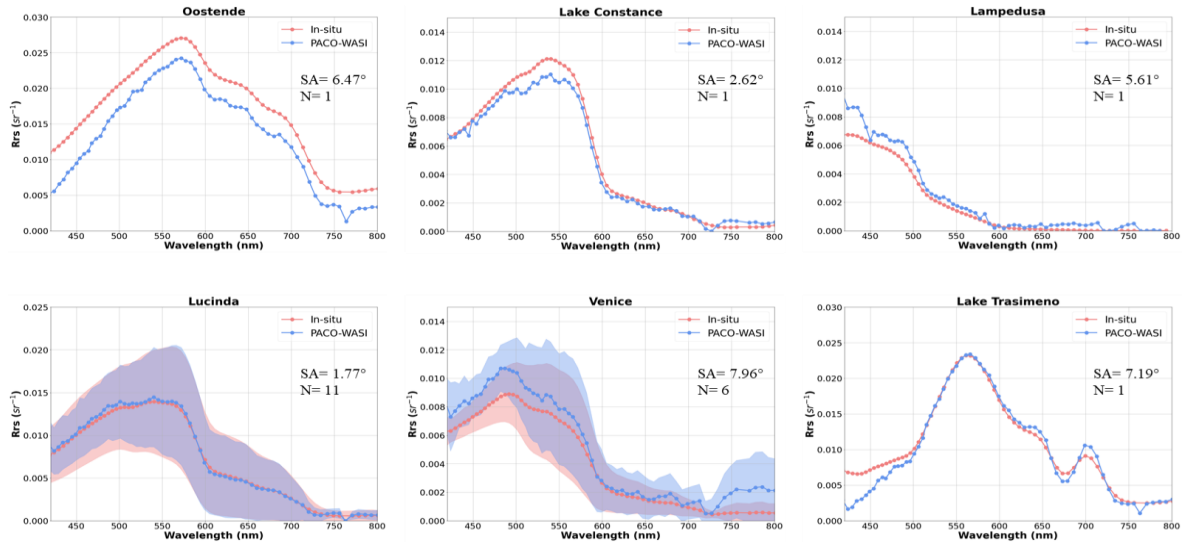


Figure 42 Spectral comparisons between PACO-WASI and hyperspectral in situ data in the 6 sites of the CVD. The variability across the dataset in the mean spectra of PACO-WASI is displayed as blue curves, with the shaded blue area representing the standard deviation. The mean and standard deviation of the in situ data are equivalently shown in red. SA represents the Spectral Angle and N represents the number of the images.

Summary

The statistical metrics resulting from the match-up analysis were then computed; notably for the CVD hyperspectral dataset we have taken directly the results from [22] where we merged the results obtained with PACO-WASI. The resulting spectra of ϵ , β , RMSE and MdAPE (corresponding to the MAPD statistic implemented in ACIX-III Aqua) for common hyperspectral match-ups ($n=11$) to all EnMAP AC results are shown in Figure 43 and summarized in Table 12. The largest uncertainties are associated with wavelengths < 450 nm (Figure 10 and Table 7 in [22]) which are decreasing towards the red, except for ACOLITE. Also for the hyperspectral PRISMA Rrs product, higher errors in the blue and in the red spectral regions was reported by [24].

The required uncertainty defined by the EnMAP ground segment for land applications was only achieved by MIP and PACO-WASI (a requirement for EnMAP water products does not exist). MIP and PACO-WASI perform best, with PACO-WASI showing more variability in the statistical metrics along the spectrum.

To clarify the reason for the different results of the processors, more tests are needed including performance testing and optimisation of settings which was not done here and it is a limitation of our study. For example, it should be investigated whether excluding the blue spectral region (410-440 nm) from POLYMER's spectral bands could improve the observed overestimation. In the case of ACOLITE we used all the default flags, but avoiding the use of some flags may provide useful information about the processor or sensor. Furthermore, most of the flagged pixels in ACOLITE were due to negative reflectance, and avoiding this flag when processing the images would have shown in which part of the wavelength spectrum these negative values occur.

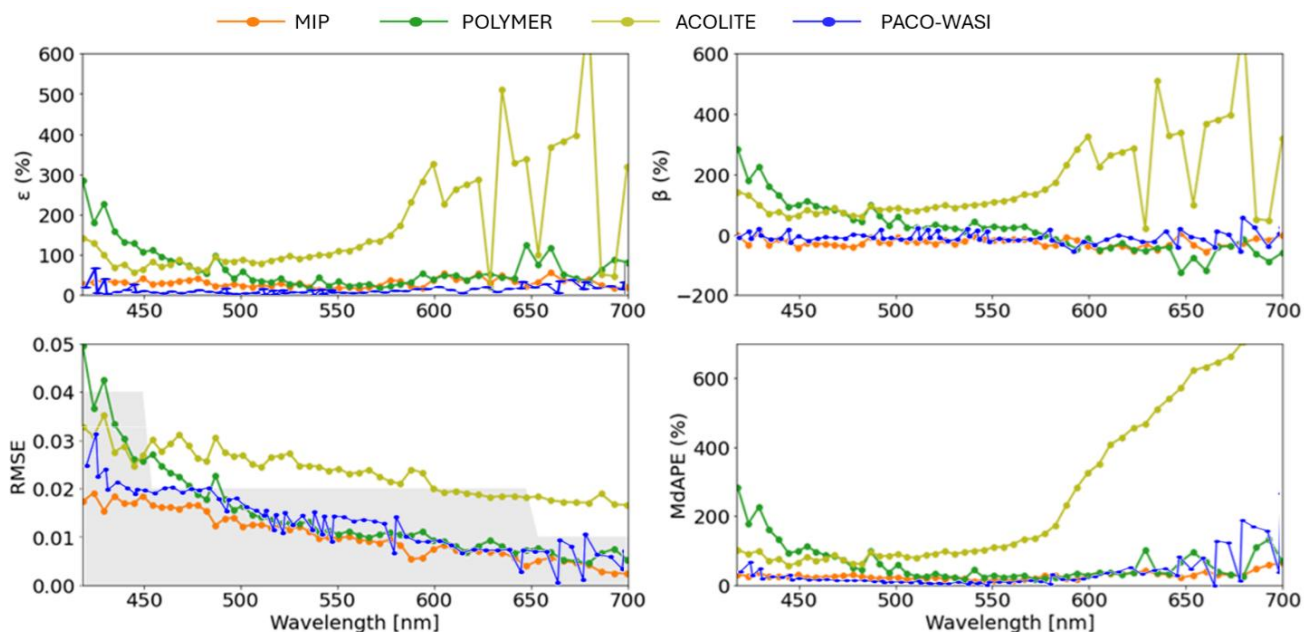


Figure 43 Spectra of ϵ , β , RMSE and MdAPE for MIP, Polymer, ACOLITE and PACO-WASI for coincident hyperspectral match-ups during the operational mission phase (N=7). The grey shaded area represents the required uncertainty (RMSE) outside of strong atmospheric absorption regions as defined by the EnMAP Ground Segment and for AOT at 550 nm lower than 0.4 [22].

Table 12 Statistics of MIP, Polymer, ACOLITE and PACO-WASI for two wavelength ranges using the common hyperspectral dataset (both mission phases).

Wavelength range	AC	ϵ (%)	β (%)	RMSD	MdAPE(%)
418-450 nm	MIP	26.87	-15.84	0.01	21.99
	ACOLITE	68.85	68.85	0.02	67.23
	POLYMER	118.78	105.24	0.03	97.97
	PACO-WASI	19.07	2.42	0.01	26.45
451-700 nm	MIP	19.68	-17.01	0.01	18.45
	ACOLITE	79.34	79.34	0.02	87.56
	POLYMER	37.45	-9.53	0.01	30.35
	PACO-WASI	13.46	1.17	0.004	27.19

7 CONCLUSIONS

This study presented the results of the ACIX-III Aqua project, a global intercomparison exercise aimed to test different AC methods on satellite hyperspectral data acquired by the PRISMA hyperspectral mission. Five AC processors were tested in ACIX-III: ACOLITE, hGRS, iCOR, MIP, and POLYMER. In addition to these processors, the standard AC products of PRISMA L2C was incorporated into the comparative analysis. The evaluation encompassed T-Mart, a system used to correct for adjacency effects, which was applied prior to the ACOLITE atmospheric correction. The testing of the AC methods was performed with a set of *in situ* measurements of Rrs at both multispectral (AERONET-OC) and hyperspectral (CVD) resolutions.

The evaluated dataset was composed by a total of 174 PRISMA images with *in situ* data derived from the AERONET-OC and of 65 images with *in situ* data obtained from the CVD, yielding a total of 239 images. The match-up analysis is provided both per site and across seven different OWTs. As the evaluation was limited to the single point for which *in situ* data were available, a QWIP analysis was also included to show spatial variability of Rrs spectra image by image and for AC method.

A further analysis was conducted on EnMAP, as three of the five AC methods (namely ACOLITE, POLYMER and MIP) were recently tested for similar purposes by [22]. These tests were supplemented by an analysis for PACO-WASI, which corrects the product of a land AC processor (PACO) for sun glint, sky glint and path radiance errors (WASI). The report hence explores the comparison between EnMAP and field data from the launch of this more recent mission in 2022 until the end of 2023, based on 28 matchups (likewise originated both from AERONET-OC and CVD). This assessment of EnMAP products, presented in [22] and now extended with results from ENMAP-PACO-WASI, confirmed that some methods allow to correct its Level 1 data for atmospheric and surface effects to retrieve the surface reflectance over different water sites within the uncertainties specified for land. In near-future, a larger match-up dataset will allow the assessment of EnMAP for more optical water types. Further evaluation will especially benefit from cross-comparing the EnMAP reflectance products to other satellite missions such as DESIS, PRISMA, and S2-MSI. The *in situ* data from various projects and study sites equipped with autonomous hyper- and multispectral radiometers played a crucial role in this study. Funding agencies are encouraged to continue supporting the advancement of this technology and the expansion of the instrument network, taking into consideration the dynamic characteristics of most aquatic ecosystems and the upcoming hyperspectral missions.

The ACIX-III Aqua results were consistent with previous findings of ACIX-Aqua [18], in which a set of the AC methods tested in this study were applied to Landsat-8 and Sentinel-2 images. Comparisons between PRISMA and *in situ* data for Rrs in the six predefined spectral bands ranging from 443 to 709 nm showed that none of the AC methods performed better than the others, with the exception of PRISMA that showed in general the poorest performance. Notably, the greatest discrepancies between satellite and *in situ* data were observed in the blue and NIR bands, whereas better agreement was evident in the green region of the spectrum. The level of agreement between AC models and CVD

was slightly higher than for AERONET-OC; indeed, for CVD most of the AC methods produced data that satisfied the 30% accuracy threshold recommended by the GCOS for Rrs.

Additionally, each atmospheric correction processor showed varying degrees of accuracy depending on the Optical Water Type (OWT); these data were in fact representative of eight OWTs that encompass blue, phytoplankton-rich, turbid and humic waters in marine and lacustrine ecosystems. Analysing the heatmaps helped illustrate how method performance depends on water properties, indicating the AC method with the lowest ϵ for each combination of OWT and spectral band. OWT analysis was not conducted for EnMAP due to the lower number of samples.

To conclude, ACIX-III Aqua has provided a valuable framework for understanding how state-of-the-art atmospheric correction methods perform when applied to PRISMA and EnMAP, which have been offering relevant observations for water applications. In particular, the study provides an overview of the comparison of field- and satellite-derived Rrs values for specific PRISMA bands over 26 globally distributed inland and coastal water sites, using a dataset spanning from 2020 to 2024. Nonetheless, some elements have to be considered for improving the exercise:

- Some of the AC methods are also providing estimates of AOT; a comparison of such estimation with reference data from AERONET and CVD networks (e.g., Microtops II) would provide further elements to evaluate the AC methods.
- The QWIP analysis, presented here just as an example, would merit further investigation to obtain a vision across the entire image (30 km by 30 km) rather than the direct comparison in a limited portion (i.e. 90 m x 90 m); this would allow to appreciate how AC methods perform in shallow waters, with clouds etc.
- A deeper analysis should be undertaken to consider the uncertainties (e.g., geo-location) associated with both in situ and satellite data, and to evaluate the impact on the estimation of biophysical parameters, as performed in previous ACIX-Aqua studies [18].
- Both PRISMA and EnMAP have not been specifically designed to meet the observational requirements (e.g., high signal to noise ratio) for developing aquatic applications so that the AC results are of course depending on the properties of these satellite data.
- Further analysis is required to understand how the variations in AC performance are related to the increased hyperspectral information content of PRISMA/EnMAP and how the results of this exercise compare to those obtained with other satellites (e.g. PACE).

The analysis is hence not ending and we do hope that such work will prosecute also to support the generation of improved products for aquatic applications from hyperspectral data collected by future mission, such as CHIME and SBG.

8 ACKNOWLEDGMENTS

This work would not have been possible without access to high-quality in situ data. We are deeply grateful to the AERONET-OC Principal Investigators: J. Ishizaka, K. Arai, H. Loisel, P. Pratolongo, R. Frouin, M. Talone, F. Mélin, B. Bulgarelli, G. Zibordi, H. Higa, T. Moore, S. Ruberg, M. Wang, S. Ahmed, A. Gilerson, T. Schroeder, Y.J. Park, B. Jones, M. Ragan, D. Aurin, H. Sosti, S. Ladner, and D. Van der Zande. We also acknowledge the contributions of the Joint Research Centre (JRC) of the European Commission, JAXA's GCOM-C project, the Integrated Marine Observing System (IMOS)—enabled by the National Collaborative Research Infrastructure Strategy (NCRIS)—and the HYPERNETS H2020 project for providing hyperspectral data from AAOT and Lampedusa. Special thanks go to Mauro Musanti and Salvatore Mangano for their fieldwork in Italy; Mara Gomes, Milad Niroumand-Jadidi, the Phytooptics group members, and LUBW/ISF for their support during the Lake Constance EnMAP validation campaigns. We are grateful to Angelo Amodio and Luigi Agrimano from Planetek for their valuable support in handling PRISMA products. We thank Roberta Pozzi and Simone Lella from CNR-IREA for supporting data handling and storage. We are also grateful to all contributors and supporters of the EnMAP Cal/Val Water Project. We sincerely thank Shun Bi for valuable discussions on optical water types. This work was supported by: the Italian Space Agency through the PRISCAV Project (grant no. 2019-5-HH.0) and PANDA-WATER Project (contract ASI no. 2022-15-U.0); the European Space Agency (contract no. 4000139081/22/I-EF, HYPERNETS-POP); the Horizon 2020 HYPERNETS project (grant agreement no. 775983); the Bundesministerium für Wirtschaft und Klimaschutz (grants 50EE1915, 50EE1923, 50EE2401); the DLR for funding the EnMAP mission; The Swiss National Science Foundation (SNSF) under the Lake3P project (grant no. 204783); The Swedish National Space Agency (Dnr. 2021-00050); the Belgian Science Policy Office through the TERRASCOPE project (contract no. CB/67/12).

9 REFERENCES

1. Strong, A.E. Remote Sensing of Algal Blooms by Aircraft and Satellite in Lake Erie and Utah Lake. *Remote Sens Environ* **1974**, 3, 99–107, doi:10.1016/0034-4257(74)90052-2.
2. Shi, W.; Wang, M. Three-dimensional Observations from MODIS and CALIPSO for Ocean Responses to Cyclone Nargis in the Gulf of Martaban. *Geophys Res Lett* **2008**, 35, doi:10.1029/2008GL035279.
3. Stumpf, R.P.; Wynne, T.T.; Baker, D.B.; Fahnenstiel, G.L. Interannual Variability of Cyanobacterial Blooms in Lake Erie. *PLoS One* **2012**, 7, e42444, doi:10.1371/journal.pone.0042444.
4. Bresciani, M.; Adamo, M.; De Carolis, G.; Matta, E.; Pasquariello, G.; Vaičiūtė, D.; Giardino, C. Monitoring Blooms and Surface Accumulation of Cyanobacteria in the Curonian Lagoon by Combining MERIS and ASAR Data. *Remote Sens Environ* **2014**, 146, 124–135, doi:10.1016/j.rse.2013.07.040.
5. Matthews, M.W.; Odermatt, D. Improved Algorithm for Routine Monitoring of Cyanobacteria and Eutrophication in Inland and Near-Coastal Waters. *Remote Sens Environ* **2015**, 156, 374–382, doi:10.1016/j.rse.2014.10.010.
6. Tyler, A.N.; Hunter, P.D.; Spyrakos, E.; Groom, S.; Constantinescu, A.M.; Kitchen, J. Developments in Earth Observation for the Assessment and Monitoring of Inland, Transitional, Coastal and Shelf-Sea Waters. *Science of The Total Environment* **2016**, 572, 1307–1321, doi:10.1016/j.scitotenv.2016.01.020.
7. Pahlevan, N.; Schott, J.R.; Franz, B.A.; Zibordi, G.; Markham, B.; Bailey, S.; Schaaf, C.B.; Ondrusek, M.; Greb, S.; Strait, C.M. Landsat 8 Remote Sensing Reflectance (Rrs) Products: Evaluations, Intercomparisons, and Enhancements. *Remote Sens Environ* **2017**, 190, 289–301, doi:10.1016/j.rse.2016.12.030.
8. Hedley, J.D.; Roelfsema, C.; Brando, V.; Giardino, C.; Kutser, T.; Phinn, S.; Mumby, P.J.; Barrilero, O.; Laporte, J.; Koetz, B. Coral Reef Applications of Sentinel-2: Coverage, Characteristics, Bathymetry and Benthic Mapping with Comparison to Landsat 8. *Remote Sens Environ* **2018**, 216, 598–614, doi:10.1016/j.rse.2018.07.014.
9. Pahlevan, N.; Balasubramanian, S. V.; Sarkar, S.; Franz, B.A. Toward Long-Term Aquatic Science Products from Heritage Landsat Missions. *Remote Sens (Basel)* **2018**, 10, 1337, doi:10.3390/rs10091337.
10. Cazzaniga, I.; Bresciani, M.; Colombo, R.; Della Bella, V.; Padula, R.; Giardino, C. A Comparison of Sentinel-3-OLCI and Sentinel-2-MSI-Derived Chlorophyll- *a* Maps for Two Large Italian Lakes. *Remote Sensing Letters* **2019**, 10, 978–987, doi:10.1080/2150704X.2019.1634298.
11. Bresciani, M.; Pinardi, M.; Free, G.; Luciani, G.; Ghebrehiwot, S.; Laanen, M.; Peters, S.; Della Bella, V.; Padula, R.; Giardino, C. The Use of Multisource Optical Sensors to Study Phytoplankton Spatio-Temporal Variation in a Shallow Turbid Lake. *Water (Basel)* **2020**, 12, 284, doi:10.3390/w12010284.

12. Bresciani, M.; Rossini, M.; Morabito, G.; Matta, E.; Pinardi, M.; Cogliati, S.; Julitta, T.; Colombo, R.; Braga, F.; Giardino, C. Analysis of Within- and between-Day Chlorophyll-a Dynamics in Mantua Superior Lake, with a Continuous Spectroradiometric Measurement. *Mar Freshw Res* **2013**, *64*, 303, doi:10.1071/MF12229.
13. Hestir, E.L.; Brando, V.E.; Bresciani, M.; Giardino, C.; Matta, E.; Villa, P.; Dekker, A.G. Measuring Freshwater Aquatic Ecosystems: The Need for a Hyperspectral Global Mapping Satellite Mission. *Remote Sens Environ* **2015**, *167*, 181–195, doi:10.1016/j.rse.2015.05.023.
14. Dekker, A.G.; Vos, R.J.; Peters, S.W.M. Comparison of Remote Sensing Data, Model Results and in Situ Data for Total Suspended Matter (TSM) in the Southern Frisian Lakes. *Science of The Total Environment* **2001**, *268*, 197–214, doi:10.1016/S0048-9697(00)00679-3.
15. Dierssen, H.M.; Ackleson, S.G.; Joyce, K.E.; Hestir, E.L.; Castagna, A.; Lavender, S.; McManus, M.A. Living up to the Hype of Hyperspectral Aquatic Remote Sensing: Science, Resources and Outlook. *Front Environ Sci* **2021**, *9*, doi:10.3389/fenvs.2021.649528.
16. Striebel, M.; Behl, S.; Diehl, S.; Stibor, H. Spectral Niche Complementarity and Carbon Dynamics in Pelagic Ecosystems. *Am Nat* **2009**, *174*, 141–147, doi:10.1086/599294.
17. Doxani, G.; Vermote, E.; Roger, J.-C.; Gascon, F.; Adriaensen, S.; Frantz, D.; Hagolle, O.; Hollstein, A.; Kirches, G.; Li, F.; et al. Atmospheric Correction Inter-Comparison Exercise. *Remote Sens (Basel)* **2018**, *10*, 352, doi:10.3390/rs10020352.
18. Pahlevan, N.; Mangin, A.; Balasubramanian, S. V.; Smith, B.; Alikas, K.; Arai, K.; Barbosa, C.; Bélanger, S.; Binding, C.; Bresciani, M.; et al. ACIX-Aqua: A Global Assessment of Atmospheric Correction Methods for Landsat-8 and Sentinel-2 over Lakes, Rivers, and Coastal Waters. *Remote Sens Environ* **2021**, *258*, 112366, doi:10.1016/j.rse.2021.112366.
19. Dierssen, H.M.; Vandermeulen, R.A.; Barnes, B.B.; Castagna, A.; Knaeps, E.; Vanhellemont, Q. QWIP: A Quantitative Metric for Quality Control of Aquatic Reflectance Spectral Shape Using the Apparent Visible Wavelength. *Frontiers in Remote Sensing* **2022**, *3*, doi:10.3389/frsen.2022.869611.
20. Storch, T.; Honold, H.-P.; Chabrillat, S.; Habermeyer, M.; Tucker, P.; Brell, M.; Ohndorf, A.; Wirth, K.; Betz, M.; Kuchler, M.; et al. The EnMAP Imaging Spectroscopy Mission towards Operations. *Remote Sens Environ* **2023**, *294*, 113632, doi:10.1016/j.rse.2023.113632.
21. Chabrillat, S.; Foerster, S.; Segl, K.; Beamish, A.; Brell, M.; Asadzadeh, S.; Milewski, R.; Ward, K.J.; Brosinsky, A.; Koch, K.; et al. The EnMAP Spaceborne Imaging Spectroscopy Mission: Initial Scientific Results Two Years after Launch. *Remote Sens Environ* **2024**, *315*, 114379, doi:10.1016/j.rse.2024.114379.
22. Soppa, M.A.; Brell, M.; Chabrillat, S.; Alvarado, L.M.A.; Gege, P.; Plattner, S.; Somlai-Schweiger, I.; Schroeder, T.; Steinmetz, F.; Scheffler, D.; et al. Full Mission Evaluation of EnMAP Water Leaving Reflectance Products Using Three Atmospheric Correction Processors. *Opt Express* **2024**, *32*, 28215, doi:10.1364/OE.523813.
23. Zibordi, G.; Mélin, F.; Berthon, J.-F.; Holben, B.; Slutsker, I.; Giles, D.; D'Alimonte, D.; Vandemark, D.; Feng, H.; Schuster, G.; et al. AERONET-OC: A Network for the Validation of Ocean Color Primary Products. *J Atmos Ocean Technol* **2009**, *26*, 1634–1651, doi:10.1175/2009JTECHO654.1.

24. Braga, F.; Fabbretto, A.; Vanhellemont, Q.; Bresciani, M.; Giardino, C.; Scarpa, G.M.; Manfè, G.; Concha, J.A.; Brando, V.E. Assessment of PRISMA Water Reflectance Using Autonomous Hyperspectral Radiometry. *ISPRS Journal of Photogrammetry and Remote Sensing* **2022**, *192*, 99–114, doi:10.1016/j.isprsjprs.2022.08.009.
25. Wüest, A.; Bouffard, D.; Guillard, J.; Ibelings, B.W.; Lavanchy, S.; Perga, M.; Pasche, N. LÉXPLORE: A Floating Laboratory on Lake Geneva Offering Unique Lake Research Opportunities. *WIREs Water* **2021**, *8*, doi:10.1002/wat2.1544.
26. González Vilas, L.; Brando, V.E.; Concha, J.A.; Goyens, C.; Dogliotti, A.I.; Doxaran, D.; Dille, A.; Van der Zande, D. Validation of Satellite Water Products Based on HYPERNETS in Situ Data Using a Match-up Database (MDB) File Structure. *Frontiers in Remote Sensing* **2024**, *5*, doi:10.3389/frsen.2024.1330317.
27. Casey, K.A.; Rousseaux, C.S.; Gregg, W.W.; Boss, E.; Chase, A.P.; Craig, S.E.; Mouw, C.B.; Reynolds, R.A.; Stramski, D.; Ackleson, S.G.; et al. A Global Compilation of in Situ Aquatic High Spectral Resolution Inherent and Apparent Optical Property Data for Remote Sensing Applications. *Earth Syst Sci Data* **2020**, *12*, 1123–1139, doi:10.5194/essd-12-1123-2020.
28. IMOS AODN Lucinda Jetty Coastal Observatory: HyperOCR Data Available online: <https://thredds.aodn.org.au/thredds/catalog/IMOS/SRS/OC/LJCO/catalog.html> (accessed on 7 March 2025).
29. Klotz, P. Assessment of the Suitability of PlanetScope SuperDove Imagery for Aquatic Remote Sensing at Lake Junin in Central Peru, Ludwig-Maximilians-Universität München, 2024.
30. Zibordi, G.; Holben, B.N.; Talone, M.; D’Alimonte, D.; Slutsker, I.; Giles, D.M.; Sorokin, M.G. Advances in the Ocean Color Component of the Aerosol Robotic Network (AERONET-OC). *J Atmos Ocean Technol* **2021**, *38*, 725–746, doi:10.1175/JTECH-D-20-0085.1.
31. Ruddick, K.G.; Brando, V.E.; Corizzi, A.; Dogliotti, A.I.; Doxaran, D.; Goyens, C.; Kuusk, J.; Vanhellemont, Q.; Vansteenwegen, D.; Bialek, A.; et al. WATERHYPERNET: A Prototype Network of Automated in Situ Measurements of Hyperspectral Water Reflectance for Satellite Validation and Water Quality Monitoring. *Frontiers in Remote Sensing* **2024**, *5*, doi:10.3389/frsen.2024.1347520.
32. Vansteenwegen, D.; Ruddick, K.; Cattrijse, A.; Vanhellemont, Q.; Beck, M. The Pan-and-Tilt Hyperspectral Radiometer System (PANTHYR) for Autonomous Satellite Validation Measurements—Prototype Design and Testing. *Remote Sens (Basel)* **2019**, *11*, 1360, doi:10.3390/rs11111360.
33. Hommersom, A.; Kratzer, S.; Laanen, M.; Ansko, I.; Ligi, M.; Bresciani, M.; Giardino, C.; Beltrán-Abaunza, J.M.; Moore, G.; Wernand, M.; et al. Intercomparison in the Field between the New WISP-3 and Other Radiometers (TriOS Ramses, ASD FieldSpec, and TACCS). *J Appl Remote Sens* **2012**, *6*, 063615, doi:10.1117/1.JRS.6.063615.
34. Schläpfer, D.; Borel, C.C.; Keller, J.; Itten, K.I. Atmospheric Precorrected Differential Absorption Technique to Retrieve Columnar Water Vapor. *Remote Sens Environ* **1998**, *65*, 353–366, doi:10.1016/S0034-4257(98)00044-3.
35. Gege, P.; Grötsch, P. A Spectral Model for Correcting Sunlint and Skyglint. In Proceedings of the Ocean Optics XXIII 2016; 2016.

36. Gordon, H.R. Ocean Color Remote Sensing Systems: Radiometric Requirements.; Slater, P.N., Ed.; October 12 1988; p. 151.
37. Haan, J.F.; Kokke, J.M.M. Remote Sensing Algorithm Development: Toolkit I: Operationalization of Atmospheric Correction Methods for Tidal and Inland Waters. *Netherlands Remote Sensing Board (BCRS)* **1996**.
38. Sterckx, S.; Knaeps, S.; Kratzer, S.; Ruddick, K. SIMilarity Environment Correction (SIMEC) Applied to MERIS Data over Inland and Coastal Waters. *Remote Sens Environ* **2015**, *157*, 96–110, doi:10.1016/j.rse.2014.06.017.
39. Kiselev, V.; Bulgarelli, B.; Heege, T. Sensor Independent Adjacency Correction Algorithm for Coastal and Inland Water Systems. *Remote Sens Environ* **2015**, *157*, 85–95, doi:10.1016/j.rse.2014.07.025.
40. Richter, R.; Schläpfer, D.; Müller, A. An Automatic Atmospheric Correction Algorithm for Visible/NIR Imagery. *Int J Remote Sens* **2006**, *27*, 2077–2085, doi:10.1080/01431160500486690.
41. Wu, Y.; Knudby, A.; Pahlevan, N.; Lapen, D.; Zeng, C. Sensor-Generic Adjacency-Effect Correction for Remote Sensing of Coastal and Inland Waters. *Remote Sens Environ* **2024**, *315*, 114433, doi:10.1016/j.rse.2024.114433.
42. Kotchenova, S.Y.; Vermote, E.F.; Matarrese, R.; Klemm, Jr., F.J. Validation of a Vector Version of the 6S Radiative Transfer Code for Atmospheric Correction of Satellite Data Part I: Path Radiance. *Appl Opt* **2006**, *45*, 6762, doi:10.1364/AO.45.006762.
43. Lenoble, J.; Herman, M.; Deuzé, J.L.; Lafrance, B.; Santer, R.; Tanré, D. A Successive Order of Scattering Code for Solving the Vector Equation of Transfer in the Earth's Atmosphere with Aerosols. *J Quant Spectrosc Radiat Transf* **2007**, *107*, 479–507, doi:10.1016/j.jqsrt.2007.03.010.
44. Berk, A.; Anderson, G.P.; Acharya, P.K.; Bernstein, L.S.; Muratov, L.; Lee, J.; ...; Shettle, E.P. MODTRAN5: 2006 Update. In *Algorithms and Technologies for Multispectral, Hyperspectral, and Ultraspectral Imagery XII*; 2006; Vol. 6233, pp. 508–515.
45. De Keukelaere, L.; Sterckx, S.; Adriaensen, S.; Knaeps, E.; Reusen, I.; Giardino, C.; Bresciani, M.; Hunter, P.; Neil, C.; Van der Zande, D.; et al. Atmospheric Correction of Landsat-8/OLI and Sentinel-2/MSI Data Using ICOR Algorithm: Validation for Coastal and Inland Waters. *Eur J Remote Sens* **2018**, *51*, 525–542, doi:10.1080/22797254.2018.1457937.
46. Park, Y.-J.; Ruddick, K. Model of Remote-Sensing Reflectance Including Bidirectional Effects for Case 1 and Case 2 Waters. *Appl Opt* **2005**, *44*, 1236, doi:10.1364/AO.44.001236.
47. Gege, P. WASI-2D: A Software Tool for Regionally Optimized Analysis of Imaging Spectrometer Data from Deep and Shallow Waters. *Comput Geosci* **2014**, *62*, 208–215, doi:10.1016/j.cageo.2013.07.022.
48. Vanhellemont, Q. Adaptation of the Dark Spectrum Fitting Atmospheric Correction for Aquatic Applications of the Landsat and Sentinel-2 Archives. *Remote Sens Environ* **2019**, *225*, 175–192, doi:10.1016/j.rse.2019.03.010.

49. Vanhellemont, Q.; Ruddick, K. Atmospheric Correction of Metre-Scale Optical Satellite Data for Inland and Coastal Water Applications. *Remote Sens Environ* **2018**, *216*, 586–597, doi:10.1016/j.rse.2018.07.015.
50. Harmel, T.; Chami, M.; Tormos, T.; Reynaud, N.; Danis, P.-A. Sun glint Correction of the Multi-Spectral Instrument (MSI)-SENTINEL-2 Imagery over Inland and Sea Waters from SWIR Bands. *Remote Sens Environ* **2018**, *204*, 308–321, doi:10.1016/j.rse.2017.10.022.
51. Steinmetz, F.; Deschamps, P.-Y.; Ramon, D. Atmospheric Correction in Presence of Sun Glint: Application to MERIS. *Opt Express* **2011**, *19*, 9783, doi:10.1364/OE.19.009783.
52. Steinmetz, F.; Ramon, D. Sentinel-2 MSI and Sentinel-3 OLCI Consistent Ocean Colour Products Using POLYMER. In Proceedings of the Remote Sensing of the Open and Coastal Ocean and Inland Waters; Frouin, R.J., Murakami, H., Eds.; SPIE, October 30 2018; p. 13.
53. de los Reyes, R.; Langheinrich, M.; Schwind, P.; Richter, R.; Pflug, B.; Bachmann, M.; Müller, R.; Carmona, E.; Zekoll, V.; Reinartz, P. PACO: Python-Based Atmospheric Correction. *Sensors* **2020**, *20*, 1428, doi:10.3390/s20051428.
54. IOCCG (2025) Available online: <https://ioccg.org/resources/software/> (accessed on 20 October 2025).
55. Vanhellemont, Q.; Ruddick, K. Turbid Wakes Associated with Offshore Wind Turbines Observed with Landsat 8. *Remote Sens Environ* **2014**, *145*, 105–115, doi:10.1016/j.rse.2014.01.009.
56. Vanhellemont, Q.; Ruddick, K. Acolite for Sentinel-2: Aquatic Applications of MSI Imagery. In Proceedings of the 2016 ESA Living Planet Symposium; Prague, Czech Republic, 2016.
57. Vanhellemont, Q. Sensitivity Analysis of the Dark Spectrum Fitting Atmospheric Correction for Metre- and Decametre-Scale Satellite Imagery Using Autonomous Hyperspectral Radiometry. *Opt Express* **2020**, *28*, 29948, doi:10.1364/OE.397456.
58. Vanhellemont, Q.; Ruddick, K. Atmospheric Correction of Sentinel-3/OLCI Data for Mapping of Suspended Particulate Matter and Chlorophyll-a Concentration in Belgian Turbid Coastal Waters. *Remote Sens Environ* **2021**, *256*, 112284, doi:10.1016/j.rse.2021.112284.
59. Chami, M.; Lafrance, B.; Fougner, B.; Chowdhary, J.; Harmel, T.; Waquet, F. OSOAA: A Vector Radiative Transfer Model of Coupled Atmosphere-Ocean System for a Rough Sea Surface Application to the Estimates of the Directional Variations of the Water Leaving Reflectance to Better Process Multi-Angular Satellite Sensors Data over the Ocean. *Opt Express* **2015**, *23*, 27829, doi:10.1364/OE.23.027829.
60. Hess, M.; Koepke, P.; Schult, I. Optical Properties of Aerosols and Clouds: The Software Package OPAC. *Bull Am Meteorol Soc* **1998**, *79*, 831–844, doi:10.1175/1520-0477(1998)079<0831:OPOAAC>2.0.CO;2.
61. Yang, P.; Feng, Q.; Hong, G.; Kattawar, G.W.; Wiscombe, W.J.; Mishchenko, M.I.; Dubovik, O.; Laszlo, I.; Sokolik, I.N. Modeling of the Scattering and Radiative Properties of Nonspherical Dust-like Aerosols. *J Aerosol Sci* **2007**, *38*, 995–1014, doi:10.1016/j.jaerosci.2007.07.001.
62. Gasteiger, J.; Wiegner, M. MOPSMAP v1.0: A Versatile Tool for the Modeling of Aerosol Optical Properties. *Geosci Model Dev* **2018**, *11*, 2739–2762, doi:10.5194/gmd-11-2739-2018.

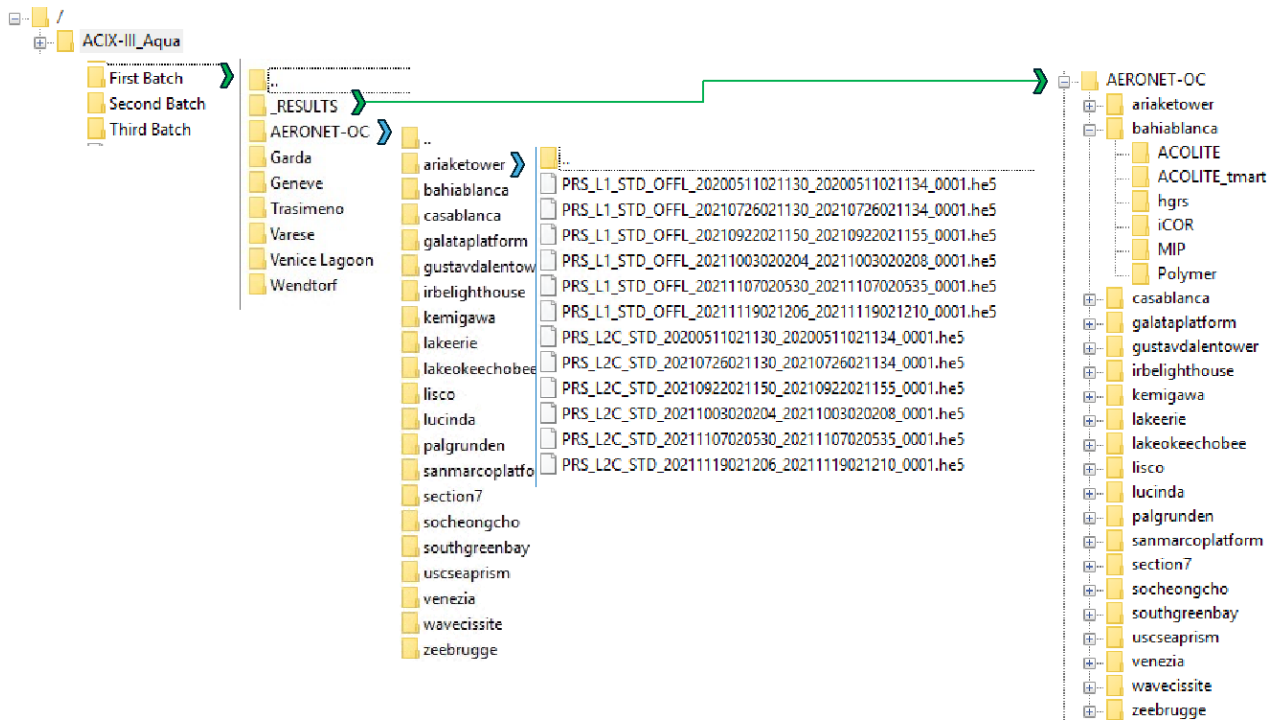
63. Richter, R. A Spatially Adaptive Fast Atmospheric Correction Algorithm. *Int J Remote Sens* **1996**, *17*, 1201–1214, doi:10.1080/01431169608949077.
64. Gege, P. The Water Color Simulator WASI: An Integrating Software Tool for Analysis and Simulation of Optical in Situ Spectra. *Comput Geosci* **2004**, *30*, 523–532, doi:10.1016/j.cageo.2004.03.005.
65. Albert, A.; Mobley, C. An Analytical Model for Subsurface Irradiance and Remote Sensing Reflectance in Deep and Shallow Case-2 Waters. *Opt Express* **2003**, *11*, 2873, doi:10.1364/OE.11.002873.
66. Mobley, C.D.; Gentili, B.; Gordon, H.R.; Jin, Z.; Kattawar, G.W.; Morel, A.; Reinersman, P.; Stamnes, K.; Stavn, R.H. Comparison of Numerical Models for Computing Underwater Light Fields. *Appl. Opt.* **1993**, *32*.
67. Gege Analytic Model for the Direct and Diffuse Components of Downwelling Spectral Irradiance in Water. *Appl Opt* **2012**, *51*, 1407, doi:10.1364/AO.51.001407.
68. Gregg, W.W.; Carder, K.L. A Simple Spectral Solar Irradiance Model for Cloudless Maritime Atmospheres. *Limnol Oceanogr* **1990**, *35*, 1657–1675, doi:10.4319/lo.1990.35.8.1657.
69. Defoin-Platel, M.; Chami, M. How Ambiguous Is the Inverse Problem of Ocean Color in Coastal Waters? *J Geophys Res Oceans* **2007**, *112*, doi:10.1029/2006JC003847.
70. Wu, Y.; Knudby, A.; Lapen, D. Topography-Adjusted Monte Carlo Simulation of the Adjacency Effect in Remote Sensing of Coastal and Inland Waters. *J Quant Spectrosc Radiat Transf* **2023**, *303*, 108589, doi:10.1016/j.jqsrt.2023.108589.
71. Global Modeling and Assimilation Office MERRA-2 Tavg1_2d_chm_Nx: 2d,1-Hourly,Time-Averaged,Single-Level,Assimilation,Carbon Monoxide and Ozone Diagnostics V5.12.4. *Greenbelt, MD, USA, Goddard Earth Sciences Data and Information Services Center (GES DISC) [Dataset]* **2015**.
72. Vermote, E.F.; Tanre, D.; Deuze, J.L.; Herman, M.; Morcette, J.-J. Second Simulation of the Satellite Signal in the Solar Spectrum, 6S: An Overview. *IEEE Transactions on Geoscience and Remote Sensing* **1997**, *35*, 675–686, doi:10.1109/36.581987.
73. Giardino, C.; Bresciani, M.; Braga, F.; Fabbretto, A.; Ghirardi, N.; Pepe, M.; Gianinetto, M.; Colombo, R.; Cogliati, S.; Ghebrehiwot, S.; et al. First Evaluation of PRISMA Level 1 Data for Water Applications. *Sensors* **2020**, *20*, 4553, doi:10.3390/s20164553.
74. Niroumand-Jadidi, M.; Bovolo, F.; Bruzzone, L. Water Quality Retrieval from PRISMA Hyperspectral Images: First Experience in a Turbid Lake and Comparison with Sentinel-2. *Remote Sens (Basel)* **2020**, *12*, 3984, doi:10.3390/rs12233984.
75. Bresciani, M.; Giardino, C.; Fabbretto, A.; Pellegrino, A.; Mangano, S.; Free, G.; Pinardi, M. Application of New Hyperspectral Sensors in the Remote Sensing of Aquatic Ecosystem Health: Exploiting PRISMA and DESIS for Four Italian Lakes. *Resources* **2022**, *11*, 8, doi:10.3390/resources11020008.
76. Pellegrino, A.; Fabbretto, A.; Bresciani, M.; de Lima, T.M.A.; Braga, F.; Pahlevan, N.; Brando, V.E.; Kratzer, S.; Gianinetto, M.; Giardino, C. Assessing the Accuracy of PRISMA Standard

- Reflectance Products in Globally Distributed Aquatic Sites. *Remote Sens (Basel)* **2023**, *15*, 2163, doi:10.3390/rs15082163.
77. Fabbretto, A.; Bresciani, M.; Pellegrino, A.; Alikas, K.; Pinardi, M.; Mangano, S.; Padula, R.; Giardino, C. Tracking Water Quality and Macrophyte Changes in Lake Trasimeno (Italy) from Spaceborne Hyperspectral Imagery. *Remote Sens (Basel)* **2024**, *16*, 1704, doi:10.3390/rs16101704.
 78. Bailey, S.W.; Werdell, P.J. A Multi-Sensor Approach for the on-Orbit Validation of Ocean Color Satellite Data Products. *Remote Sens Environ* **2006**, *102*, 12–23, doi:10.1016/j.rse.2006.01.015.
 79. Giardino, C.; Pahlevan, N.; Fabbretto, A.; Panizza, L.; Pellegrino, A.; Vandermeulen, R.; Gianinetto, M.; Adriaensen, S.; Agten, J.; Bernert, H.; et al. ACIX-III Aqua: Evaluation of Atmospheric Correction for Hyperspectral PRISMA Imagery over Inland and Coastal Waters. *Int J Remote Sens* **2025**, 1–25, doi:10.1080/01431161.2025.2574517.
 80. Bi, S.; Hieronymi, M. Holistic Optical Water Type Classification for Ocean, Coastal, and Inland Waters. *Limnol Oceanogr* **2024**, *69*, 1547–1561, doi:10.1002/lno.12606.
 81. Vandermeulen, R.A.; Mannino, A.; Craig, S.E.; Werdell, P.J. 150 Shades of Green: Using the Full Spectrum of Remote Sensing Reflectance to Elucidate Color Shifts in the Ocean. *Remote Sens Environ* **2020**, *247*, 111900, doi:10.1016/j.rse.2020.111900.
 82. Balasubramanian, S. V.; Pahlevan, N.; Smith, B.; Binding, C.; Schalles, J.; Loisel, H.; Gurlin, D.; Greb, S.; Alikas, K.; Randla, M.; et al. Robust Algorithm for Estimating Total Suspended Solids (TSS) in Inland and Nearshore Coastal Waters. *Remote Sens Environ* **2020**, *246*, 111768, doi:10.1016/j.rse.2020.111768.
 83. Bracher, A.; Randrianalisoa, A.N.; Soppa, M.A.; Chabrillat, S.; Scheffler, D.; Steinmetz, F.; Vanhellemont, Q.; Gege, P.; ...; Vansteenwegen, D. Evaluation of ENMAP Water Leaving Reflectance Products from Three Atmospheric Correction Methods by Validation with Hyperspectral and Multispectral in Situ Measurements from Inland and Coastal Water around the World. In Proceedings of the ESA Living Plant Symposium; Vienna, Austria, 2025.
 84. Goyens, C.; Lavigne, H.; Dille, A.; Vervaeren, H. Using Hyperspectral Remote Sensing to Monitor Water Quality in Drinking Water Reservoirs. *Remote Sens (Basel)* **2022**, *14*, 5607, doi:10.3390/rs14215607.
 85. Peters S.; Laanen M.; Groetsch P.; Ghezehegn S.; Poser K.; Hommersom A.; De Reus E.; Spaias L. WISPstation: A New Autonomous above Water Radiometer System. In Proceedings of the Ocean Optics XXIV Conference; Dubrovnik, Croatia, 2018; pp. 7–12.
 86. Brando, V.; Keen, R.; Daniel, P.; Baumeister, A.; Nethery, M.; Baumeister, H.; Hawdon, A.; Swan, G.; Mitchell, R.; Campbell, S.; et al. The Lucinda Jetty Coastal Observatory's Role in Satellite Ocean Colour Calibration and Validation for Great Barrier Reef Coastal Waters. In Proceedings of the OCEANS'10 IEEE SYDNEY; IEEE, May 2010; pp. 1–8.
 87. Tilstone, G.; Dall'Olmo, G.; Hieronymi, M.; Ruddick, K.; Beck, M.; Ligi, M.; Costa, M.; D'Alimonte, D.; Vellucci, V.; Vansteenwegen, D.; et al. Field Intercomparison of Radiometer Measurements for Ocean Colour Validation. *Remote Sens (Basel)* **2020**, *12*, 1587, doi:10.3390/rs12101587.

88. Zibordi, G.; Voss, K.J.; Johnson, B.C.; Mueller, J.L. Ocean Optics and Biogeochemistry Protocols for Satellite Ocean Colour Sensor Validation, Volume 3.0: Protocols for Satellite Ocean Colour Data Validation: In Situ Optical Radiometry. *International Ocean Colour Coordinating Group (IOCCG) Dartmouth, NS, Canada* **2019**.
89. Lee, Z.P.; Du, K.; Voss, K.J.; Zibordi, G.; Lubac, B.; Arnone, R.; Weidemann, A. An Inherent-Optical-Property-Centered Approach to Correct the Angular Effects in Water-Leaving Radiance. *Appl Opt* **2011**, *50*, 3155, doi:10.1364/AO.50.003155.
90. Thuillier, G.; Hersé, M.; Labs, D.; Foujols, T.; Peetermans, W.; Gillotay, D.; Simon, P.C.; Mandel, H. The Solar Spectral Irradiance from 200 to 2400 Nm as Measured by the SOLSPEC Spectrometer from the Atlas and Eureka Missions. *Sol Phys* **2003**, *214*, 1–22, doi:10.1023/A:1024048429145.
91. Scheffler, D.; Brell, M.; Bohn, N.; Alvarado, L.; Soppa, M.A.; Segl, K.; Bracher, A.; Chabrillat, S. EnPT – an Alternative Pre-Processing Chain for Hyperspectral EnMAP Data. In Proceedings of the IGARSS 2023 - 2023 IEEE International Geoscience and Remote Sensing Symposium; IEEE, July 16 2023; pp. 7416–7418.
92. Jakimow, B.; Janz, A.; Thiel, F.; Okujeni, A.; Hostert, P.; van der Linden, S. EnMAP-Box: Imaging Spectroscopy in QGIS. *SoftwareX* **2023**, *23*, 101507, doi:10.1016/j.softx.2023.101507.
93. Vanhellemont, Q. Daily Metre-Scale Mapping of Water Turbidity Using CubeSat Imagery. *Opt Express* **2019**, *27*, A1372, doi:10.1364/OE.27.0A1372.
94. EUMETSAT Recommendations for Sentinel-3 OLCI Ocean Colour Product Validations in Comparison with in Situ Measurements – Matchup Protocols. .
95. Lavigne, H.; Ruddick, K. Inter-Band Calibration for Hyperspectral Water Remote Sensing: Demonstration for Chris-Proba. In Proceedings of the 2021 IEEE International Geoscience and Remote Sensing Symposium IGARSS; IEEE, July 11 2021; pp. 7771–7774.
96. Doxaran, D.; ElKilani, B.; Corizzi, A.; Goyens, C. Validation of Satellite-Derived Water-Leaving Reflectance in Contrasted French Coastal Waters Based on HYPERNETS Field Measurements. *Frontiers in Remote Sensing* **2024**, *4*, doi:10.3389/frsen.2023.1290110.

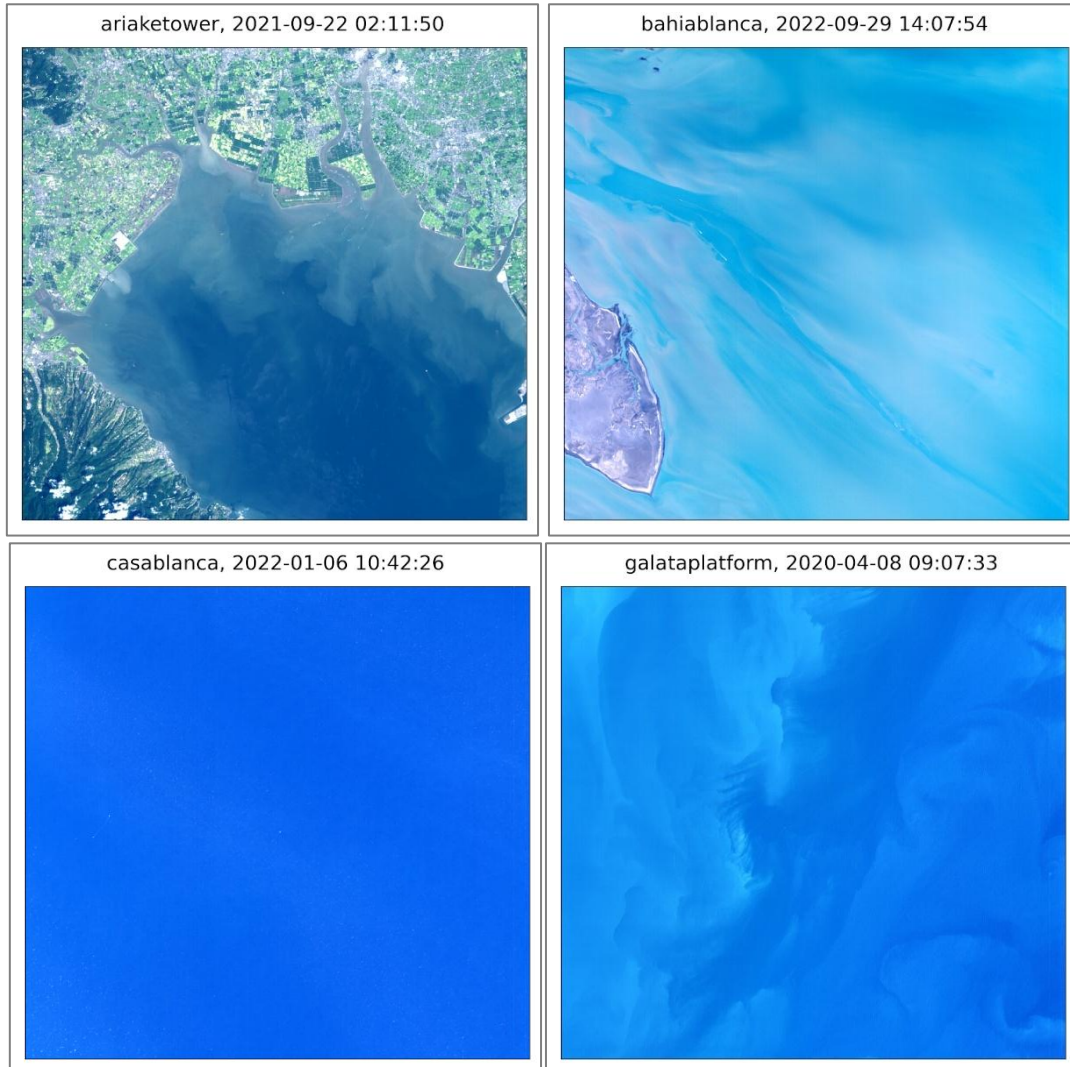
10 PRISMA DATA REPOSITORY

Consistency in image processing and data extraction between all contributors was made possible by the FTP platform of ESA. The platform consisted of three different folders: First Batch (2019-2022 data), Second Batch (2023 data), Third Batch (Rio de la Plata data). In each folder the respective PRISMA L1 and L2C products (in HE5 format) were uploaded for both the AERONET-OC and CVD dataset. Within each of the three folders, the results referring to the atmospheric correction models were also uploaded (in the subfolders ACOLITE, ACOLITE_tmart, hgrs, iCOR, MIP and Polymer, all in NC format). In the results section, there is also a dedicated folder referring to the QWIP analysis, where the results of the analysis obtained from each model are reported. *In situ* reference data are not stored in the ESA FTP, but we could add if it relevant for ESA.



11 PRISMA IMAGE GALLERY

An overview of PRISMA images for each of the site is presented; please note that for each of the sites there are more than images (cf. Figure 1).



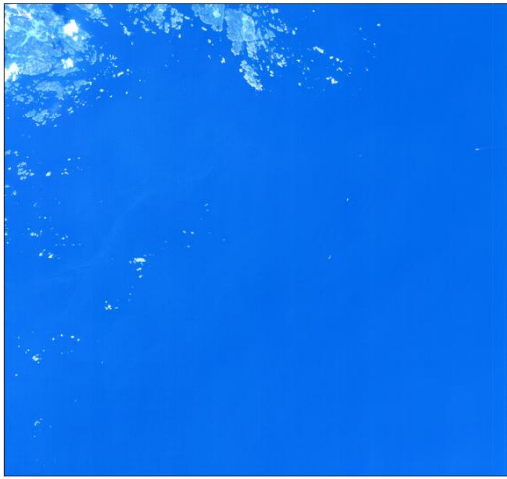
Garda, 2022-03-09 10:14:19



Geneve, 2021-09-06 10:37:12



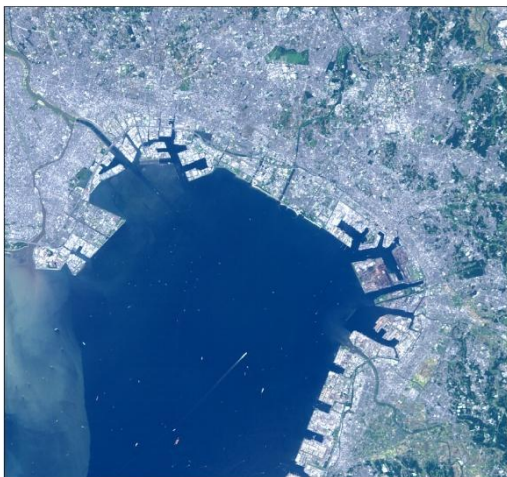
gustavdalentower, 2021-08-30 10:13:43



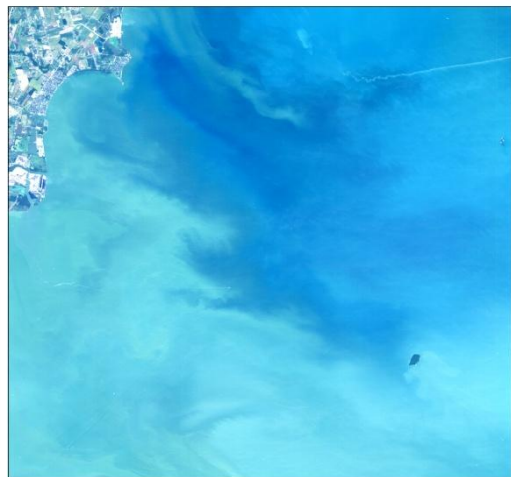
irbelighthouse, 2022-05-23 10:03:38



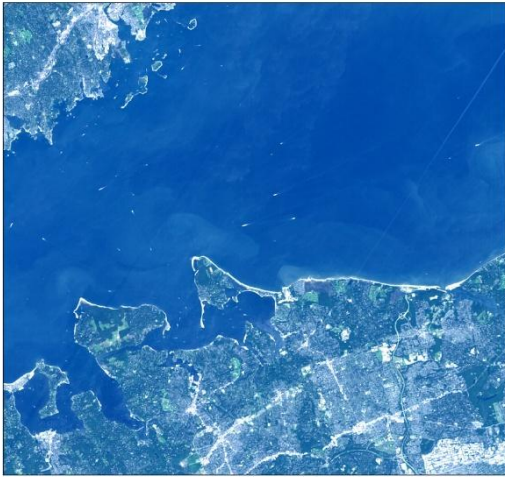
kemigawa, 2022-09-26 01:37:29



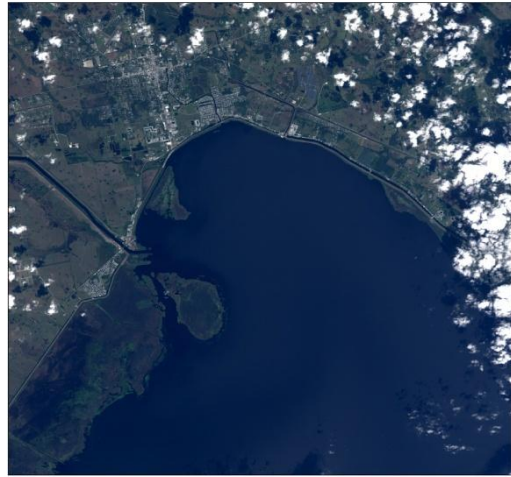
lakeerie, 2021-09-10 16:36:46



lisco, 2021-09-19 15:53:30



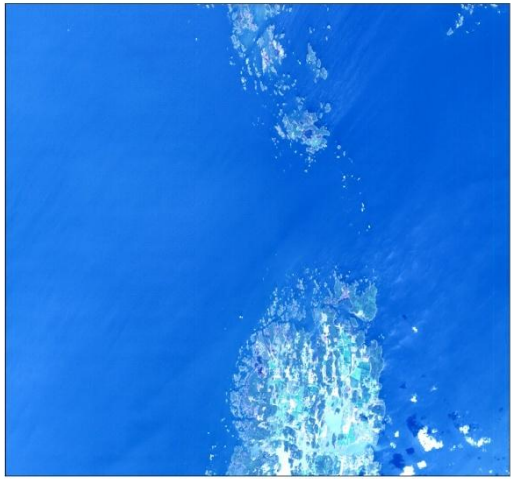
lakeokeechobee, 2021-12-04 16:07:40



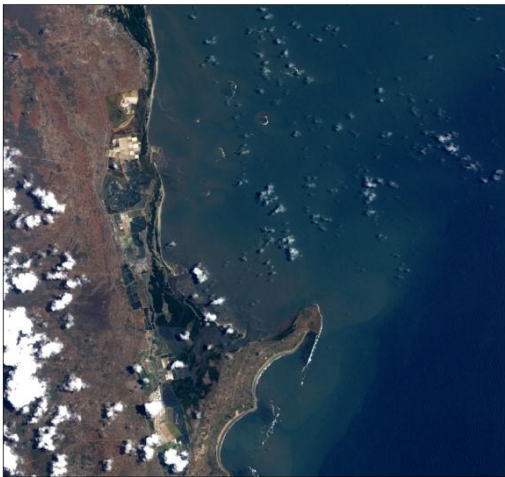
lucinda, 2021-09-21 00:32:01



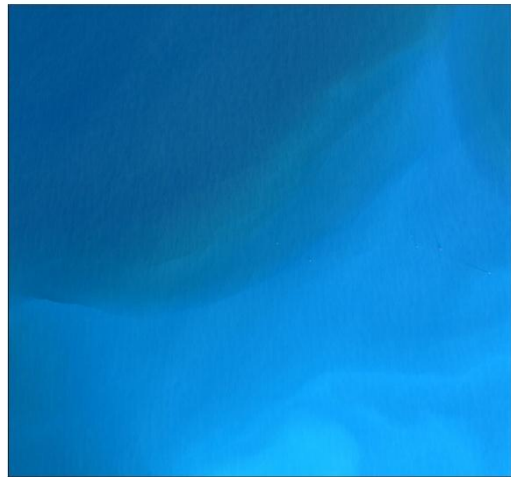
palgrunden, 2021-05-19 10:36:19



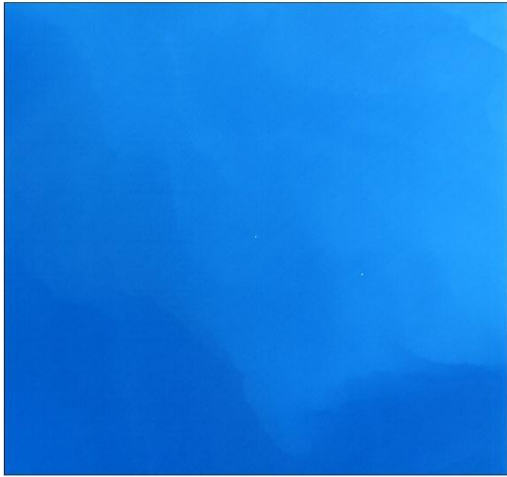
sanmarcoplatform, 2022-09-30 07:46:20



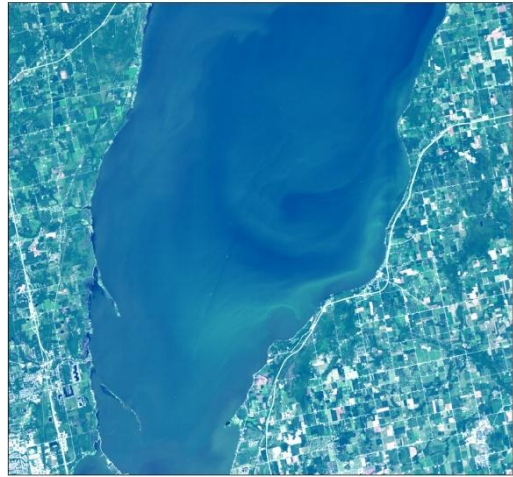
section7, 2022-06-17 09:00:27



socheongcho, 2021-04-14 02:33:38



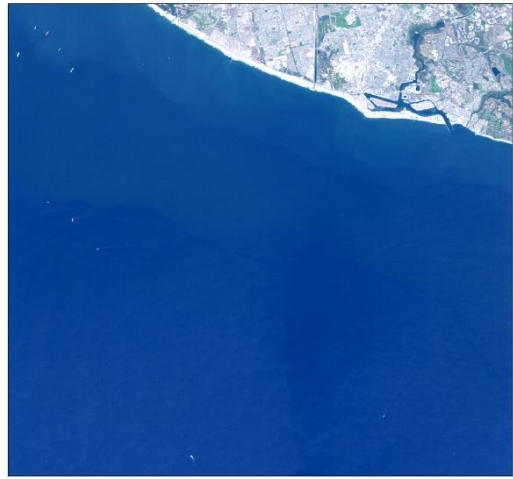
southgreenbay, 2020-08-12 16:45:22



Trasimeno, 2019-07-26 10:13:20



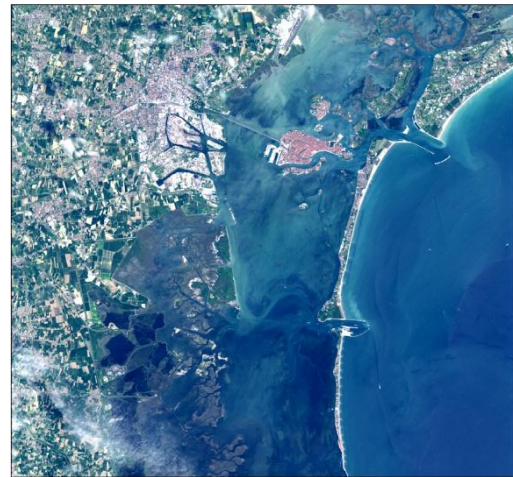
uscseaprism, 2020-03-27 18:46:09



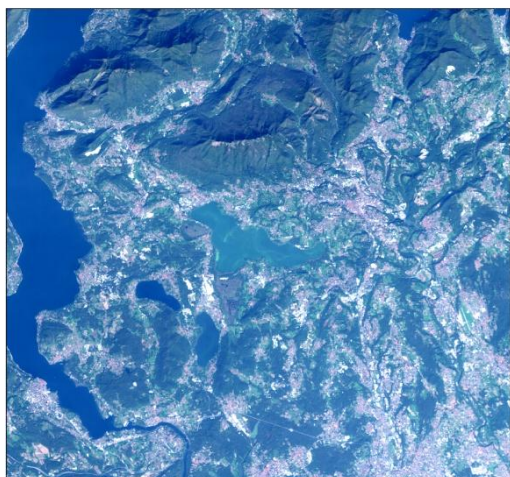
venezia, 2021-03-09 10:17:25



Venice_Lagoon, 2020-07-14 10:16:46



Varese, 2021-10-16 10:27:35



wavecissite, 2021-03-09 16:50:26



zeebrugge, 2022-04-10 11:02:31

